CERN – EUROPEAN ORGANIZATION FOR NUCLEAR RESEARCH

CLIC – Note – 1081

THERMAL CONTROL FOR THE TWO-BEAM MODULE OF THE COMPACT LINEAR COLLIDER WITH COMPUTATIONAL FLUID DYNAMICS SIMULATIONS OF CONJUGATE HEAT TRANSFER PROBLEMS, WITH SUBSIDIARY FINITE-ELEMENT SIMULATIONS

Cheuk Wing Edmond Lam[1], Alex Vamvakas[2],
Markus Aicheler[3], Jukka Ilmari Vainola[3], Steffen Doebert[4]

[1]ETH Zurich, Switzerland
[2]National Technical University of Athens, Greece
[3]Helsinki Institute of Physics, Finland
[4]European Organization for Nuclear Research, Switzerland

CERN-ACC-2018-0031
15/06/2018

Abstract

Conjugate heat transfer simulations were performed for the two-beam module of the Compact Linear Collider (CLIC). A full approach using ANSYS Fluent is presented for the determination of heat dissipation values from the main beam portion of the module to the cooling air and water. A transient model for heat dissipated through the tunnel to the outside soil is presented as well. Structural stress-strain simulations and modal analyses were performed for the adjustable supports with the finite-element method using ANSYS Mechanical. The operating range of the adjustable supports was determined.

Geneva, Switzerland
15 June 2018

ETH
Eidgenössische Technische Hochschule Zürich
Swiss Federal Institute of Technology Zurich

CERN
European Organization for Nuclear Research
Organisation européenne pour la recherche nucléaire

Thermal Control for the Two-beam Module of the Compact Linear Collider with Computational Fluid Dynamics Simulations of Conjugate Heat Transfer Problems, with Subsidiary Finite-element Simulations

Report

Cheuk Wing Edmond Lam, Alex Vamvakas, Markus Aicheler, Jukka Ilmari Vainola, Steffen Doebert

Abstract

Conjugate heat transfer simulations were performed for the two-beam module of the Compact Linear Collider (CLIC). A full approach using ANSYS Fluent is presented for the determination of heat dissipation values from the main beam portion of the module to the cooling air and water. A transient model for heat dissipated through the tunnel to the outside soil is presented as well.

Structural stress-strain simulations and modal analyses were performed for the adjustable supports with the finite-element method using ANSYS Mechanical. The operating range of the adjustable supports was determined.

Acknowledgements

I would like to first and foremost thank Dr. Steffen Doebert for accepting me as a trainee in the CLIC project team at the Beams Department. The six months in his team was rewarding and fruitful.

I would like to as well thank Mr. Alex Vamvakas, Dr. Markus Aicheler, and Mr. Jukka Ilmari Vainola for their excellent supervision in their diverse areas of expertise, and their advice for my future engineering career.

The good times spent with fellow students Ms. Ana Dorda Martin, Mr. Seongyeol Kim and Mr. Hermann Winrich Pommerenke, were memorable and will not be forgotten. I have to extend my thanks to Ms. Anouchka Chenevard Sommaruga, for her great hospitality during my stay in Geneva. I send my best wishes for her gorgeous theatre work at Théâtrochamp, of which she serves as the founding director.

Last but not least, I would like to express my heartfelt gratitude to my partner, Ms. Florance Ko, for her support over the long years, wherever I am.

Without the abovementioned individuals, this work, and my time at CERN would hardly be satisfying. Thank you.

Cheuk Wing Edmond Lam

12. June 2018

Table of Contents

Index of Tables and Figures

Tables

Figures

1. Introduction

1.1. Background of this report

This report summarises and concludes the work performed for the two-beam module of the Compact Linear Collider (CLIC) study between 01.09.2017 and 28.02.2018, when the first author was a trainee at CERN (BE-RF-MK), as a part of his master's studies in mechanical engineering at ETH Zurich. It aims to serve as a convenient reference for future efforts with modelling and simulations of the two-beam module.

1.2. Compact Linear Collider and the two-beam module

The two-beam module is a fundamental part of the Compact Linear Collider (CLIC). A model of it is shown in Figure 1. The collider consists of over 10’000 of such modules repeated in serial, forming the distance with which particles are accelerated [1]. This report skips the discussion on the arrangement of the module. For details, refer to the conceptual design report [1].

It is then without question that, understanding the behaviour of the two-beam module is essential in understanding the behaviour of the collider. In this work, most of the content is dedicated to the investigation of the heat dissipated from the module, specifically, the heat dissipated to the air within the tunnel, to the water in the cooling circuit, and to the soil external to the tunnel. The remaining content is dedicated to the mechanical behaviour of adjustable supports, with which the position of the module can be fine-tuned.

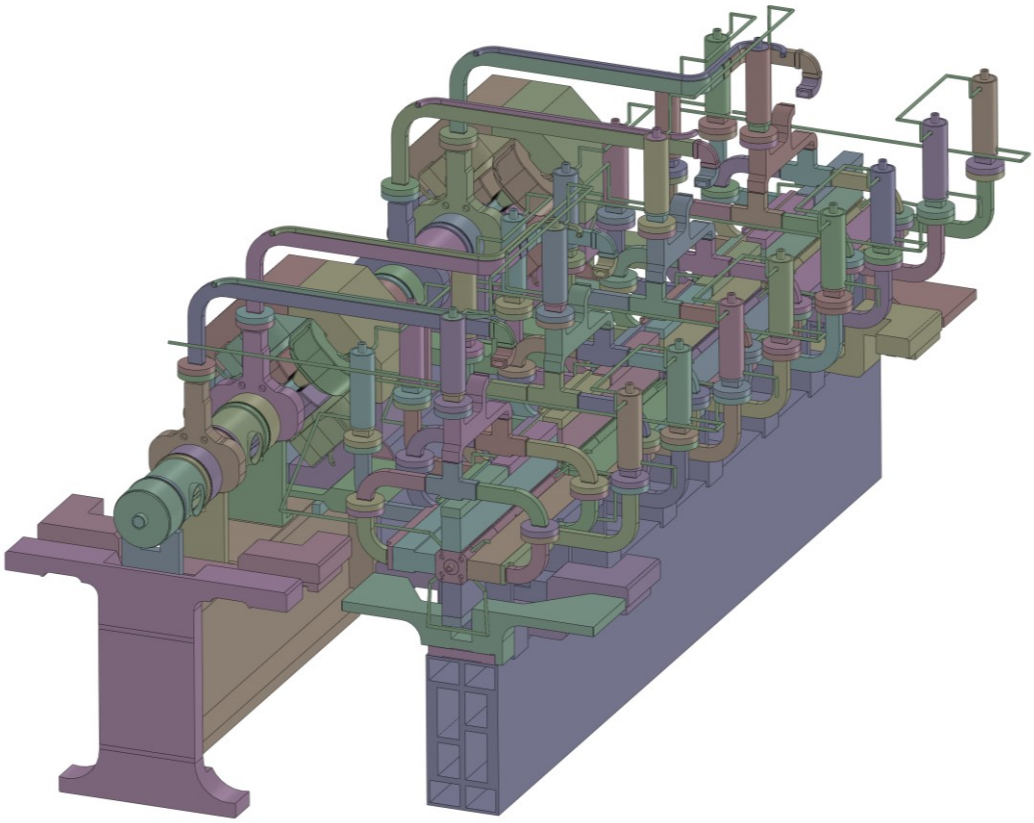

Figure 1: Two-beam module

1.3. Thermal behaviour determination

A proper understanding of the thermal behaviour of the module is desired for several reasons. For the proposed length of tens of kilometres of the collider, the heat dissipation to air is the basic factor governing the choice of the tunnel ventilation system, which can translate to millions of euros in terms of costs. Second, thermal expansion of the materials must be considered given the strict alignment requirements of the collider. The size of the alignment window over 200 m is measuring merely 28 μm [2]. It is desirable to determine an optimal operating temperature at this point so that alignment can be performed accordingly.

The determination of heat dissipation values for the module is a conjugate heat transfer problem, which involves the coupling of heat transfer within the solid regions (e.g. conduction within the module) and heat transfer within the fluid regions (e.g. convection of air). Chapter 2 begins by first describing previous approaches to this problem and their limitations. Chapter 3 then introduces the computational fluid dynamics approach which constitutes much of this work.

1.4. Structural behaviour determination

Given the strict requirements in alignment, it is desirable to correct for minor deviations from nominal design dimensions after the collider is installed in the tunnel. In view of this, the supports of the accelerating structure are to be made adjustable based on elastic strain of a chosen material. Simulations were used to identify the maximum movement window of such supports, and the resonance frequencies of the system. Chapter 4 discusses the finite-element method simulations performed.

2. Existing Approaches to Thermal Behaviour Determination

2.1. Introduction

There are 3 existing approaches to model the heat dissipation from the module to different media before the CFD approach introduced in this report. They involve different extents of simplification and approximation, with different solution times. An overview of these approaches are given in [3].

2.2. Analytical model

The analytical model was developed by M. Aicheler and A. Vamvakas. It had a highly simplified geometry with only the essential components of the model, i.e. power input to the system, heat dissipation to air and to water, and heat dissipation by radiation [4]. Because of the lack of the consideration of the actual geometry, the heat transfer was modelled by coefficients only. Such coefficients involved heavy assumptions. The main advantage was that computation time was only in a matter of seconds.

2.3. Finite-element approach with ANSYS Mechanical

The finite-element approach was developed by A. Moilanen. It used the actual geometry of the module. The chosen finite-element solver, ANSYS Mechanical, solves for the conduction equation within the module. The convective heat transfer to air and to water, and the heat dissipated by radiation were modelled with coefficients. In particular, a single (ideally the average) value of the heat transfer coefficient was chosen for all the surfaces of the module exposed to air flow. Naturally, these coefficients involved assumptions. The computation time was on the scale of minutes.

2.4. Experimental approach

The experimental approach was developed by M. Aicheler, V. Andavan, and A. Vamvakas. Results were obtained from the module placed in a wind tunnel.

There were a few sources of errors in the experimental approach. The wind tunnel cross section did not match with the supposed circular cross section when the collider is put into operation. This error was only minimal if the change in the cross section did not significantly impact the air flow around the module. Uncertainties existed as well for the sensors, generating error bars of tens of watts. Third, there was no actual beam within the module during the experimental measurements. The heat dissipated from the beam was estimated by heating elements located close to the beam location instead.

The experimental approach had as well a few limitations. First of all, it was not possible to directly measure heat dissipated to air. The method adopted was indirect: 1) measure the change in water temperature and the water flow rate to deduce the heat dissipated to water; and then 2) subtract this value from the power generated from the heating elements. The resulting value was the sum of the heat dissipated by convection to air, and by radiation.

Experiments provided results for only specific variables, for example temperature values; and only at pre-selected points, rather than a field that one can obtain with modelling methods. Nevertheless, experiments provided an indispensable way to validate the mathematical model and the finite-element model, as well as the CFD model, if the measurement errors were sufficiently low.

3. The CFD Approach to Thermal Behaviour Determination

3.1. A new approach

The CFD approach aimed to complement the existing ones in Chapter 2. Figure 2 is taken from [3]:

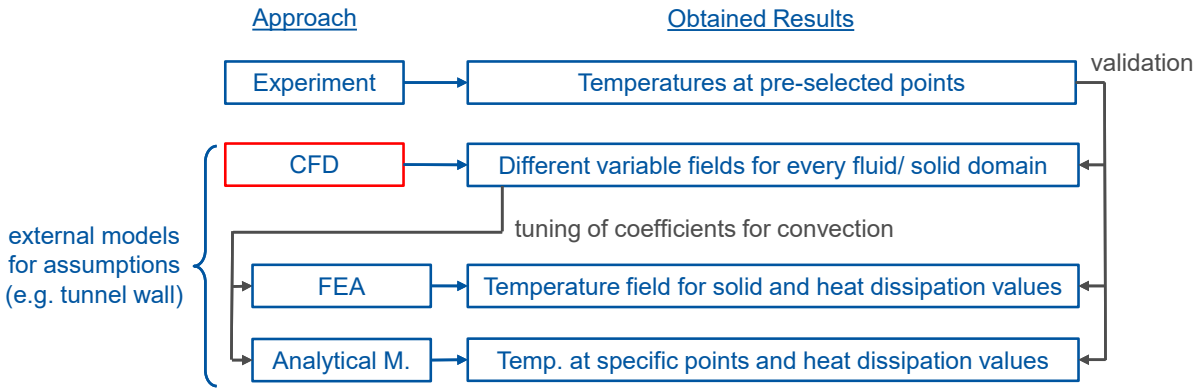

Figure 2: Workflow incorporating CFD [3]

Figure 2 illustrates the role of CFD in the system of approaches. While the finite-element model and the analytical model enjoyed the advantages of short computation times (within minutes), they suffered from the estimation errors of heavy assumptions in heat transfer coefficients. The CFD approach undertaken in this work was an all-coupled approach in which the conduction heat transfer within the module, convective heat transfer to air and to water, and the radiation heat exchange with the tunnel wall were all coupled in the final model. This was performed at the expense of significant human labour, as well as CPU time (measured in hours, on the CERN cluster). Therefore, it was of interest to take the results from CFD simulations to tune the heat transfer coefficients in the existing models. In this way, one can perform a parametric study with different incoming air temperatures and air speeds, for example, in a reasonable amount of time using the tuned coefficients. This concept is illustrated in Figure 2.

Nevertheless, even with an all-coupled approach, there was a finite size of the computational domain. Modelling and estimation were present at domain boundaries, e.g. heat transfer to soil out of the tunnel wall. Turbulence and radiation heat exchange were modelled as well. The choice of turbulence and radiation models involved engineering judgement and may introduce other errors. These should be taken note when interpreting the results.

3.2. Software and general workflow

This section describes the workflow generally followed in this work to perform a CFD analysis.

3.2.1. Geometry repair and simplification

The original 3D CAD file, often in STEP format, was first imported to SolidWorks 2017 for geometry repair and simplification. It should be noted that the “original” geometry refers to the geometry that was left by previous colleagues. Usually, this had already been simplified to some extent by previous users. Some of such geometries had been sufficiently simplified to perform a finite-element analysis with ANSYS Mechanical, where mesh generation and solution methods were believed to be more robust to geometry issues. Some other geometries had been partially simplified in previous attempts to perform a CFD analysis, but these attempts did not proceed to completion due to time limitations.

It was essential to repair, simplify, and verify the geometry before mesh generation. It should be straightforward to imagine that when a structure was placed in a fluid domain, the fluid would enter any tiny gap of the solid geometry. This would in turn create highly skewed elements and a low-quality mesh, if not a non-readable mesh. There would be a large number of small elements in the gaps, and it would take a longer meshing time than necessary. Such mesh would introduce convergence issues later in the solver, and the accuracy would be lower because there would be no thermal contact when there should be. On the other hand, fillets and small features (e.g. screws, bolts, nuts) were removed reasonably as much as possible, since they required a more refined mesh to represent their geometry but did not alter much the fluid flow patterns.

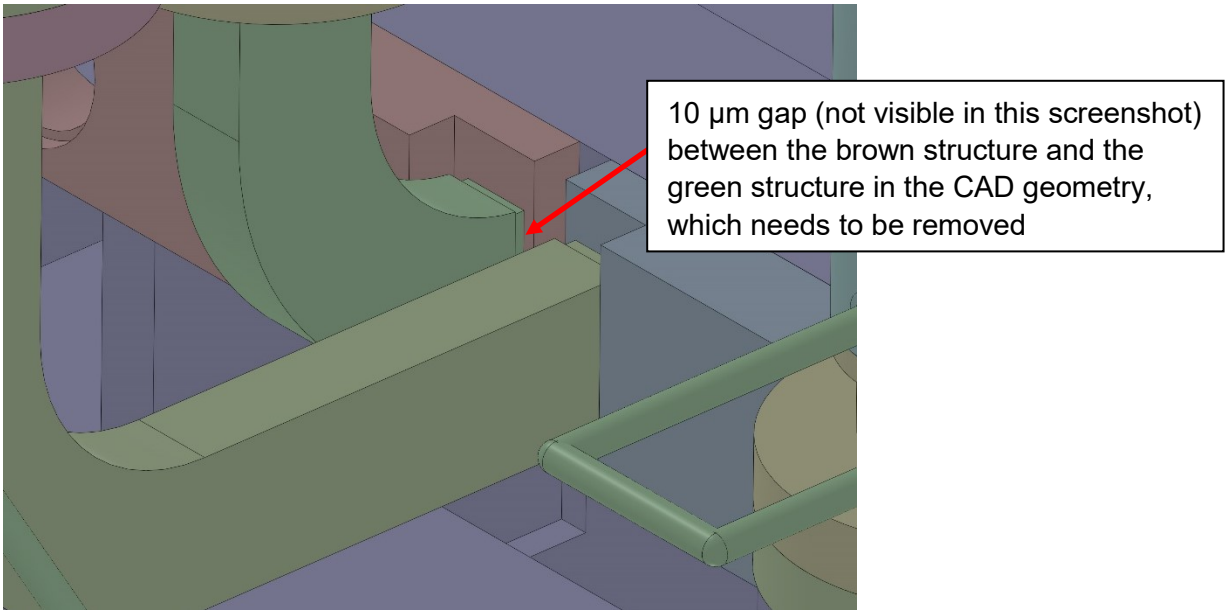

Figure 3: Gap between the waveguide and the accelerating structure

Some of these gaps might have been left there on purpose. A reason for this was to leave for manufacturing tolerances. The gap in Figure 3 may be one of these gaps. All of these gaps, however, had to be removed before meshing.

In complex problems, such as the simplification of the main beam part of the entire module, this process took over a month.

3.2.2. Mesh generation procedures

3.2.2.1. Import to ICEM CFD

Mesh generation, or meshing, is arguably the most challenging step since it is highly problem-dependent, and it can require a lot of user input and judgement. The mesh quality directly impacts the plausibility to attain a converged solution.

With a “clean” geometry, the file could be safely passed to the meshing phase. A STEP file was exported from SolidWorks 2017 and imported to ANSYS Workbench. It was then read into the geometry modeller SpaceClaim, and a fluid domain was generated by using the *Enclosure* feature in the software. The resulting SpaceClaim file (*.scdoc) was then transferred to the meshing software, ICEM CFD 17.2, with the Workbench interface. ICEM CFD is a surface-based meshing software and offers significantly more manual controls over ANSYS Meshing, the software used in previous attempts. It is surface-based in that in ICEM CFD, only *surfaces*, *curves* (i.e. edges) and *points* (i.e. vertices) are extracted from the CAD geometry. Solid regions were only represented by the generated mesh, rather than stored within the ICEM CFD pre-mesh geometry data.

3.2.2.2. Build topology

Although ICEM CFD offers an automated way to fix geometry errors and gaps as those depicted in Figure 3, it has its own limitations in that the user can specify only one tolerance value, smaller than which the edges of solids are merged. Nevertheless, this feature, named *Build Topology*, significantly simplifies the process given that it is extremely difficult to fill *all* gaps in the CAD software.

As a result, the *Build Topology* feature was run once to build a fixed geometry for the meshing step, with an appropriate tolerance value. (The tolerance value was arbitrary and geometry-dependent, but it usually lied on the scale of 100 μm in the geometries considered in this work.) ICEM CFD would then warn the user with a map of the connectivity of *curves*. Ideally, most of the curves should be connected to 2 surfaces since a curve connected to 1 surface implies that the surface is lying in open area.

3.2.2.3. Grouping the surfaces

The next step was one of the most time-consuming steps. In this step, *all* the surfaces were manually grouped and then the group named for future identification. Such a group is termed a *part* in ICEM CFD. For example, the surfaces which constitute the interface between the air in the tunnel and tunnel concrete wall were grouped and the *part* was named as “IFACE_TUNNEL_TUNNELAIR_TUNNELCONCRETE.” The naming process enabled the user to specify maximum sizes of the elements in contact with the surfaces within the group and the group was later read into the solver to specify boundary conditions on all the surfaces belonging to the group. It was as well easier to report results after solution since all the involved surfaces were grouped. In this example, one could directly output the heat flux between the air in the tunnel and the tunnel concrete wall from the solution by specifying the group.

It is important to note that interfaces between two fluid or solid regions must be handled with care. In principle, surfaces belong to either one of the two types, 1) exposed to free space, so that a fluid or solid region is on only one side of the surface; or 2) a fluid or solid region exists on both sides of the surface. Surfaces belonging to the same group must be of the same type, and if they are of type 2, it is required that the fluid or solid regions on the two sides of the surfaces are the same for all the surfaces within the group. In this example, all the surfaces within the group had TUNNELAIR on one side and TUNNELCONCRETE on the other side. This facilitated unambiguous specification of boundary conditions in the solver. Otherwise, the solver would separate the group until the requirement was fulfilled and lead to confusion.

The *curves* and *points* in the geometry were all placed into one single group since they had no real effect except indicating the boundary for the meshing algorithm.

Material points were then added to the supposed solid and fluid regions. During meshing, ICEM CFD identifies a region, bounded by its surfaces and in which its material point is found, and then meshes the region, for every material point specified.

For example, the material point TUNNELCONCRETE was placed within the region bounded by the tunnel wall surfaces.

3.2.2.4. Specify maximum sizes

It was then required to specify the maximum sizes of elements in contact with the surfaces within each group. The general guideline is that the user should specify a finer mesh in regions of high gradients or of significant interest. Depending on the problem, the user must consider whether to resolve the viscous sublayer or use a wall function for near-wall flows. Ideally, the near-wall mesh should be at the appropriate size to achieve the target y^+ value for the first element. In this work, since heat transfer is of the highest interest, and flow separation was expected from the blunt features of the module, it was more desirable to resolve the viscous sublayer. A target y^+ value of 1 was placed for the first element. However, for such a complex problem, estimation was not straightforward, and a post-simulation verification might be necessary. In specifying the maximum sizes, the sizes must be a series multiplied with powers of 2. For example, if the smallest maximum size is 1 mm, the other specified sizes should be one of the values in the series 2 mm, 4 mm, 8 mm, 16 mm, etc. This is to satisfy the Octree meshing algorithm [5].

Apart from maximum element sizes, *Curvature/Proximity Based Refinement* was also enabled such that for small features and curves, the meshing algorithm would automatically refine locally the mesh to represent the geometry until the pre-set “Min size limit” was reached [5].

The Octree method was used to generate the mesh. It is a robust and straightforward meshing method. An overview of how the Octree algorithm works can be found in [6].

3.2.2.5. Mesh checking

After mesh computation, a mesh check was performed with default settings in ICEM CFD. If the geometry in ICEM CFD is clean, the user should not expect a lot of errors in this step. Usually, duplicate elements can be safely deleted, and multiple edges can be safely ignored. Unconnected vertices were removed.

3.2.2.6. Comments on prism layers

Prism layers are usually desired in the boundary layer regions because of the high gradients perpendicular to the direction of the flow. It significantly reduces the number of elements necessary in the near-wall regions and increases numerical accuracy. However, such layers are only easily generated when the geometry is relatively simple. With the module, selecting which surfaces to generate prism layers became a problem since the flow was highly complex. Generating the layers almost always introduced errors, and given the time available with this work, prism layers were not pursued. A very fine mesh was used in these regions instead, for robustness of mesh generation, at the expense of computational resources since the number of elements increased considerably without prism layers.

3.2.2.7. Smoothing

With an error-free mesh from the checks performed in Section 3.2.2.5, the mesh was then smoothed. Smoothing the mesh improves mesh quality. The user specifies the number of smoothing iterations and the up to quality value. ANSYS recommends a quality of 0.15 for complicated models [6]. If time is sufficient, mesh elements with the lowest qualities can be highlighted and improved manually.

3.2.2.8. Manual mesh checking

It is important to do a manual checking of the mesh at some point after the initial meshing. The user may check for the element sizes, especially in the near-wall regions; and that all regions that were intended to be meshed were indeed meshed.

3.2.2.9. Boundary conditions and output

Boundary conditions were then set within ICEM CFD. All the surfaces with a mesh on one of its sides could have their boundary conditions specified at this step. Two-sided surfaces were left to be configured later. The mesh in ICEM CFD was then translated and output to the mesh format of the solver.

3.2.3. Solution

3.2.3.1. Solution on the CERN cluster

The chosen solver was ANSYS Fluent, a widely used solver for CFD studies. It is robust and has a wide range of models to fit with the problem. CFD case files from Fluent were uploaded to the CERN cluster to solve and result files were downloaded, automatically.

3.2.3.2. Importing into Fluent

The mesh output from ICEM CFD (*.msh) was passed to ANSYS Fluent for solving, using the Workbench interface. Fluent was set to open the mesh and set up the case file as double-precision. Parallelisation of the mesh on the local workstation was not necessary, since this could be done on the cluster.

3.2.3.3. Case setup

This section includes a step-by-step setup guide for the Fluent case file, for the SAS-only case (Section 3.7). Changes to the settings for the main-beam-tunnel-wall case are to be described accordingly in Section 3.9.

General

The first step in Fluent was to check the mesh. Fluent checks the mesh for integrity and errors, and the mesh *must* pass this step. The user may also request a mesh quality report for reference. A pressure-based solver was used, with absolute velocity formulation. The simulation was steady-state. Gravity was set to 9.80665 m/s^2 in the appropriate direction.

Models

The energy equation was turned on. Turbulence was modelled with the SST k-ω model (see Section 3.3), with default model constants and options. Radiation was modelled with the Discrete Ordinates model (see Section 3.5.2), with *Energy Iterations per Radiation Iteration* set at 10. *DO/Energy Coupling* was turned off (see Section 3.5). *Solar Load* was turned off as well. *Angular Discretization* was set to have these values: *Theta Divisions* = *Phi Divisions* = 3; and *Theta Pixels* = *Phi Pixels* = 1. *Number of Bands* was set to 0.

Materials

Depending on the problem (Sections 3.7 and 3.9), the number of materials in the domain might vary. Nevertheless, these materials were common: liquid water, air, copper, and aluminium.

The default material properties stored in Fluent for these materials were used, except for the density of air. The density of air was modelled with the incompressible ideal gas law. For all the materials, the absorption and scattering coefficients were set to 0, and the refractive index was set to 1; since no absorption, scattering, or refraction of the fluids would be taken into account in this simulation.

Cell zone conditions

Appropriate materials were assigned to the cell zones, which should have been clearly defined in the meshing step. None of the materials participated in radiation, except air in the tunnel and water in the pipes. The heating elements were set to have a constant source term for the appropriate amount of heat generation, in terms of W/m^3. The volume of the heating elements could be obtained from the CAD file.

For *Operating Conditions*, the operating pressure was left as default, at 101325 Pa. An appropriate value reduces round-off errors. Gravity should have been enabled already due to the setting in *General*. The operating temperature was irrelevant since the Boussinesq model was not used in estimating density change. An operating density was specified at 1.1839 kg/m^3, the corresponding density for 25 °C air [7].

Boundary conditions

The boundary conditions are described in the respective sections in each case. See Sections 3.7.4 and 3.9.4.

Reference values

Reference values could be used for reporting values such as heat transfer coefficients, by setting a reference temperature, for example. This was not set for the two cases.

Solution methods

The *Coupled* scheme was used for pressure-velocity coupling. For spatial discretisation, *Gradient* was set as *Least Squares Cell Based*. *Pressure* was set to *Second Order*. *Momentum*, *Turbulent Kinetic Energy*, *Specific Dissipation Rate*, *Energy*, and *Discrete Ordinates* were all set to *Second Order Upwind*. *Pseudo Transient* was enabled.

Solution controls

Relaxation factors were set at this step. These values were important in maintaining stability of the solution. After several trials, these values are used for the SAS-only case: 0.8 for *Pressure*; 0.8 for *Momentum*; 1 for *Density*; 1 for *Body Forces*; 0.75 for *Turbulent Kinetic Energy*; 0.75 for *Specific Dissipation Rate*; 1 for *Turbulent Viscosity*; 0.65 for *Energy*; and 1 for *Discrete Ordinates*.

Under Advanced/Expert, all three equations (i.e. *Turbulent Kinetic Energy*, *Specific Dissipation Rate*, and *Energy*) were enabled for the pseudo transient method. The time scale factor for turbulent kinetic energy and specific dissipation rate was set to 10; whereas the time scale factor for energy was set to 100.

Monitors

Several monitors were set for monitoring the iteration progress. For example, in the SAS-only case (Section 3.7), the following values were monitored: mass balance of air; mass balance of water; total heat to air (specified on SAS surfaces); total heat to water (specified on SAS and pipe surfaces); radiation heat passing through the domain boundaries; net radiation heat from the SAS in contact with air; total heat from the heat source; mass-weighted average of the water temperature just before it enters the structure and just after it leaves the structure; and the enthalpy flow rate of air and water into and out of the domain.

Solution initialisation

Hybrid initialisation was used, with 25 iterations.

Run calculation

Under *Pseudo Transient Options*, *Time Step Method* in *Fluid Time Scale* was set to *Automatic*, with *Timescale Factor* at 1. *Length Scale Method* was selected to be *User Specified*, with *Length Scale* at 0.5 m (i.e. the length of one SAS) for the SAS-only case. *Verbosity* was set to 1 so that the time scales were printed to the console during iterations. *Time Step Method* in *Solid Time Scale* was set to *Automatic*, with *Timescale Factor* at 1000.

It was set to run for 500 iterations.

3.2.3.4. Convergence criteria

To determine convergence some criteria had to be set. This mainly included the residuals, the stability of the solution, as well as the mass and energy balances. Normally the residuals should reduce over iterations. Scaled residuals were reported and they depended on initial guesses of the solution. The second criterion was the stability of the solution. This was judged with the stability of the monitored variables, described in the sub-section Monitors above. They should be within a range of tolerance and should not be oscillating. The third criterion was the balances. Since both mass and energy were conserved, any imbalances were a significant warning to the solution validity.

3.2.3.5. Input and output parameters

The ANSYS Workbench environment allows the parameterisation of problems, in which the user can specify input and output parameters; and perform what is known as a design point study. This is especially convenient when the problem is large, since the user does not have to open the Fluent case (and data) file(s) to adjust the input parameters (or obtain the values of the output parameters).

For the SAS-only case, the input parameters were: speed and temperature of the air into the domain; backflow temperature of air at the air outlet; ambient emissivity and temperature (for radiation calculations); emissivity of copper; heat generation of the heat sources (per unit volume); mass flow rate and temperature of water into the domain; backflow temperature of water at the water outlet; and the target mass flow rate of water at the water outlet.

The output parameters were basically the same as the monitored values in Section 3.2.3.3: mass balance of air; mass balance of water; total heat to air (specified on SAS surface); total heat to water (specified on SAS and pipe surfaces); radiation heat passing through the domain boundaries; net radiation heat from the SAS in contact with air; total heat from the heat source; mass-weighted average of the water temperature just before it enters the structure and just after it leaves the structure; and the enthalpy flow rate of air and water into and out of the domain.

3.2.4. Post-processing and visualisation

3.2.4.1. Results of interest

There were two main types of results of interest. The first was the heat dissipation values to air, to water, and to soil (in the main-beam-tunnel-wall case). The second was the temperature and velocity fields of the computational domain.

3.2.4.2. Visualisation

Sometimes it may be worth to visualise the flow field or the temperature field of a cross section. One may want to inspect the temperature uniformity over a cross section of the accelerating structure, or over the length of the module.

The bottom line of visualisation is to inspect whether the flow field and the temperature field match with physics, and what is expected before the simulation.

3.3. Turbulence model

3.3.1. Reynolds-averaged Navier-Stokes (RANS) equations

The flow in the tunnel is turbulent. Assuming that the tunnel cross-section is circular so that the air flow can be approximated as a pipe flow, an air speed of 0.4 m/s and a tunnel inner diameter of 5.6 m (tunnel cross section in Figure 80) give a Reynolds number of approximately 140’000, well above ~ Re 2’300 for transition to turbulent flow. Given the limitation of computational resources and that time-dependent flow features were not the interest of this work, a time-averaged steady-state solution was desired. A turbulence model was chosen to solve the Reynolds-averaged Navier-Stokes (RANS) equations.

The RANS equations are obtained by time-averaging the Navier-Stokes (NS) equations, which introduces additional unknowns known as Reynolds stresses. A proper turbulence model for these Reynolds stresses must be chosen to close the set of equations.

3.3.2. The shear-stress transport (SST) k-ω model

k-ω models are generally more accurate than k-ε models in calculating boundary layer separation [8]. Moreover, the formulation of k-ω models in Fluent is y^+-insensitive [9]. This circumvents the problem described in 3.2.2.4 in that the y^+ value of the first element cannot be accurately predicted at every point on the solid surface beforehand in complex problems. The model allows flexible y^+ value for the first element given that it still lies in the logarithmic layer, and switches between modes of near-wall resolution and near-wall modelling.

In this work, an improvement to the standard k-ω model, the shear-stress transport (SST) k-ω model was used. Compared to the standard k-ω model, the SST k-ω model is less sensitive to freestream values of k and ω [8]. This was desirable since these values were not necessarily known at this stage.

3.4. Buoyancy effects

Buoyancy effects were accounted for in the simulations from the change in density of air with temperature. The density of water was assumed to be constant. The buoyancy effects were modelled with the incompressible ideal gas law. Nevertheless, buoyancy effects were secondary since the change in density was minimal and there was forced convection of air over the module.

3.5. Radiation model

3.5.1. Contribution from radiation exchange

It was thought in the earlier parts of the project that contribution from radiation was significant and shall not be neglected. It was from the estimation with the following equation:

$$Q = \sigma A(T_H^4 - T_L^4)$$

To model radiation exchange between the module and the tunnel wall, an appropriate radiation model in Fluent had to be chosen. This discussion is to follow shortly. Although it was later discovered that the heat dissipated by radiation from the structure was overestimated because of an overestimation in the emissivity of copper (see Section 3.7.5.4), radiation modelling constituted a supplementary part which improved the accuracy of simulation results.

For the SAS-only case, radiation was modelled for air and water regions. For the main-beam-tunnel-wall case, radiation was modelled only for the air regions.

3.5.2. Radiation models in Fluent

There are a few available radiation models in Fluent, namely, Rosseland, P1, Discrete Transfer Radiation Model (DTRM), Surface-to-Surface (S2S), and Discrete Ordinates (DO). The choice of the radiation model followed the guideline given in [9]. Since the problem had a low optical thickness, and Rosseland and P1 models are for optically thick problems, they were not considered [9]. Moreover, the Rosseland model is insensitive to emissivity [9]. Although DTRM and DO require much more computational resources, they are suitable for all optical thicknesses [9] and were therefore preferred.

3.5.2.1. Surface-to-Surface (S2S)

Before going to the DTRM and DO models, the S2S model is worth some discussion. It is recommended in modelling “enclosure radiative heat transfer with non-participating media” [9], which is exactly the configuration with the module inside the “enclosure” of the tunnel wall. When the media (i.e. water or air) does not participate in radiation, the S2S model is more efficient than models which consider participating media [9].

The initial case was set up with the S2S model enabled. It had soon become clear that this model was not feasible because of the complexity of the geometry. In principle, the S2S model computes the *view factor* between surface elements, that is, the surface of the geometry is first divided, and then computed to determine whether one surface element “sees” another surface element [9]. This approach, with a complex geometry (fine details and curvature) of the module, requires unreasonably high resolution in performing view factor computation. This in turn requires significant time because this cannot be computed on the cluster. The resulting view factor values, at the same time, were not accurate enough for the considered geometry and produced significant errors which were non-physical.

3.5.2.2. Discrete Transfer Radiation Model (DTRM)

The DTRM model approximates radiation leaving a surface with discrete rays [9]. The number of discrete rays is controlled by the angular discretisation specified by the user. Fluent performs a ray tracing step before the main solution step and creates a “ray file” for radiation calculation [8]. Although this model is straightforward and elegant, its implementation in Fluent does not allow parallel processing [9], thus rendering it impossible to use with the current problem.

3.5.2.3. Discrete Ordinates (DO) model

The DO model then became the last remaining choice of radiation models available in Fluent. The DO model is capable of a large number of effects, such as semi-transparent walls, specular walls, and scattering [9], although only some of them were used in the current problem.

The DO model solves the radiation intensity transport equations in different directions. The number of such directions is defined by the number of discrete solid angles from the discretisation process [9]. Similar to the DTRM model, the angular discretisation fineness is controlled by the user. The DO model is solved in the same way as fluid flow and energy equations [9].

The coupling between the energy and radiation intensity equations is recommended when the optical thickness is larger than 10 [8]. Since the optical thickness was small for the current problem, the coupling was not enabled.

The uncoupled DO model was chosen for modelling radiation exchange in this work.

3.6. Periodicity

Ideally, the model and the mesh should be set up to be ready for periodic flow computation. When the flow is fully developed within the tunnel, the entire length of the collider can be split to the smallest repeating unit, or a module, and the flow field should be approximately equal over each module, neglecting buoyancy effects from temperature changes.

There are two ways to approach the periodicity problem. The first pseudo-periodic approach is a manual approach to achieve periodic flow. The second periodic heat transfer approach is built into Fluent.

3.6.1. Pseudo-periodic

The pseudo-periodic approach is simple to apprehend. In a computational domain containing the smallest repeating unit and the boundary (tunnel wall), where there is a main flow direction, the flow is solved once. A velocity profile, which should correspond to the intended air mass flow rate, is specified at the inlet for this first solution. The exact profile does not matter. In the second step, the velocity profile at the outlet is taken and input as the inlet velocity profile. This process is repeated manually until the difference in the inlet and outlet velocity profiles is within a tolerance. It may be helpful to have the exactly identical geometry for both inlet and outlet to help convergence. Also, having the same surface mesh at the inlet and outlet eliminates the error of interpolation. The result from this process is a fully developed flow over the module in the tunnel.

3.6.2. Periodic heat transfer

Fluent allows the computation of periodic heat transfer setups by including one module only [8]. The considered case is termed as “streamwise-periodic” flow in Fluent, in which there is a constant pressure drop across the periodic boundaries [8].

For periodic heat transfer setups, thermal boundary conditions of constant wall temperature or constant wall heat flux are allowed in Fluent, and these two boundary conditions cannot co-exist in the problem [8]. The implementation in Fluent imposes a number of limitations of the case setup, including that solid regions cannot be next to periodic planes; and that fluid density cannot be a function of temperature [8]. These limitations imply that the problems have to be modified to a certain extent in order to satisfy Fluent’s requirements. Volumetric heat sources such as those of the heating elements may introduce extra complexity.

The most straightforward implementation of the periodic heat transfer setup would be a case of specified constant wall heat flux out of the domain. In such case, there is a temperature gradient σ across a periodic length L, as in the following equation given in [8]:

$$\frac{T(\vec{r}+\vec{L})-T(\vec{r})}{L}=\frac{T(\vec{r}+2\vec{L})-T(\vec{r}+\vec{L})}{L}=\sigma$$

The temperature gradient σ is in turn related to the heat transfer in or out of the periodic domain.

A step-by-step guide is provided in [8] for solving streamwise-periodic flow with periodic heat transfer in Fluent.

Due to time limitations, the two approaches above have not been implemented. They may be of interest in future work.

3.7. Super accelerating structure, SAS-only case

3.7.1. First case as proof-of-concept

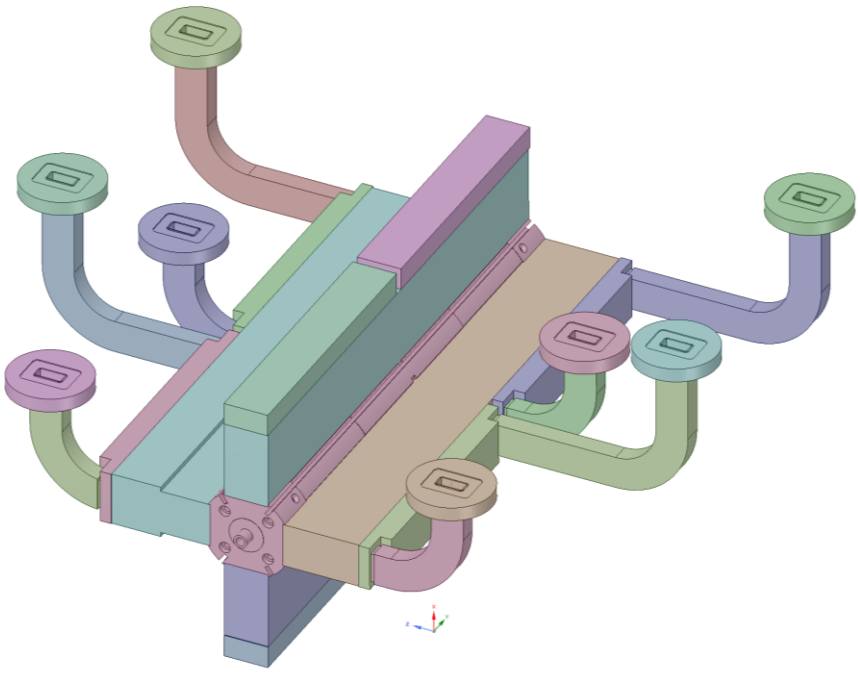

Figure 4: Super-accelerating structure

As a first case, one SAS was taken from the module as a proof-of-concept test for the CFD approach. Figure 4 shows a slightly simplified CAD model of an SAS. In actual CFD analysis a more simplified model was used. Various scenarios were then tested with this geometry to find suitable models for fluid flows and radiation. These models and settings have already been presented in Section 3.2. With the insights gained, the same models and settings were used on the more complete case involving the main beam part of the module and the tunnel wall in Section 3.9.

3.7.2. Problem definition

One SAS was placed in a “free” space where the domain boundaries were sufficiently far away from the structure.

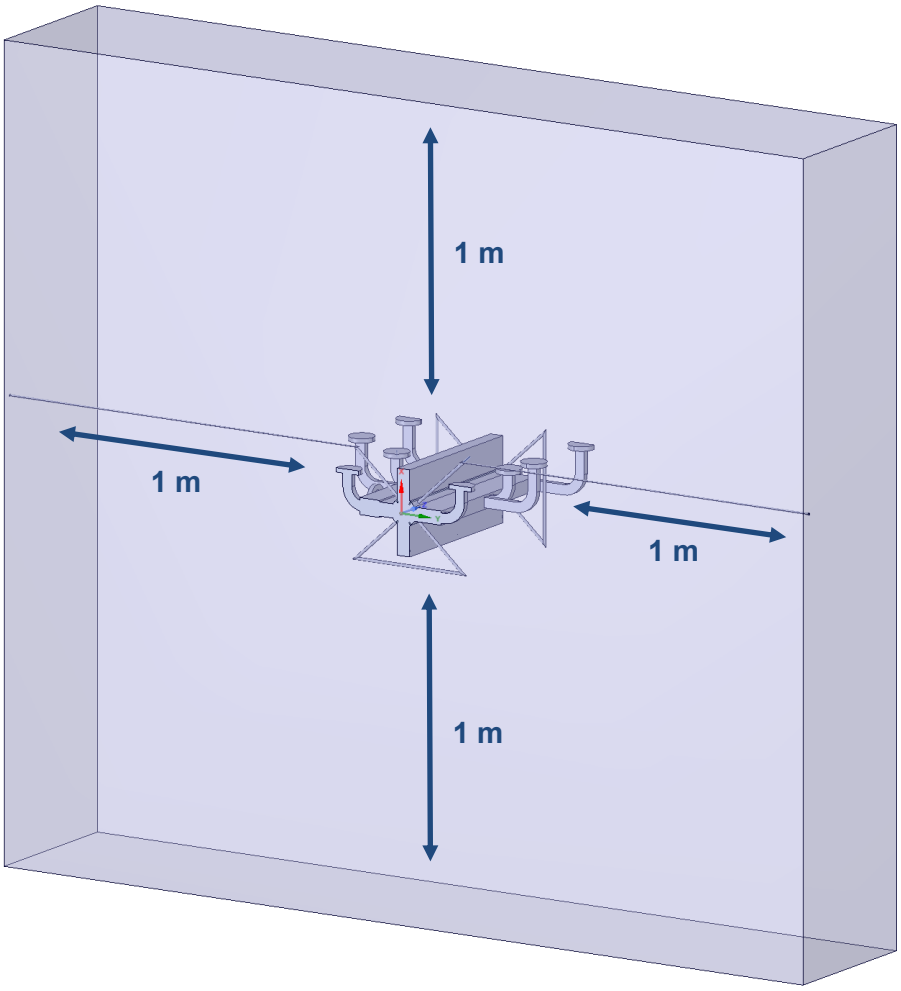

Figure 5: Computational domain, SAS-only

Figure 5 shows an SAS placed in “free” space 1 m away from the domain boundaries. The simplified SAS geometry was taken from the previous work of A. Vamvakas. The water pipes were artificial and extended to the domain boundaries, but they were expected to have a negligible effect on the air flow because of their small size. The effect of the artificial geometry in heat dissipated to water was minimal, because the modified geometry was external to the structure. The water pipe within the SAS, where most heat transfer to water takes place, was not modified.

The pipes had an inner diameter of 6 mm and were made of copper. They were assumed to be thermally bonded to the SAS, which was as well made of copper. Air was modelled to have variable density with temperature using the incompressible ideal gas law. Water was assumed to have constant density.

In this simplified geometry, the ends of the SAS were slightly cut in the streamwise direction. This was to avoid the problem of a too sudden change in geometry in air flow which hinders convergence in this particular case.

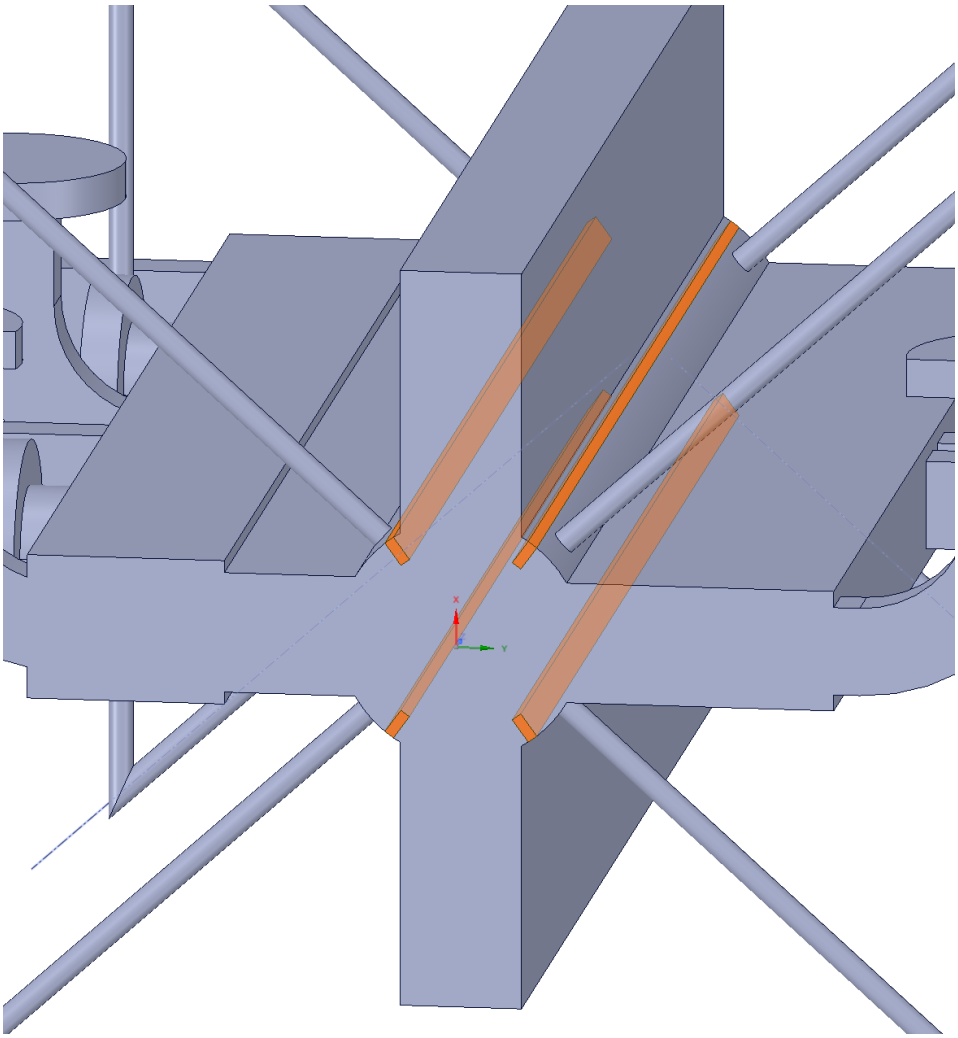

Figure 6: Location of the heating elements of the SAS

For heat sources, heating elements made of aluminium were used instead of an internal heat source originating from the cavity (Figure 6). This was to correspond to the setting from the experimental approach in Section 2.4. For one SAS, the heat generated was 780 W.

3.7.3. Meshing

The mesh was generated from the steps described in Section 3.2.2. A tetrahedral mesh was generated with the Octree method. For the finest mesh, there were approximately 43 million elements, while coarser meshes were generated for mesh independence tests. The smallest maximum size of elements was set to 1 mm.

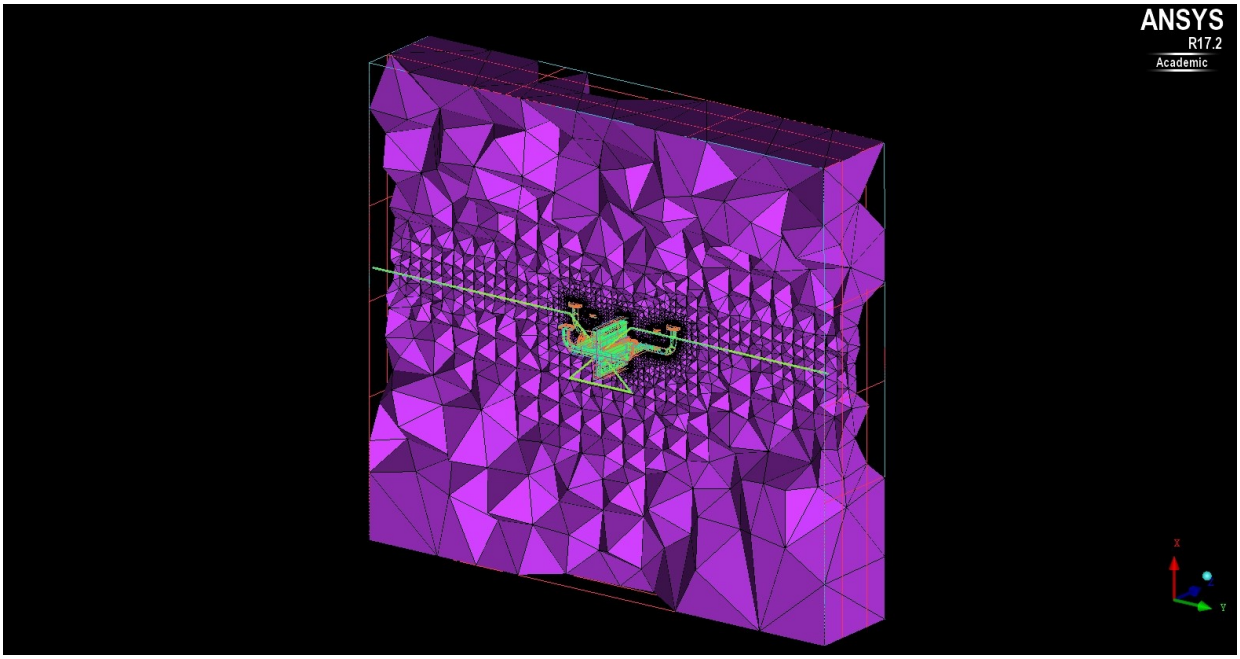

Figure 7: Cross section of the mesh, SAS-only

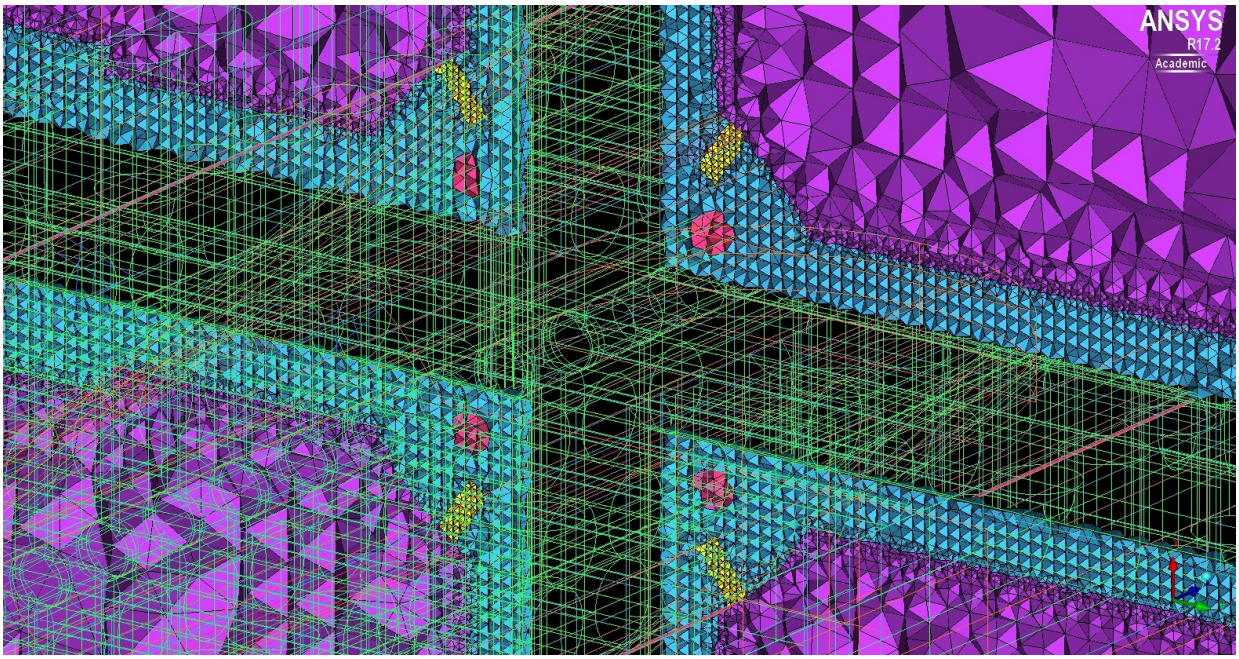

Figure 8: Cross section of the mesh showing different regions, SAS-only

A cross section of the mesh is shown in Figure 7. Figure 8 shows a cross section with different fluid/ solid regions. The yellow region corresponds to the rectangular heating elements, and the SAS copper region has a sky-blue mesh. The air mesh is purple in colour and the water mesh is magenta in colour.

All of these fluid and solid zones were coupled in the solution process and solved simultaneously.

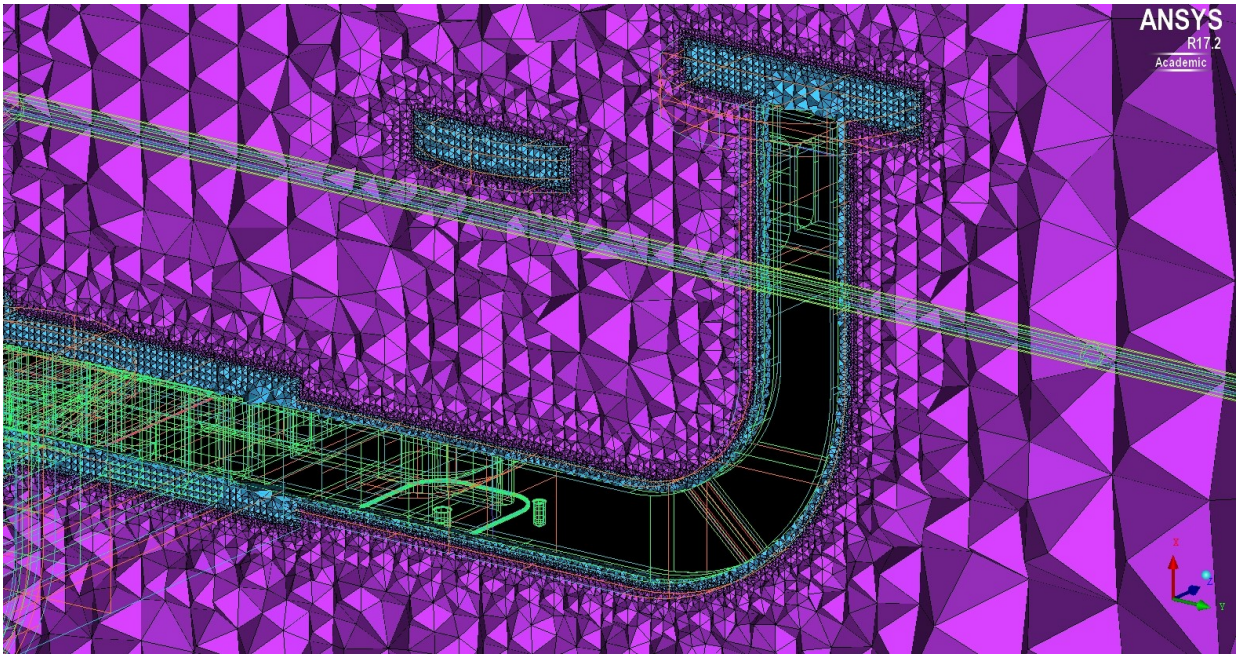

Figure 9: Cross section of the mesh, waveguides, SAS-only

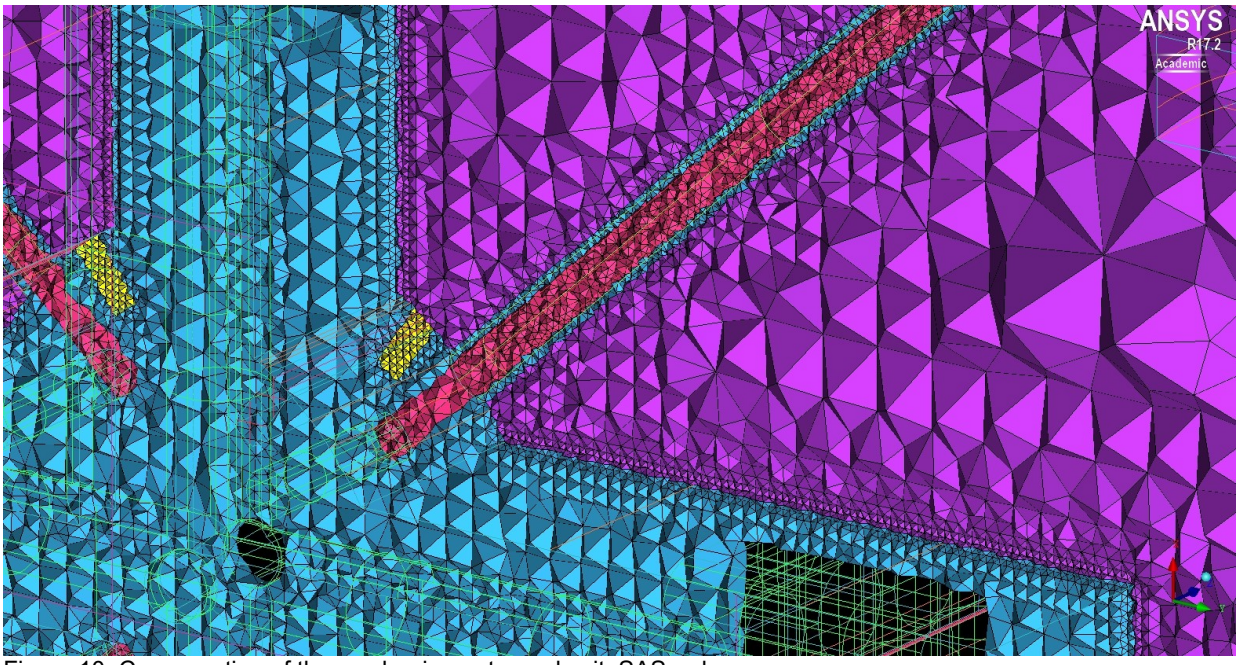

Figure 10: Cross section of the mesh, pipe entry and exit, SAS-only

Figure 9 and Figure 10 are two other cross sections of the mesh. In Figure 9, the waveguide is shown. The empty region in black indicates the lack of mesh for this vacuum. Figure 10 shows the mesh at the position where the pipe entered and left the SAS. It can be seen that the mesh of the SAS and the mesh of the pipe wall were connected as one single solid region.

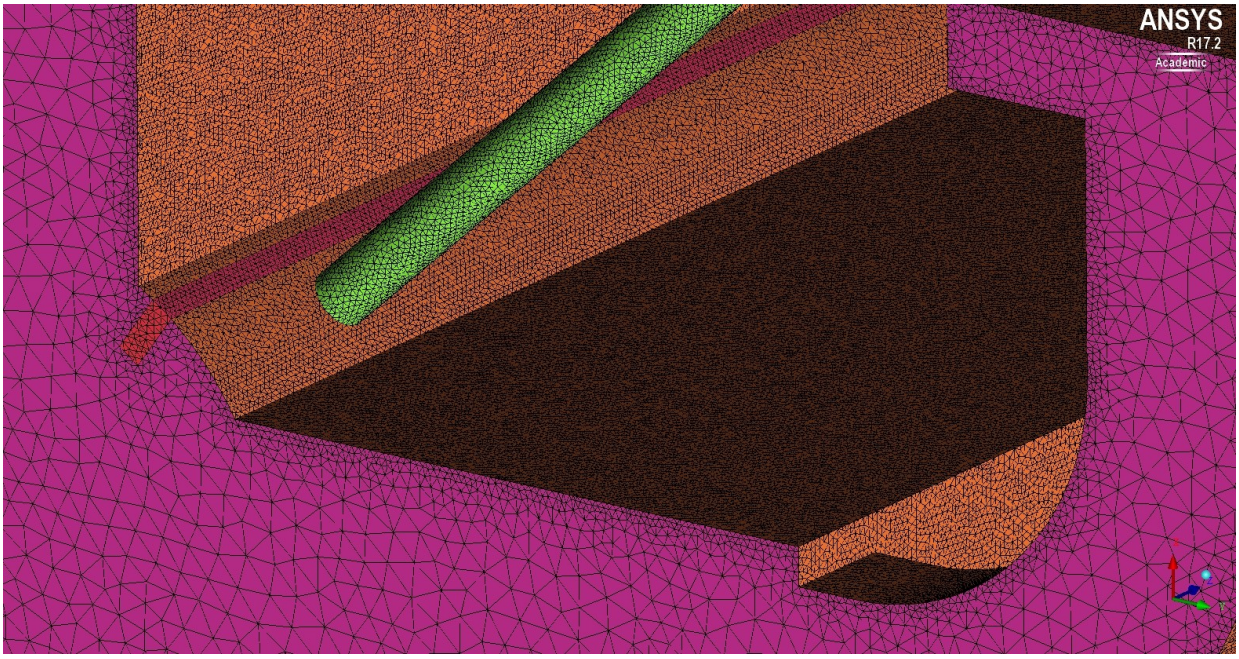

Figure 11: Surface mesh, SAS-only

Figure 11 shows the surface mesh of the SAS. Note that the colours are only for visibility of the surfaces and are different from those from Figure 7 to Figure 10.

3.7.4. Boundary conditions

3.7.4.1. Types of boundary conditions

There are a few types of boundary conditions, namely momentum, thermal, and radiation. In the follow sections, they are discussed by considering different parts of the domain.

3.7.4.2. Domain boundary (air)

Inlet

At the inlet, an inlet velocity was specified to be normal to the boundary at a certain temperature, both were input parameters in Workbench. The turbulence parameters were specified with the default *Turbulent Intensity* (5%) and *Turbulent Viscosity Ratio* (10). For radiation, the *External Black Body Temperature Method* was set to *Boundary Temperature* and *Internal Emissivity* was set to 0.

Outlet

At the outlet, a pressure outlet (type *pressure-outlet* in Fluent) was specified with *Gauge Pressure* set to 0. The *Backflow Direction Specification Method* was set to *Normal to Boundary*. The backflow turbulence parameters were set to be the same as the inlet. The *Backflow Total Temperature* was set as an input parameter in Workbench, which was then set to be 4 – 5 °C higher than the inlet air temperature. For radiation, the *External Black Body Temperature Method* was set to *Boundary Temperature* and *Internal Emissivity* was set to 0.

Note that the *outflow* boundary condition should not be specified in Fluent for the outlet when solving for heat transfer problems with two fluids separated by a solid region, or there would be convergence issues. See Section 13.2.1.2 in [8].

Sides

At the domain boundary for air, it was assumed that the boundary was sufficiently far away from the SAS. The momentum boundary condition of zero shear stress on air was thus imposed (in Fluent, *Shear Condition/ Specified Shear*). For the thermal boundary condition, *Thermal Conditions* was set to *Radiation*. *External emissivity* was set to 1; *External Radiation Temperature* was set as an input parameter in Workbench, which would be at the same temperature as the inlet air temperature; and *Internal Emissivity* was set to 0. The domain boundary was set to be transparent to radiation (*BC Type* set to *semi-transparent* under the *Radiation* tab, other settings in the tab left at default).

3.7.4.3. Domain boundary (water)

Inlet

A mass flow rate was set at the inlet normal to the boundary (type *mass-flow-inlet* in Fluent), at a certain water total temperature (it was assumed that the total temperature equals the static temperature); both were input parameters in Workbench. The turbulence parameters were the same as those for the air inlet boundary in Section 3.7.4.2. For radiation, the *External Black Body Temperature Method* was set to *Boundary Temperature* and *Internal Emissivity* was set to 0, same as that in Section 3.7.4.2.

Outlet

A pressure outlet (type *pressure-outlet* in Fluent) was specified with *Gauge Pressure* at 0. The *Backflow Direction Specification Method* was set to *Normal to Boundary*. A target mass flow rate was set as the negative of the mass flow rate specified at the inlet, which was also a parameter in Workbench. The backflow turbulence parameters were set to be the same as the inlet. The *Backflow Total Temperature* was set as an input parameter in Workbench, which was then set to be 3 °C higher than the inlet water temperature. For radiation, the *External Black Body Temperature Method* was set to *Boundary Temperature* and *Internal Emissivity* was set to 0.

Similarly, the *outflow* boundary condition should not be specified, as described in Section 3.7.4.2.

3.7.4.4. Domain boundary (solids)

For surfaces adjacent to solid zones and form part of the domain boundary, they were of type *wall* in Fluent. There was no momentum boundary condition applicable. *Thermal Conditions* was set to *Heat Flux*, with zero heat flux across the surface. The setting *Internal Emissivity* had no effect, since radiation was not solved inside solid zones. Under the *Radiation* tab, *BC Type* was set to be opaque.

3.7.4.5. SAS

Boundary conditions were specified on *surfaces*. There were two types of surfaces for the SAS. The first type separated an unmeshed region (vacuum e.g. found in the beam cavity) and the copper region of the structure. These were just *walls* in Fluent. The second type of surfaces were *interfaces*. They separated regions of meshes representing different materials. For example, an interface can separate the copper region of the SAS and the air region of the tunnel. These were the surfaces where the coupled boundary condition applies.

There was not much one could specify for the first type. There were no adjacent fluid regions, so momentum boundary conditions did not apply. It was assumed that no heat flux crossed the wall, same as the domain boundary setting for solids. Radiation had not been modelled here, and it would not have been possible since for radiation transport in the DO model a mesh was necessary in this vacuum region.

The second type of surfaces was automatically identified by Fluent when reading the mesh. They were automatically set to be *Coupled* under *Thermal Conditions*. On the air side, a no-slip wall was specified. *Internal Emissivity* was set to be the emissivity of copper, an input parameter in Workbench. Under the *Radiation* tab, *BC Type* was set to be *opaque*. On the copper side, the setting *Internal Emissivity* had no effect since radiation was not solved in solid zones. Under the Radiation tab, *BC Type* was set to opaque.

3.7.4.6. Heating elements

The heating elements were specified to have a volumetric heat generation which gave a total of 780 W for the four heating elements in one SAS. Similarly, the surfaces of the heating elements had coupled thermal boundary conditions between the aluminium zone of the heating elements and the air zone, or the copper zone on the other side of the surface.

On the air side of the air-aluminium interface, a no-slip condition was specified. *Internal Emissivity* was set to 1 and the surface was set to opaque. On the aluminium side, no momentum conditions were available. The setting *Internal Emissivity* had no effect since radiation was not solved in the solid zones. Under the Radiation tab, *BC Type* was set to opaque.

On the copper side of the copper-aluminium interface, no momentum conditions were available. The setting *Internal Emissivity* had no effect since radiation was not solved in the solid zones. Under the Radiation tab, *BC Type* was set to opaque. On the aluminium side, similarly, no momentum conditions were available. Similarly, the setting *Internal Emissivity* had no effect since radiation was not solved in the solid zones. Under the Radiation tab, *BC Type* was set to opaque.

3.7.4.7. Pipe

The pipes had similar boundary conditions as described in the previous sections.

Inner surface – Water side

At the inner surface of the pipe, a no-slip boundary condition was specified on the water side. *Thermal Conditions* was automatically set to *Coupled*. *Internal Emissivity* was set to the emissivity of copper, an input parameter in Workbench. Under the *Radiation* tab, *BC Type* was set to *opaque*.

Inner surface – Copper side

On the copper side, there was no momentum boundary condition. *Thermal Conditions* was automatically set to *Coupled*. The setting *Internal Emissivity* had no effect since radiation was not solved in the solid zones. Under the Radiation tab, *BC Type* was set to opaque.

Outer surface – Air side

At the outer surface of the pipe, a no-slip wall boundary condition was specified on the air side. There was no heat flux across the interface: *Thermal Conditions* set to *Heat Flux*, where heat flux was set to 0 and *Internal Emissivity* was set to the emissivity of copper, an input parameter in Workbench. Under the *Radiation* tab, *BC Type* was set to *opaque*.

Outer surface – Copper side

On the copper side, there was no momentum boundary condition. *Thermal Conditions* was set to *Heat Flux*, with heat flux set to 0. The setting *Internal Emissivity* had no effect since radiation was not solved in the solid zones. Under the Radiation tab, *BC Type* was set to opaque.

3.7.5. Results

3.7.5.1. Convergence

The cases achieved convergence with about 500 iterations. It took 6 hours on the CERN cluster with 32 cores for the finest mesh.

3.7.5.2. Results reporting

The results were reported with output parameters listed in Section 3.2.3.5. Heat dissipated to water and air were calculated from the differences in enthalpy flow rates at their respective inlet and outlet. For example, the heat dissipated to air was derived from the difference between air enthalpy outflow rate and air enthalpy inflow rate. The heat dissipated by radiation was given by the output parameter for radiation heat passing through the domain boundaries.

3.7.5.3. Mesh independence test

Mesh independence tests were performed by doubling and quadrupling the *Global Element Scale Factor* in ICEM CFD. The *Min Size Limit* under *Curvature/Proximity Based Refinement* was adjusted accordingly so that after scaling with the *Global Element Scale Factor* the resulting value was constant. This was necessary to resolve the smaller features in the geometry.

The results reported for different meshes are as follows:

Global Element Scale Factor	Air Inlet Temperature (°C)	Enthalpy Change Rate of Air (W)	Enthalpy Change Rate of Water (W)	Net Radiation Heat through Boundary (W)	Total Heat Dissipated (W)
1	21	54.112	699.12122	27.400854	780.634074
2	21	55.524	712.12822	27.1213	794.77352
4	21	56.486	693.07053	27.146991	776.703521
1	25	39.13833275	719.45096	21.168561	779.7578538
2	25	40.10631913	731.27496	21.048059	792.4293381
4	25	40.6591333	714.76958	21.065851	776.4945643
1	30	23.638	743.52126	12.880305	780.039565
2	30	24.317	756.4637	12.813536	793.594236
4	30	24.892	740.55073	12.7975	778.24023
1	35	5.77	769.79369	4.2262865	779.7899765
2	35	6.677	783.92678	4.2432718	794.8470518
4	35	6.862	767.80334	4.2001928	778.8655328

Table 1: Mesh independence test, copper emissivity 0.8, SAS-only

Global Element Scale Factor	Air Inlet Temperature (°C)	Enthalpy Change Rate of Air (W)	Enthalpy Change Rate of Water (W)	Net Radiation Heat through Boundary (W)	Total Heat Dissipated (W)
1	21	55.476	719.79986	3.4515551	778.7274151
2	21	56.077	731.96969	3.9837736	792.0304636
4	21	57.942	715.27261	3.437516	776.652126
1	25	40.31856632	736.36994	2.6824564	779.3709627
2	25	40.54064089	750.7891	3.2297047	794.5594456
4	25	41.854045	732.42454	2.6715439	776.9501289
1	30	24.599	753.62749	1.6418402	779.8683302
2	30	24.681	766.0872	2.2181591	792.9863591
4	30	25.859	750.53556	1.6306035	778.0251635
1	35	10.265	773.92195	0.55973696	784.746687
2	35	7.937	786.59862	1.2093298	795.7449498
4	35	7.752	770.81677	0.54976661	779.1185366

Table 2: Mesh independence test, copper emissivity 0.05, SAS-only

Table 1 gives the values for different meshes for a copper emissivity of 0.8. Table 2 gives the same values, except the copper emissivity was corrected to 0.05. Section 3.7.5.4 explains the change in the copper emissivity.

It can be seen that for most of the results, the three meshes with different element sizes gave fairly consistent values. There was an exception for the 2x mesh, where there was a systematic deviation of the values of the enthalpy change rate of water from those of other meshes for both copper emissivity values; and a deviation of the net radiation heat for the copper emissivity of 0.05. This might be due to some highly skewed elements located somewhere in the water pipes or these cases required much more iterations for proper convergence. The total heat dissipated for the 2x mesh also gave ~795 W for all the cases, which was 15 W larger than the nominal 780 W.

It was concluded that the element sizes were in the desired range, and that the 2x mesh was only an exception. The finest (1x) mesh was used to report the results.

3.7.5.4. Overestimation of copper emissivity

In the beginning the emissivity of copper was set to 0.8, and it produced an underestimation of heat dissipated to water. It was later known that the emissivity of copper had in fact been measured experimentally and it was more than one order of magnitude lower, at 0.05.

The results reported in this Section (3.7.5.4) are from an air inlet velocity of 0.4 m/s. The water inlet volume flow rate was 1.3 L/min, which was converted to an equivalent mass flow rate (density is constant for water in the simulation) for the boundary condition in Fluent. The water inlet temperature was 27 °C.

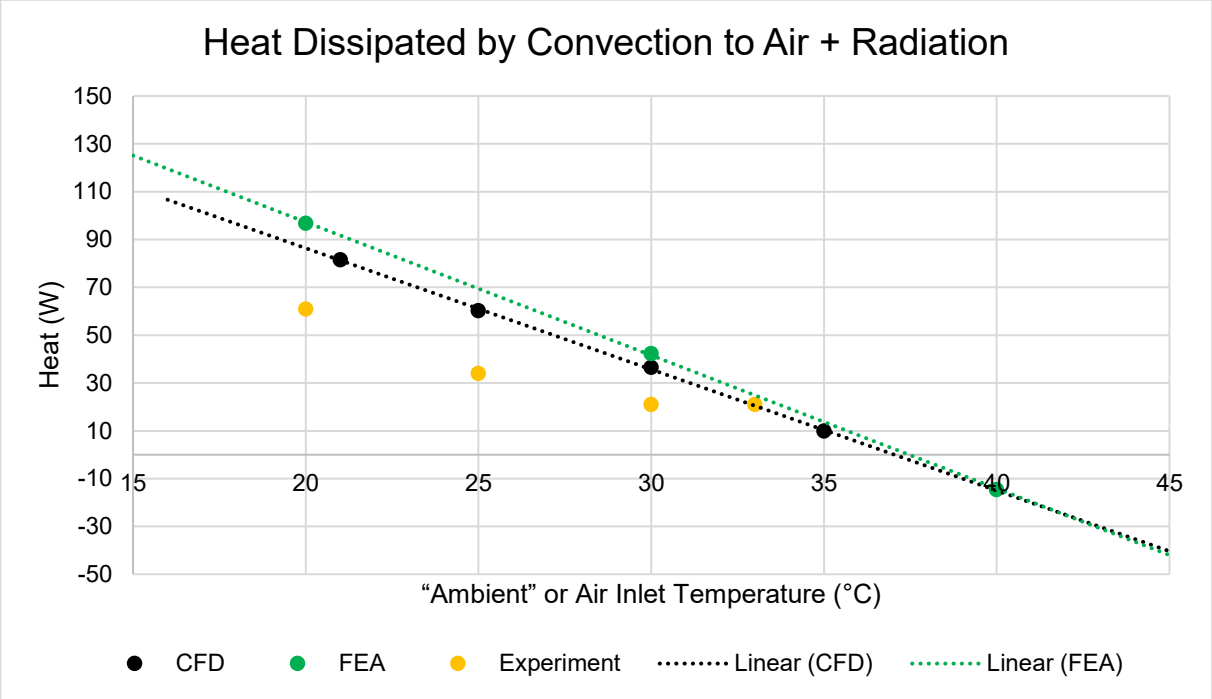

Figure 12: Heat dissipation values to air and by radiation at different air temp., SAS-only

Figure 12 shows the sum of heat dissipation values by convection to air and by radiation. The plot and the FEA values are from A. Moilanen. The experiment values are from V. Andavan and A. Vamvakas. Reporting the sum of the two heat dissipation values instead of separated values was necessary because it was not possible to distinguish between heat dissipation by convection and by radiation in the experiment with available sensors. It is noted that these values in the experiment were measured indirectly, that only the temperature change in water and the power input to the heating elements were actually measured. In this plot the finite-element (FEA) results have been adjusted according to the results from CFD. The adjusted air convective heat transfer coefficient was 6 W/(m^2·K). The water convective heat transfer coefficient was not adjusted and was chosen to be ~ 4000 W/(m^2·K). On the x-axis, air inlet temperatures were specified for CFD and ambient temperatures were specified for FEA. This is because in ANSYS Mechanical, one has to specify an "ambient" temperature on which the user input convection coefficient is based.

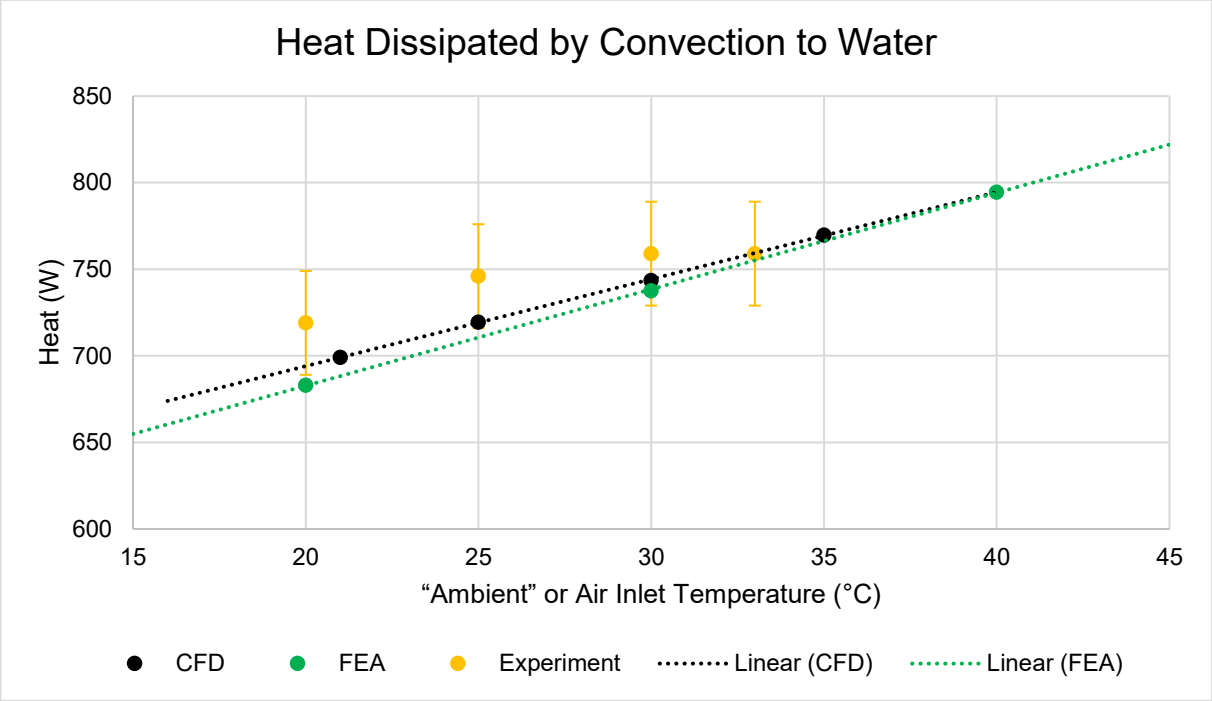

Figure 13: Heat dissipation values to water at different air temp., SAS-only

Figure 13 shows the heat dissipation values to water by convection. The plot and the FEA values are from A. Moilanen. The experiment values are from V. Andavan and A. Vamvakas.

One can easily observe from Figure 12 and Figure 13 that the numerical solutions underestimate the heat dissipated by convection to water and overestimate the sum of heat dissipation by convection to air and by radiation. This is due to the overestimation of the copper emissivity, as it becomes clear in Section 3.7.5.5, when compared to experiments.

3.7.5.5. After correction of copper emissivity

Incoming air at 0.4 m/s

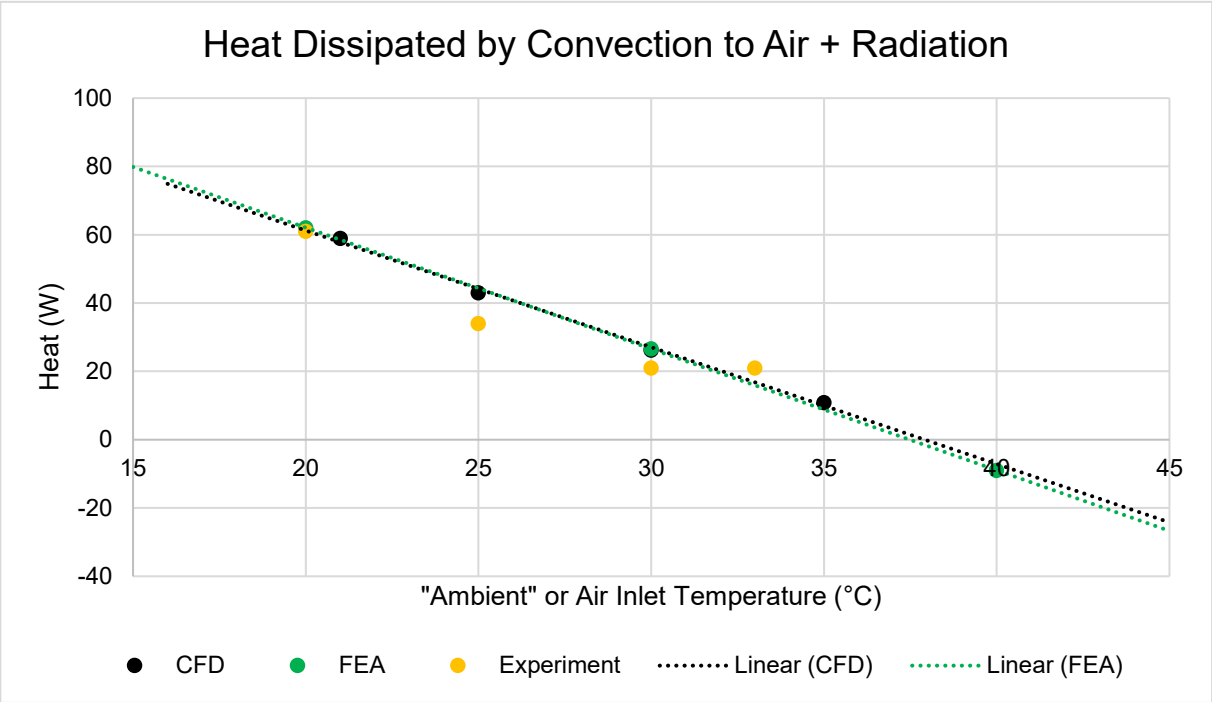

Figure 14: Heat dissipation values to air and by radiation at different air temp, SAS-only

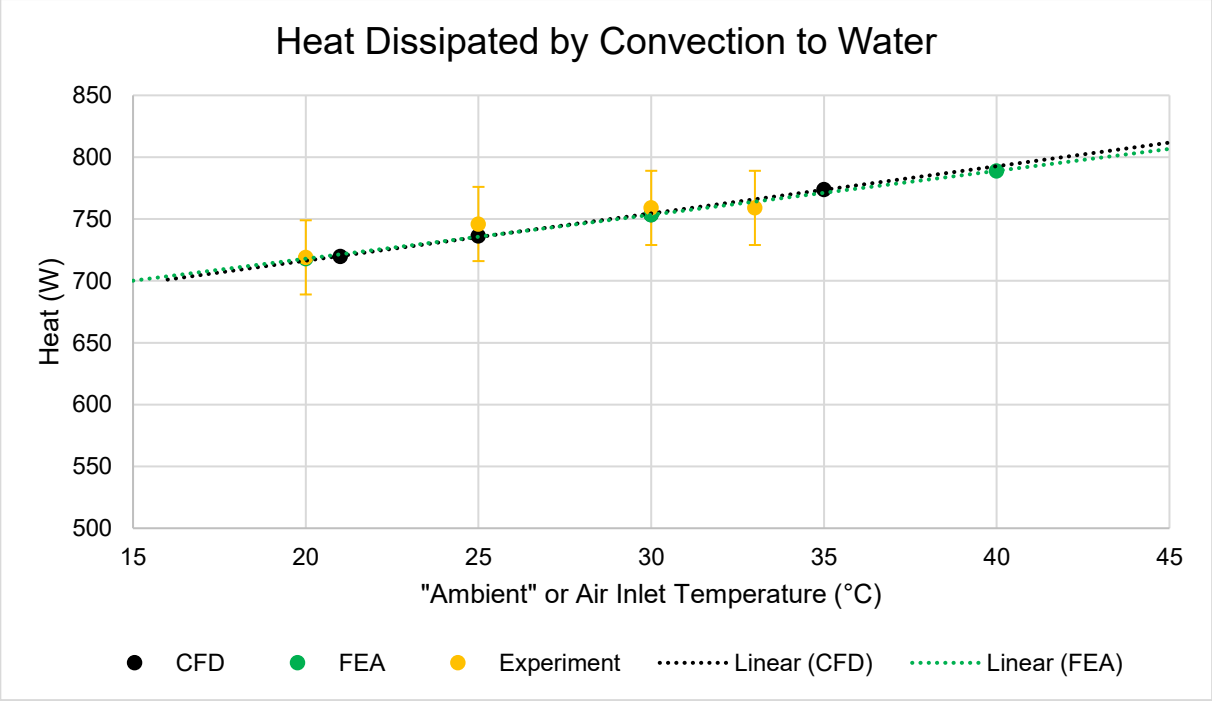

Figure 15: Heat dissipation values to water at different air temp., SAS-only

Incoming air at 1.3 m/s

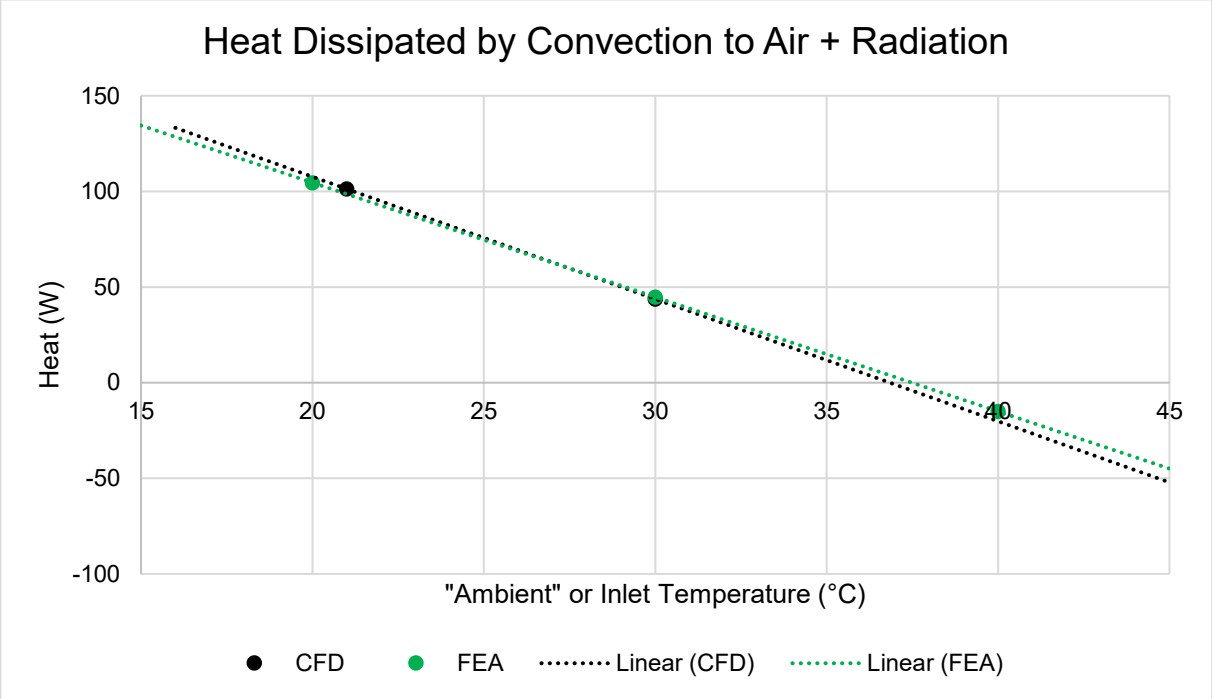

Figure 16: Heat dissipation values to air and by radiation at different air temp., SAS-only

Figure 14 to Figure 16 report the heat dissipation values after the correction of copper emissivity. The plots and the FEA values are from A. Moilanen. The experiment values are from V. Andavan and A. Vamvakas.

It can be seen that in Figure 14 and Figure 15, the CFD values correspond well with the experimental values after the adjustment of copper emissivity. The FEA curve and the CFD curve converged.

A higher air speed of 1.3 m/s was tested, with results shown in Figure 16. The FEA curve corresponds well with the CFD curve as well. For FEA, the adjusted air convective heat transfer coefficient was 11 W/(m^2·K). The water convective heat transfer coefficient remained to be ~ 4000 W/(m^2·K). Experiment values were not available at 1.3 m/s air.

3.7.5.6. Contour and vector plots

This section shows a few visualisation plots generated with CFD-Post before the adjustment in copper emissivity, i.e. the values for the case in Section 3.7.5.4 are shown. They were not re-generated with the new emissivity values because at this stage they are only for illustration purposes and without considering other parts of the module, the flow and temperature fields are not of great reference value. These plots were shown in the presentation for the CLIC Project Meeting #28 [3].

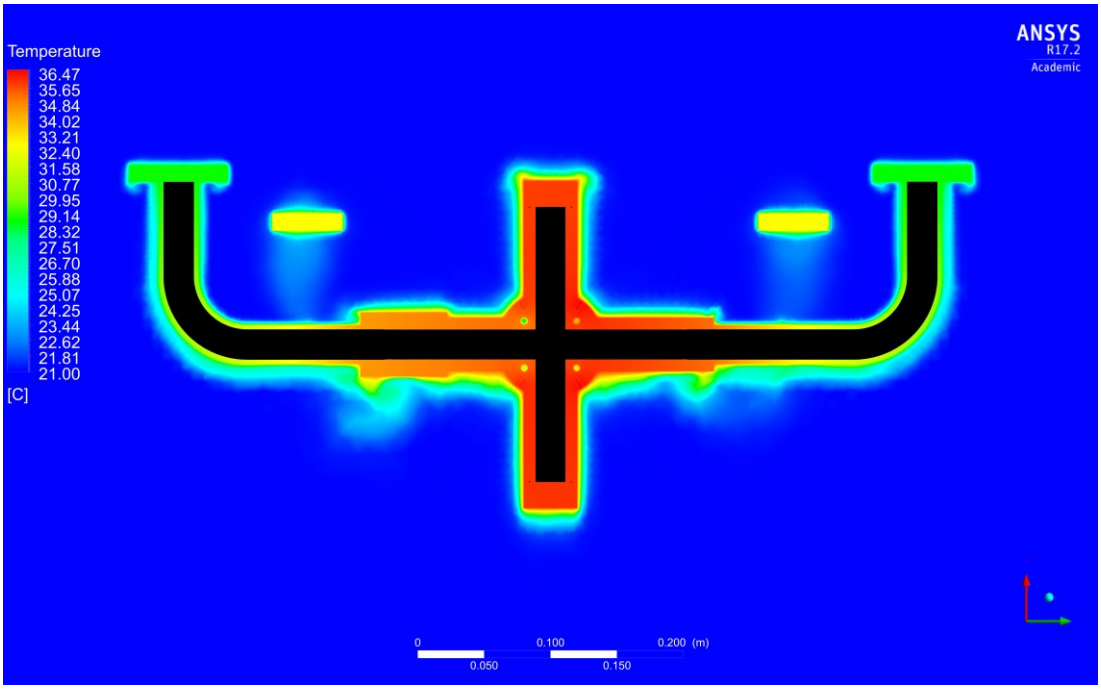

Figure 17: Temperature field at a cross section of the SAS, SAS-only

Figure 17 shows the temperature field at a cross section. The temperature of the SAS was at approximately 36 °C.

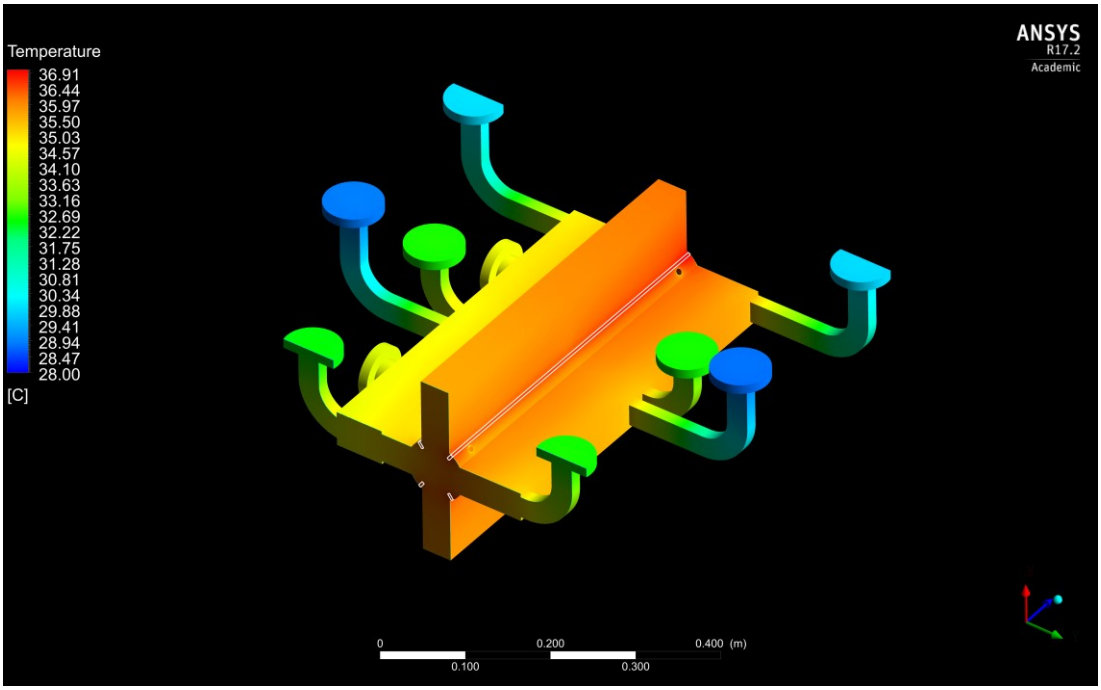

Figure 18: Temperature distribution at the surface of the SAS, SAS-only

Figure 18 shows the temperature distribution at the surface of the SAS. CFD analyses provide the valuable capability to visualise temperature distributions of the structure. Although this is as well possible in the finite-element model, there are large uncertainties in the results because all of the fluid flows are modelled with one averaged heat transfer coefficient, which is definitely not the case in reality.

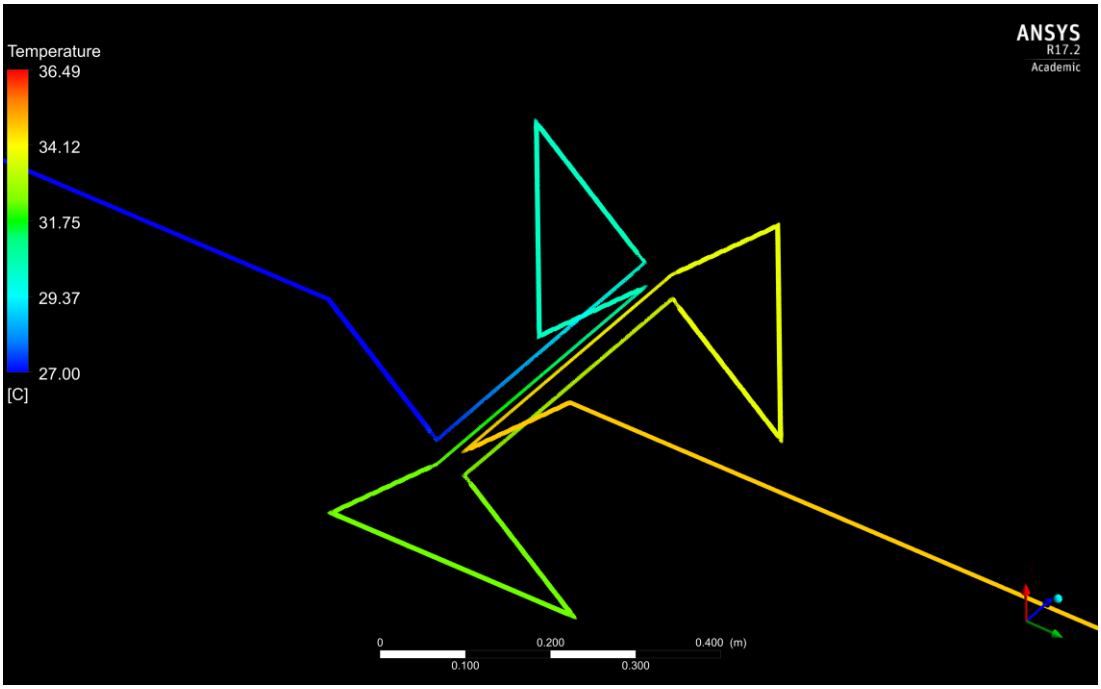

Figure 19: Temperature of water in the pipe, SAS-only

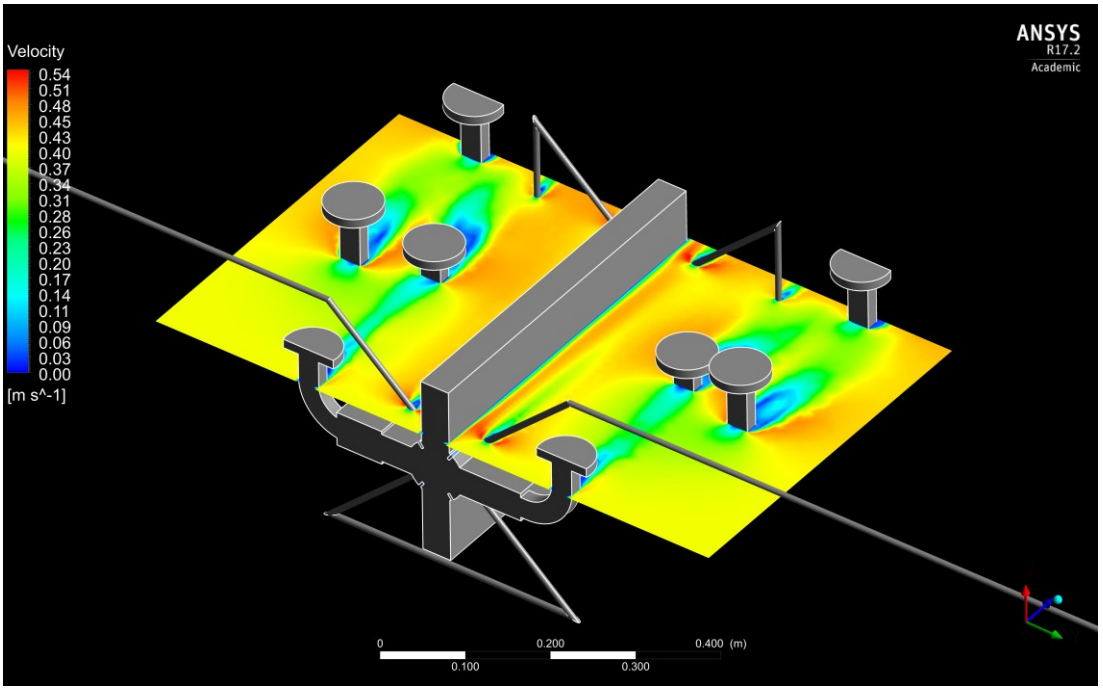

Figure 20: Velocity field of air at a cross section around the SAS, SAS-only

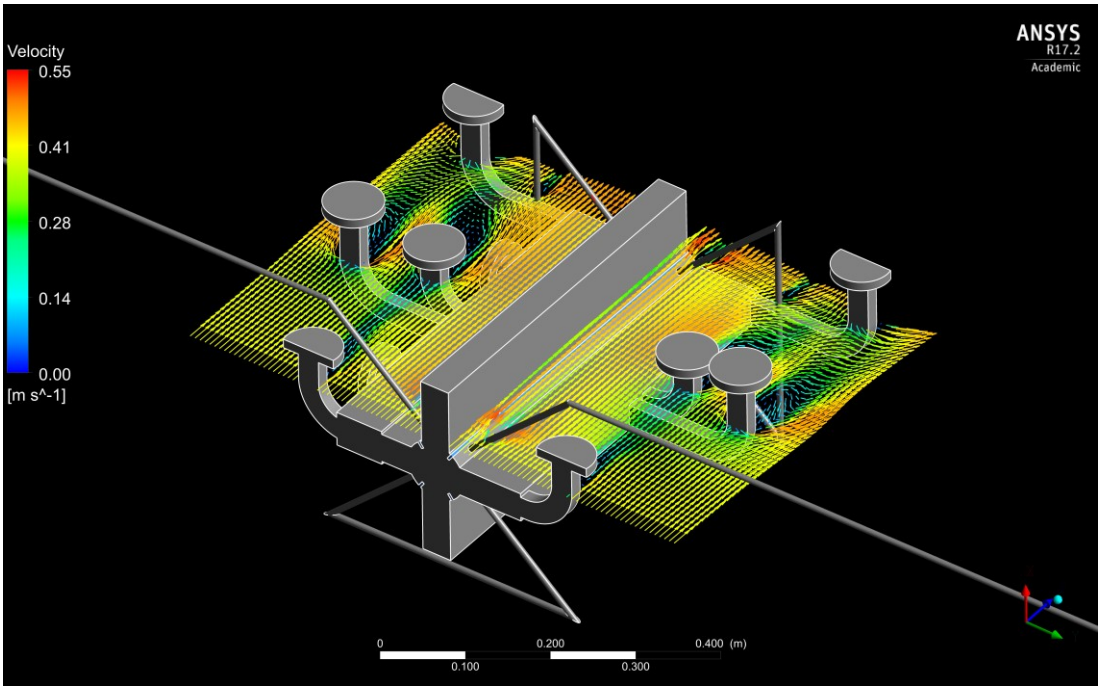

Figure 21: Velocity field of air as a vector plot at a cross section around the SAS, SAS-only

Figure 19 to Figure 21 give other visualisation examples possible with CFD analyses.

3.7.6. Comments

The study performed with one SAS acts as a proof-of-concept case for integrating CFD into the system of approaches (Figure 2). It integrates the advantages between experimental methods, analytical modelling, finite-element analyses and CFD, and provides good estimation for the coefficients used in the finite-element and analytical models.

However, this is only a very simplified case. The insights learnt from this were to be applied to the more comprehensive main-beam-tunnel-wall case in Section 3.9.

3.7.7. Failed cases

This section is dedicated to some of the failed cases that are worth a mention during the testing of different approaches for the SAS-only case. Almost all failed cases arose due to artificial simplification of cases, which might be either unrealistic or rejected by the code. In other words, they could be avoided if the full case was considered without any artificial simplification, but that would, however, introduce other issues such as convergence and meshing due to much higher complexity.

3.7.7.1. Virtual thickness of a surface as a heat source

It is an available feature in Fluent that the user can specify a thin layer of material on a surface (Section 6.3.14.3.7, Thin-Wall Thermal Resistance Parameters in [8]). It allows the specification of the material, the thickness, and the heat generation rate (power per unit volume) of the layer. Fluent then solves the one-dimensional steady heat conduction equation for the heat transfer [8].

The idea of specifying a heat generation at a surface stemmed from the finite-element simulations performed by A. Moilanen. In his simulation case, only the solid was solved and the fluid flows were modelled with a constant heat transfer coefficient. ANSYS Mechanical might have allowed to specify a heat generation on a surface under such conditions. A heat generation was specified in the finite-element case on the curved surfaces at the centre of the SAS, where the heating elements were located.

In reality, specifying a heat generation value at a surface is non-physical since heat has to be generated from a volume. Fluent does not allow the specification of heat generation at a surface, except using the aforementioned thin-wall approach as a workaround. A test case with this feature enabled, with wall thickness 1 mm, on the same surfaces was set up but the solution immediately failed. It might be due to the complexity of the geometry. This was not then pursued since meshing the heating elements corresponds to the experiment, whereas heat generation on these surfaces was an approximation in the first place for convenience in the finite-element simulations in ANSYS Mechanical with the existing geometry files.

3.7.7.2. Pipe inlets and outlets inside the domain

Since the pipes were artificial, it was first attempted to just construct the pipes such that the water inlet and outlet were right next to the SAS body, for two reasons, 1) lower complexity since less water flow had to be computed; and 2) fewer artificial effects on the air flow since the artificial pipes did not have the same geometry as the real pipes. It was shortly discovered that Fluent does not allow inlets and outlets within the computational domain, but only at the domain boundaries. As a compromise the pipes were extended to the side boundaries of the domain.

3.7.7.3. Abrupt change in geometry close to the air inlet boundary

The original simplified geometry provided by A. Vamvakas included one SAS with the flanges connecting with the compact loads. It was then deemed necessary to cut the two sides in the axial direction to consider only one SAS, since there were overlapping regions between consecutive SAS's. At first it was cut to the beginning of the protruding feature, which was already existing in the simplified geometry, as shown in Figure 22. This cut had two problems.

The first problem was that cutting until this point had no physical meaning, in the sense that in reality there was a spring connecting two SAS's and this protruding feature was in fact a hollow cavity for the beam rather than a solid obstruction against the air flow.

The second problem was that such a small protruding feature introduced an abrupt change in geometry close to the air inlet boundary. This in turn introduced abrupt changes in the velocity (see Figure 23), and thus required a much finer mesh for accurate results. Also, since in this case the velocity at the boundary was prescribed as a constant speed at the direction normal to the boundary, the resulting flow field would not be realistic due to the close proximity of an obstruction to the boundary. The flow had to change direction at some point before the obstruction, and this direction change required a certain distance, which might be beyond the distance between the SAS main body and the boundary.

Although the first problem already pointed out that the geometry should not have been cut to this point, the second problem provided some insights into the issues of having obstructions close to the boundary. It should be taken note in future cases when setting up boundary conditions and simplifying geometries.

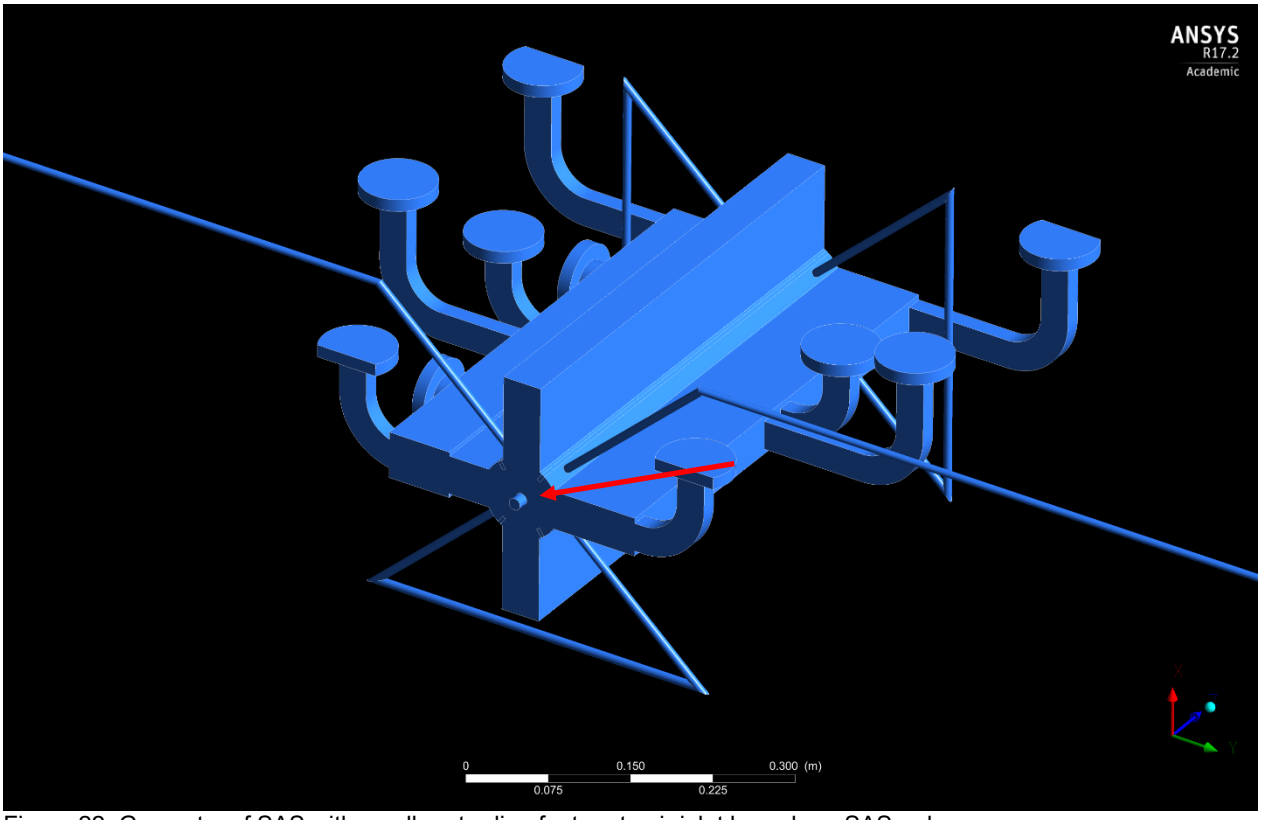

Figure 22: Geometry of SAS with small protruding feature to air inlet boundary, SAS-only

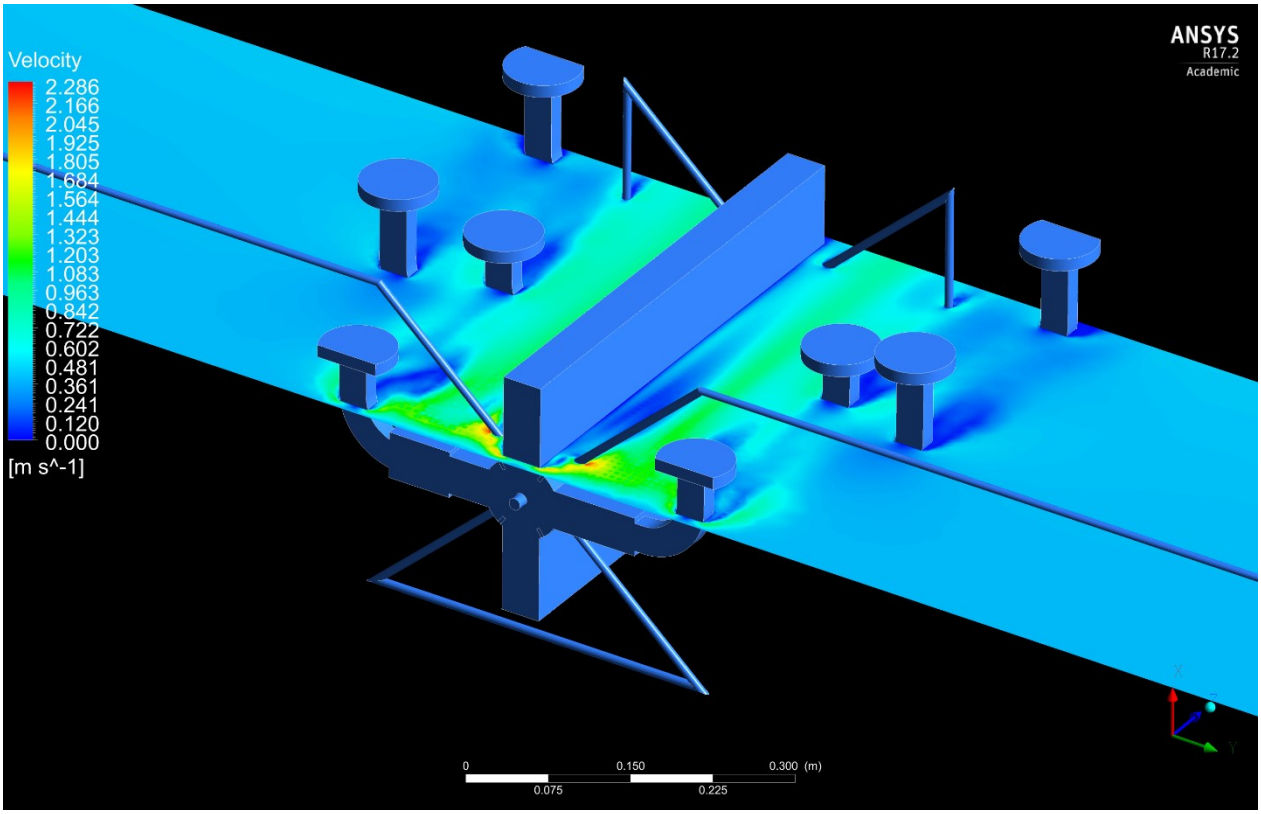

Figure 23: Velocity field with small protruding feature to air inlet boundary, SAS-only

3.8. Modelling of heat transfer to soil

3.8.1. Importance

It is important to understand or be able to estimate the amount of heat flow into the soil through the tunnel wall, so to identify an optimal and equilibrium operating temperature of the collider. This can be in the range of ~ 100 W per meter of tunnel, as shown in the preliminary analyses in the following sections.

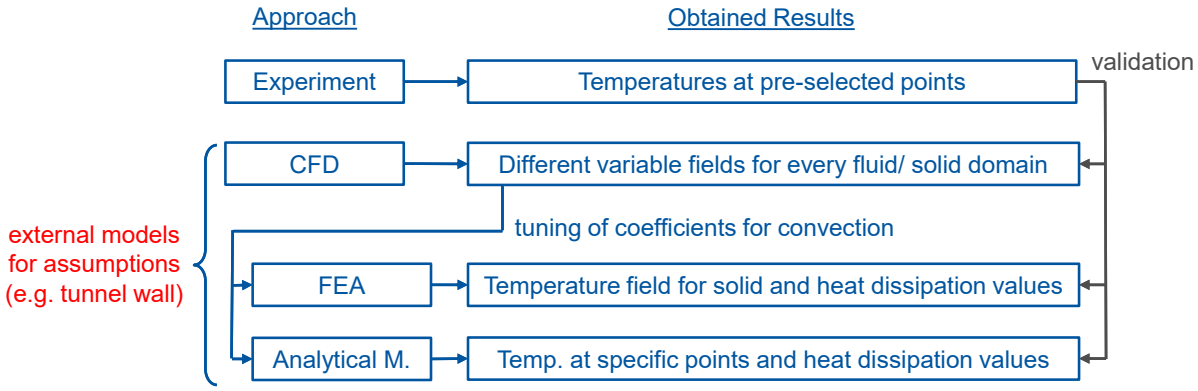

Figure 24: Role of external models in the entire approach

Figure 24 shows the role of external models in the approach chart.

3.8.2. Previous approach and its validity

3.8.2.1. Steady-state heat-resistance model

The previous, existing approach was a simple one-dimensional steady-state series-heat-resistance model in cylindrical coordinates [10]. It had three resistance components, namely, 1) convection heat transfer resistance between freestream air temperature within the tunnel and the tunnel wall; 2) conduction heat transfer resistance within the concrete wall layer; and 3) conduction heat transfer resistance in the soil region. The heat transfer equation given in [10] is as follows, where the terms are self-explanatory:

$$Q_{AIR-GROUND} = \frac{T_{AIR} - T_{GROUND}}{\frac{1}{2\pi D_{TUNNEL} h L} + \frac{\ln\left(\frac{D_{TUNNEL} + 2t_{CONCRETE}}{D_{TUNNEL}}\right)}{2\pi k_{CONCRETE} L} + \frac{\ln\left(\frac{2r_{GROUND}}{D_{TUNNEL} + 2t_{CONCRETE}}\right)}{2\pi k_{GROUND} L}}$$

3.8.2.2. Incorrect assumptions

This approach is unfortunately invalid for two reasons: 1) assuming the existence of a steady state in terms of temperature distribution (and thus heat transfer) in the soil; and 2) assuming the existence of an undisturbed soil temperature at a distance (r_{GROUND}) sufficiently far from the heat source, i.e. the air in the tunnel.

The model can be invalidated with a simple thought experiment. Imagine that there is a point heat source lying in an infinitely large body of soil. The heat source is always maintained at a certain temperature T_H. Initially, the entire soil body is at a temperature T_L, where $T_L < T_H$. The second law of thermodynamics dictates that heat must flow from the heat source to the soil, and heat slowly propagates radially outwards. One can then easily observe that 1) there is no steady state for this problem as heat always propagates outwards; and 2) "undisturbed" soil will be disturbed after some sufficient amount of time.

Putting in other words, one must be clear that there is no active cooling in the soil to maintain the soil temperature at a certain distance from the tunnel (r_{GROUND} in the equation above) to be exactly that set temperature (T_{GROUND} in the equation above) indefinitely. A heat source of constant temperature, e.g. T_{AIR} in the equation above, would *continuously* heat up the soil further and further away from it. A steady-state condition does not exist, and the temperature profile obtained from the heat-resistance model in [10] is only a profile *at one particular point in time* when the heat has just propagated to the distance r_{GROUND}. The solution temperature profile, thus the heat dissipated to soil, directly depends on the choice of T_{GROUND} and r_{GROUND} in the steady-state model, of which an appropriate method of estimation or modelling has not been, and can hardly be, provided.

Assuming a temperature T_{GROUND} for heat transfer analysis through the wall is only a 'first approximation' [11, p. 425]. In the case of having a strong heat source (i.e. the tunnel), such an approximation is inadequate.

Although the approach is ultimately incorrect, before the realisation of an appropriate model, an ANSYS case was set up along with an analytical solution for a steady-state model, before a similar model was found in [10]. It is provided in Section 6.2.

3.8.3. Inspiration from temperature profiles underground

Despite the argument given, it is intuitive for the concept that there is an “undisturbed” temperature at a certain distance from a heat source. It is particularly apparent when one measures the temperature profile at different depths from the ground with a probe – it would most likely be a decaying pattern which approaches an “undisturbed” temperature asymptotically.

This is indeed true, as revealed in [12]. What is overlooked, however, is that this decaying temperature profile is transient, and, periodic. In simple words, it is periodic that, in summer times, the ground temperature is hotter than this “undisturbed” temperature, whereas in winter times, the ground temperature is cooler than this “undisturbed” temperature. In this sense, the so-called “undisturbed” temperature is in fact approximately the average of the ground temperature over the year, see Figure 25.

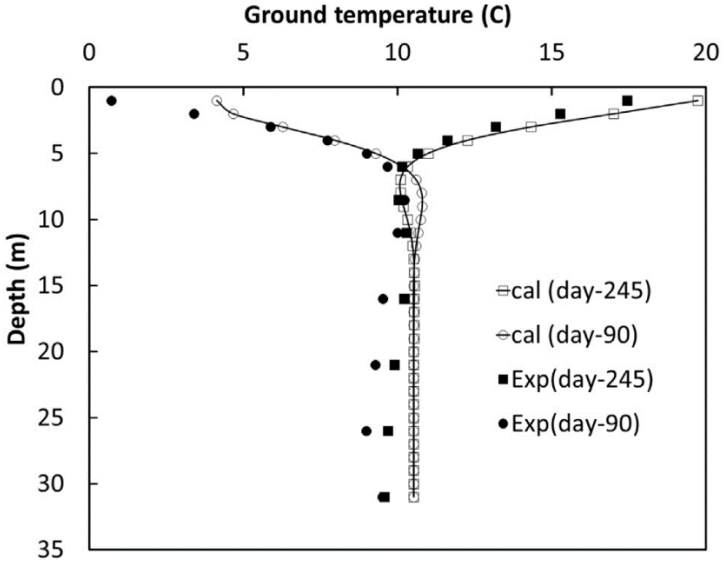

Figure 25: Variation of underground temperature profile in 155 days [12]

Givoni et al. stated the following:

> The “natural”, unmodified temperature of the ground is governed by two boundary conditions: the cyclic annual pattern of the surface temperature and the constant temperature at a depth of several meters. Over large homogeneous areas, the “depth” temperature equals the long-term annual average of the surface temperature [13, p. 16].

It follows that in the underground tunnel case, the “undisturbed temperature” at some distance from the tunnel wall is approximately the time-average of the temperature of the tunnel wall, neglecting the effect from the ground surface. The question then becomes for what periods the collider is supposed to operate when it is placed underground. This, however, was not known at the time of writing. Nevertheless, an analytical model was developed (Section 3.8.5). An ANSYS Mechanical Transient Thermal case was set up (Section 3.8.6) and a Mathematica code was written (Section 3.8.7).

3.8.4. Thermal properties of concrete and soil

Some efforts were made to determine the likely thermal properties of the concrete and soil in the region. For transient analyses, the thermal diffusivity, denoted by α, is particularly important:

$$\alpha = \frac{k}{\rho c_p}$$

where k is the thermal conductivity, ρ is the density, and c_p is the specific heat capacity.

For concrete, the thermal properties were directly taken from [10]:

Density, ρ = 2400 kg/m^3

Thermal conductivity, k = 2.5 W/(m·K)

Specific heat capacity, c_p = 1000 J/(kg·K)

For soil, thermal properties were difficult to estimate since they are significantly affected by the soil composition, moisture content and temperature [14], [15]. For silt loam, for example, an increase in soil moisture content from 5 wt.% to 35 wt.% can increase the thermal conductivity by 4 times [14]. At this stage, however, an exact value is not necessary. What is of interest is the approximate magnitude of the heat absorbed by soil.

It is known that most of CLIC would be in molasse (M. J. Stuart, personal communication, November 28, 2017). Three borehole records (5140, 5489, 10601) were provided by M. J. Stuart, which are included in Section 6.5. But since the records only provided data for water content and density, external literature had to be searched for thermal properties. Such data, unfortunately, was not readily available. A compromise was made and the thermal properties for molasse were obtained from p. 49 in [16], for *granitische Molasse* (granitic molasse). It was chosen because it was the same type of soil (Molasse basin) and the density was similar to that from the boreholes (~ 2600 kg/m^3). The properties obtained are as follows:

Density, ρ = 2600 kg/m^3

Thermal conductivity, k = 3 W/(m·K)

Specific heat capacity, c_p = 1120 J/(kg·K)

One can easily observe that the thermal properties of soil are similar to that of concrete, in this particular case. They can be combined and solved with relative ease since no coupling is involved, as shown in Section 3.8.7.

3.8.5. Analytical model

Refer to Figure 26.

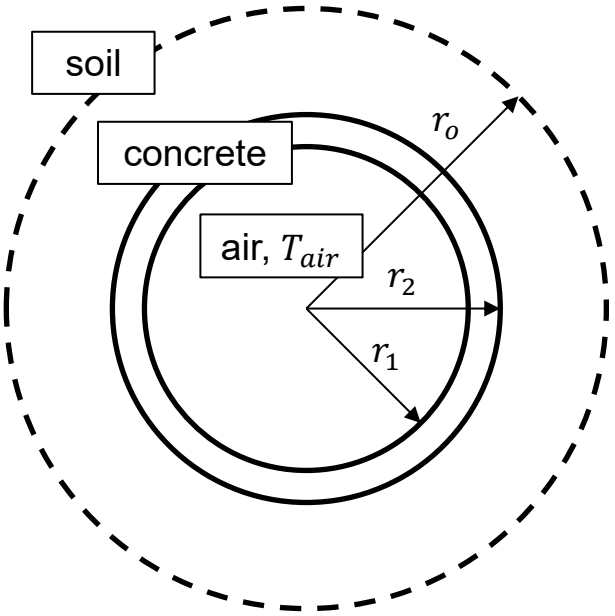

Figure 26: Cross-section of the tunnel for the transient approach

The heat transfer model is easily constructed from the one-dimensional transient heat equation in cylindrical coordinates:

$$\frac{1}{r}\frac{\partial}{\partial r}\left(r\frac{\partial T_i}{\partial r}\right) - \frac{1}{\alpha_i}\frac{\partial T_i}{\partial t} = 0 \qquad i \in \{c, s\} \qquad r_1 < r < \infty \qquad t > 0$$

There is one equation for each layer, namely, concrete (denoted with subscript c) and soil (denoted with subscript s). r extends to infinity as the soil layer is assumed to be semi-infinite.

Initially, the temperature across the entire domain is T_{ini}:

At $(r = r, t = 0)$

$$T_c = T_s = T_{ini}$$

The initial temperature is taken as the typical undisturbed ground temperature at the intended depth of the tunnel, which is 16.2 °C (A. M. Rodriguez, personal communication, November 17, 2017). This is then set as the initial temperature, $T_{ini} = 16.2$ ℃.

[17] provides an example for estimating the temperatures around the tunnel along the tunnel loop length of the Future Circular Collider at CERN.

For the concrete layer, the following boundary condition is specified:

At $(r = r_1, t > 0)$,

$$-k_c \frac{\partial T_c}{\partial r}\bigg|_{r=r_1} = h\big(T_{AIR} - T_c(r = r_1, t)\big)$$

where k_c is the thermal conductivity of concrete. Radiation exchange between the wall and the module is not considered, since the effect is insignificant. See Section 3.7.5.5.

For the interface between concrete and soil regions, the following boundary conditions are imposed:

At $(r = r_2, t > 0)$

$$T_c(r = r_2, t) = T_s(r = r_2, t)$$

$$-k_c \frac{\partial T_c}{\partial r}\bigg|_{r=r_2} = -k_s \frac{\partial T_s}{\partial r}\bigg|_{r=r_2}$$

As t increases from 0, heat will propagate in the positive r direction. The domain for r extends to infinity. The above forms a set of coupled partial differential equations.

However, an outer boundary ($r = r_o$), and an end of the time domain ($t = t_{END}$) are necessary to define the domain for a numerical solution. No boundary condition can be set at this boundary $r = r_o$, however, since $T_s(r_o, t)$ is not defined. Therefore, to circumvent the problem, the end of the time domain t_{END} is limited to the point when the temperature near the boundary $r = r_o$ has not been disturbed from its initial temperature, i.e. the heat has not propagated to this boundary. Mathematically, it can be stated as:

$$\left|\lim_{r \to r_o} T_s(r, t_{END}) - T_{ini}\right| < \varepsilon$$

and ε is sufficiently small. The problem of artificial boundary and temperature in the steady-state approach is circumvented.

It was unfortunate, however, that attempts to solve the coupled partial differential equations in Mathematica failed. This might be due to incorrect setting for the solution resolution. Interested readers may work on the unfinished code. The coupling, thus, was only investigated with finite-element methods in ANSYS.

3.8.6. Solution from ANSYS

Since the coupled partial differential equations could not be solved in Mathematica (or required considerable extra effort to do so), the problem was put to ANSYS Mechanical for solution.

3.8.6.1. Convective heat transfer coefficient

The convective heat transfer coefficient between tunnel air and tunnel wall was determined using the Gnielinski correlation [18], which is suitable for turbulent flow in pipes.

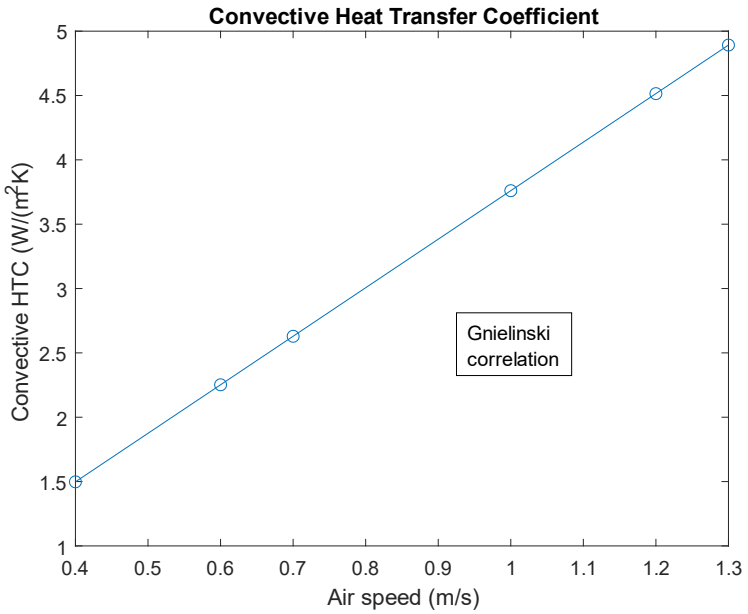

Figure 27: Gnielinski correlation

Figure 27 shows the plot of convective heat transfer coefficient against air speed using the Gnielinski correlation. From [18], the Gnielinski correlation is as follows:

$$\mathrm{Nu} = \frac{(f/8)(\mathrm{Re} - 1000)\mathrm{Pr}}{1 + 12.7\sqrt{f/8}\,(\mathrm{Pr}^{2/3} - 1)}$$

where f is the friction factor.

The air properties at 300 K were used, the following values obtained from [19]:

Prandtl number, Pr = 0.707

Density, ρ = 1.177 kg/m^3

Dynamic viscosity, μ = 18.46E-6 kg/(m·s)

Thermal conductivity, k = 26.24E-3 W/(m·K)

The inner diameter of the tunnel was chosen to be 5.6 m (tunnel cross section, Figure 80), and assuming a roughness of 10 mm, the relative roughness is 10/5600 = 0.002. The friction factor from the Moody chart is 0.022.

3.8.6.2. Results

To obtain a meaningful result, an operating *cycle* had to be input into the model for transient behaviour. The heat source was assumed to be switching between an on- and off-state. An on-state referred to a tunnel air temperature of 32 °C and an off-state referred to a tunnel air temperature of 25 °C. There were 3 days of off-state per month, and 3 months of off-state per year. The initial temperature was set at 16.2 °C. The model was solved for 37 months, and results are reported excluding the first month.

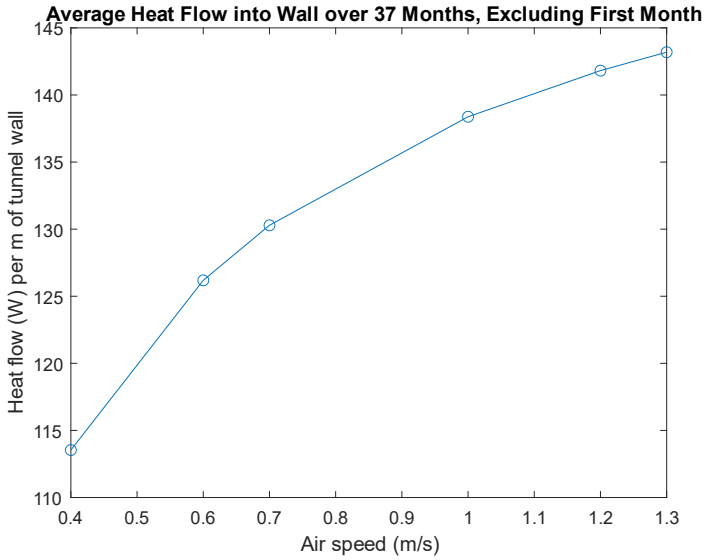

Figure 28: Average heat flow into wall at different air speeds

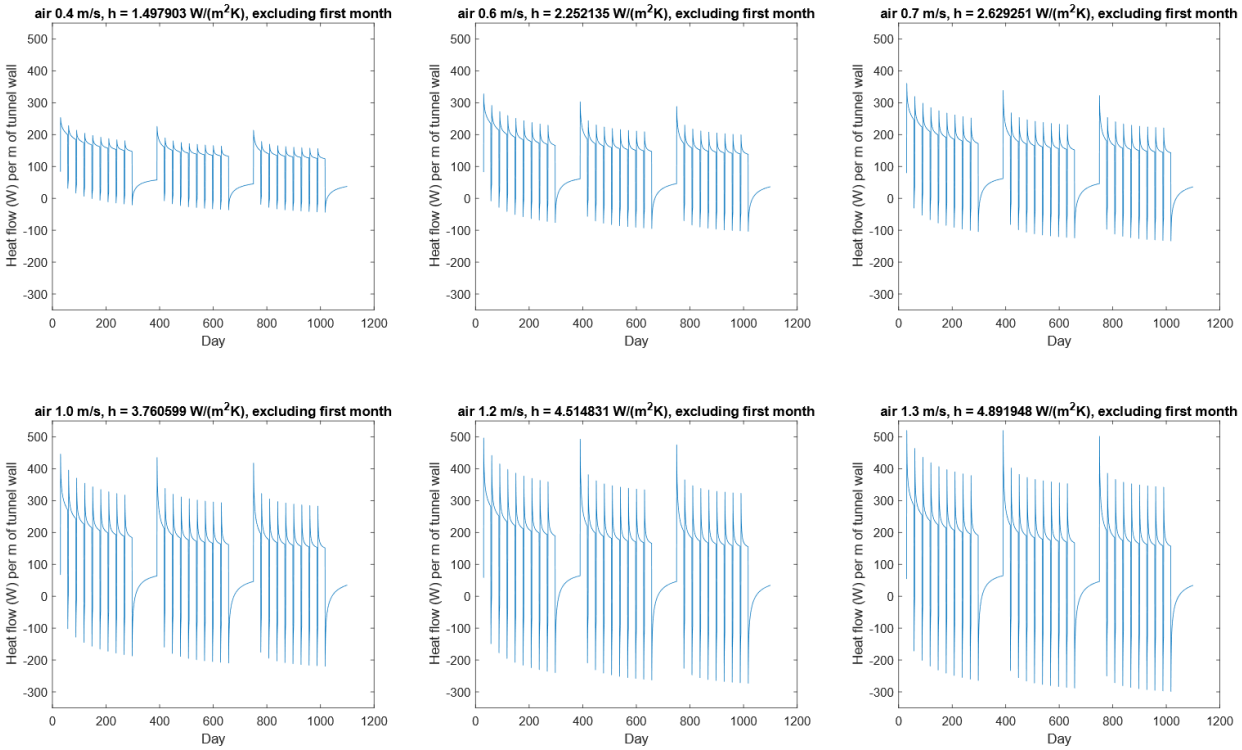

Figure 29: Heat flow variation over time at different air speeds

Figure 28 illustrates the average heat flow at different air speeds. The averages were obtained from the variation of heat flow over time, as given in the six plots in Figure 29. With this approach, the average heat flow into the tunnel wall over a given time period can be computed. This average can be input to the steady-state *CFD* analysis of the collider. This serves as an important point in the entire workflow. As long as the operating cycle can be estimated or known, an appropriate number of heat flow into the tunnel wall can be input to the CFD analysis.

3.8.7. Solution from Mathematica

Although the coupled equations could not be solved with Mathematica, a simpler approach was carried out. Since the thermal properties of concrete and soil are similar (Section 3.8.4), they can be merged into a single material and it greatly simplifies the solution procedure. This has the advantage of much improved speed and convenience of computation, especially when a parameter study is to be carried out.

No coupling of partial differential equations is necessary when only one material is considered. The set in Section 3.8.5 is thus simplified to as follows:

Governing equation:

$$\frac{1}{r}\frac{\partial}{\partial r}\left(r\frac{\partial T}{\partial r}\right)-\frac{1}{\alpha}\frac{\partial T}{\partial t}=0$$

Initial condition, at $(r=r, t=0)$:

$$T=T_{ini}$$

Boundary condition, at $(r=r_1, t>0)$:

$$-k\left.\frac{\partial T}{\partial r}\right|_{r=r_1}=h\left(T_{AIR}-T(r=r_1,t)\right)$$

For the merged thermal properties, the thermal conductivity of the merged material is taken to be equal to the thermal conductivity of concrete. This was decided to ensure that the temperature gradient at the wall-air interface was unchanged. The average thermal diffusivity was taken for the thermal diffusivity of the merged material.

Thermal conductivity, k = 2.5 W/(m·K)

Thermal diffusivity, α = 1.036E-6 m^2/s

A similar problem can be found in [20, p. 263] where a complex analytical solution is as well provided.

A Mathematica code was written which could search the appropriate domain size (r_o), as described in Section 3.8.5. The current code, however, was not capable of incorporating an operating cycle. The air temperature was set to always be 32 °C and flowing at 0.4 m/s. The initial temperature was set to be 16.2 °C.

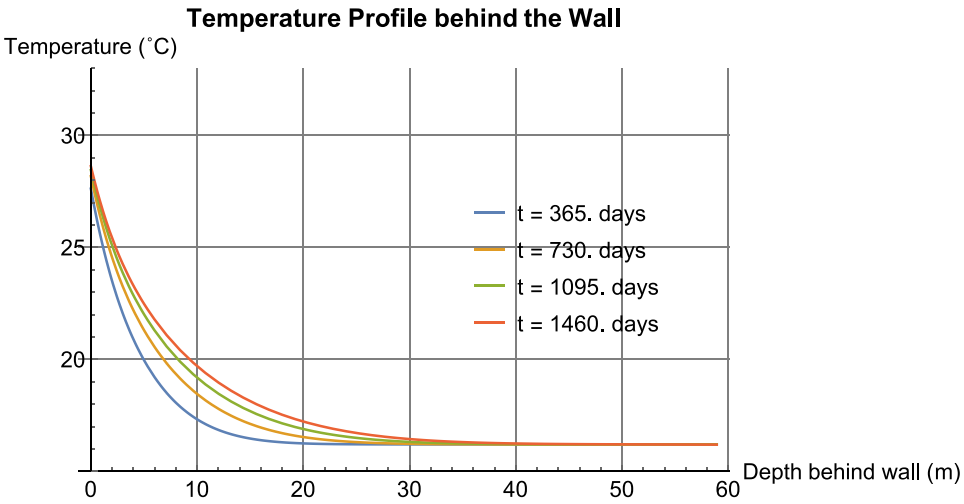

Figure 30: Temperature profile behind the tunnel wall

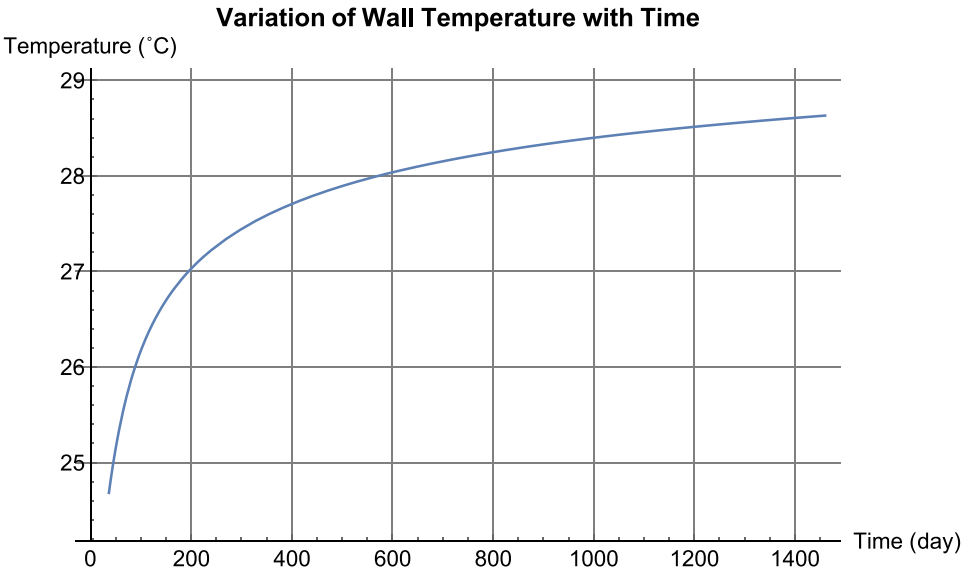

Figure 31: Variation of wall temperature with time

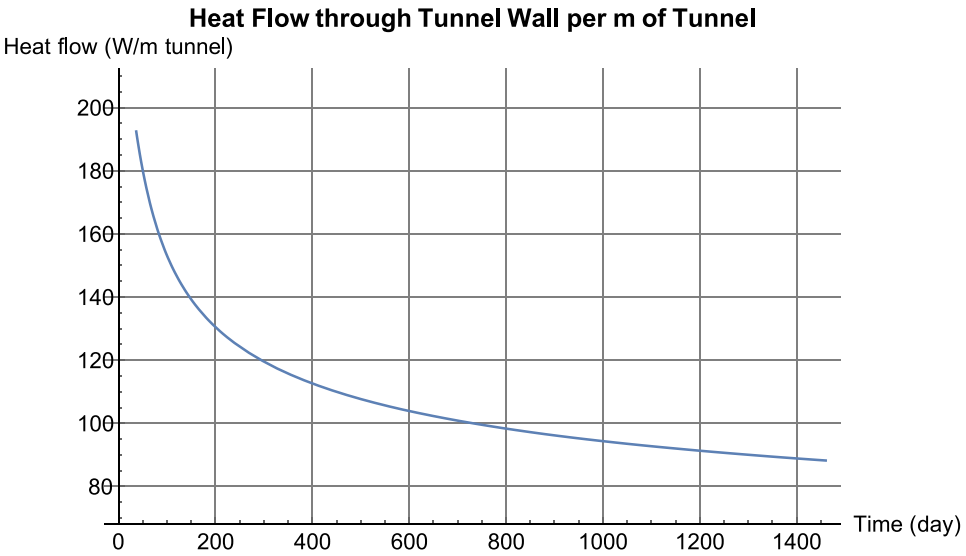

Figure 32: Heat flow through tunnel wall per metre of tunnel

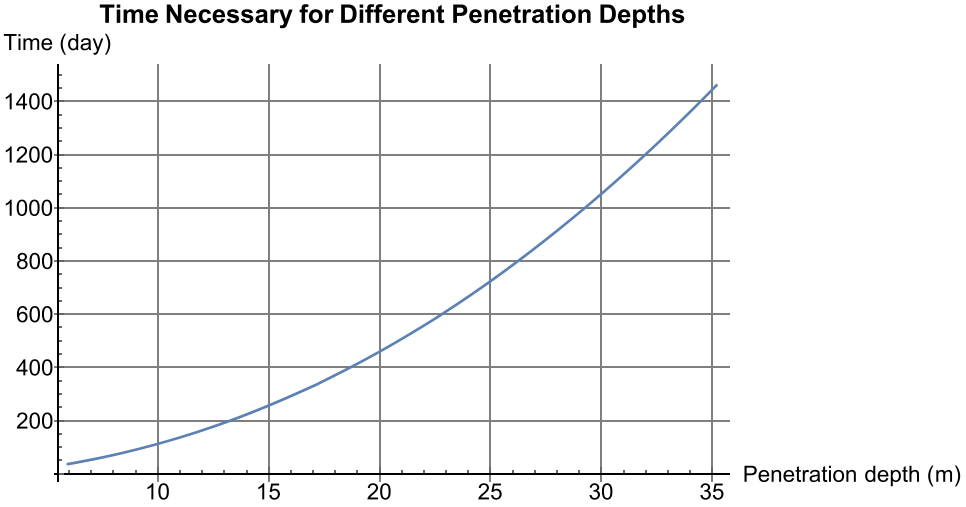

Figure 33: Time necessary for different penetration depths

Figure 30 shows the change of the temperature profile behind the wall at different times. Figure 31 shows the variation of wall temperature, $T(r = r_1, t)$ with time. Figure 32 shows the variation of heat flow per metre of tunnel into the tunnel wall with time. Figure 33 shows the time necessary for different *penetration depths*. Here, *penetration depth* is defined such that at a specific time, the temperature at the penetration depth increases by 0.1 °C. In other words, the penetration depth is in effect the location where the “undisturbed” soil region starts. This location moves with time, and therefore the steady-state approach is invalid (by assuming a constant r_{GROUND}).

It is obvious that a merged material gives a much higher flexibility in obtaining different kinds of results with ease.

3.9. Main-beam-tunnel-wall case

3.9.1. Heat through tunnel wall

Section 3.8 has presented an adequate model for the heat transfer through the tunnel wall to the soil. Unfortunately, since the operation cycle was not known, a proper value for heat dissipated through the tunnel could not be estimated. This section presents a CFD model incorporating the tunnel wall with the heat flux through the tunnel wall set to zero.

3.9.2. Problem definition

3.9.2.1. Including the tunnel

The current problem was a significant step up from the SAS-only case and had posed significant challenges in geometry simplification, meshing, and solution. Figure 34 shows the geometry of the current case. It includes the main beam part of the module, as well as the tunnel wall. The tunnel cross section follows the diagram (Figure 80) provided from the civil engineering team (M. J. Stuart, personal communication, January 8, 2018). The drive beam part was estimated with a box and nothing was solved in the drive beam region. The supports of the girder were measured according to the dimensions of the prototype. The pipes were extended to the tunnel boundaries, since the exact configuration of pipes outside the vicinity of the module was not known. It took months to completely fix and repair the geometry of the main beam for CFD, described in Section 3.2.1.

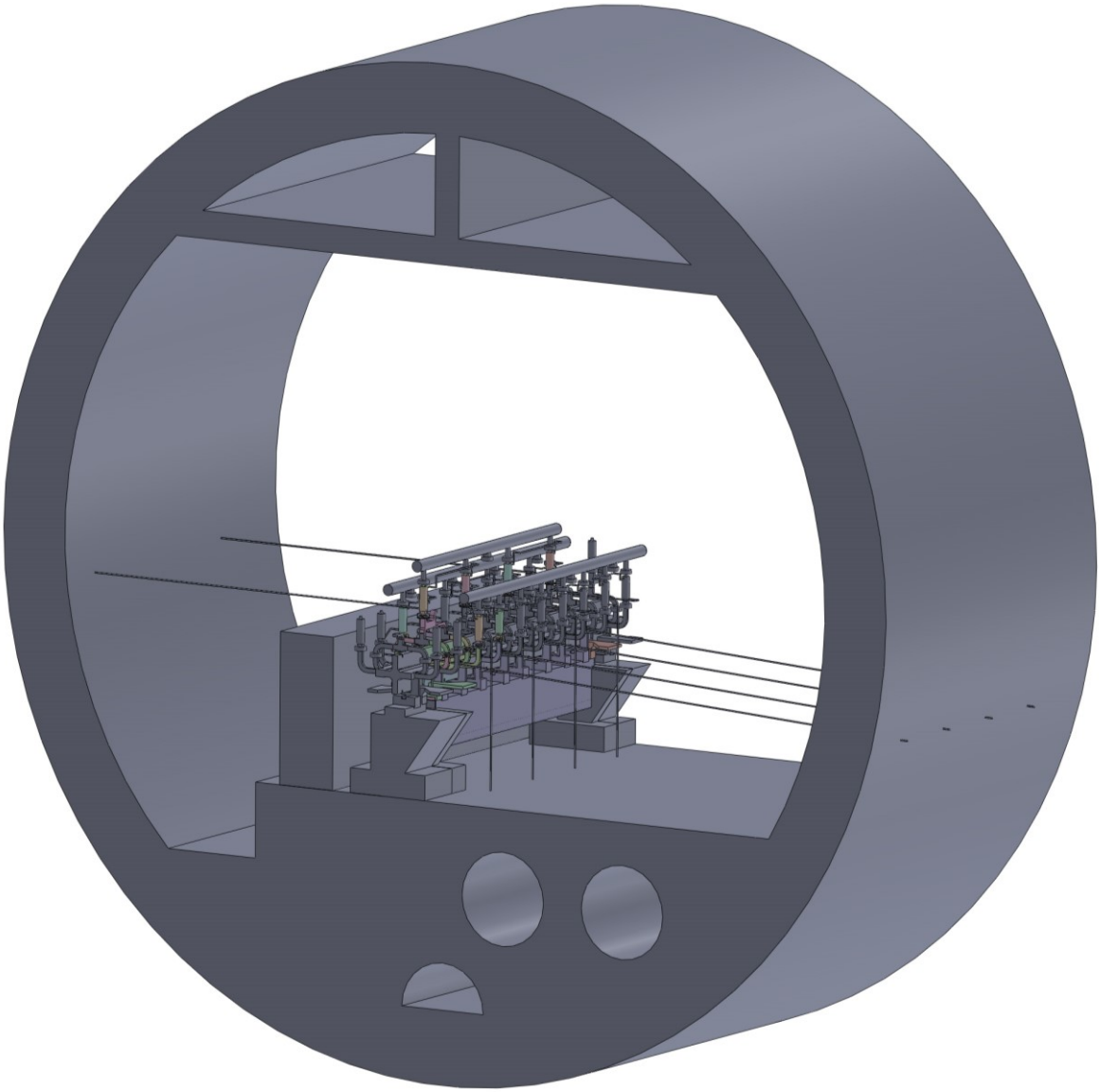

Figure 34: Computational domain, main-beam-tunnel-wall

3.9.2.2. Memory requirements

The requirement for computer memory was much higher than in the case with only one SAS (Section 3.7). Since the steps of meshing and loading the mesh in Fluent had to be done locally, the vast amount of RAM on the cluster could not be utilised. This placed significant constraints on the speed of meshing, because the workstation was set to use the much slower hard disk for extra memory space in the form of virtual memory. In one particular meshing attempt, the target element size filled up the physical memory (24 GB) very soon and took up at least 55 GB of virtual memory. The meshing took more than 72 hours before it was aborted. Therefore, it is highly recommended to have sufficient physical memory to load at least the majority of the mesh.

3.9.2.3. Approximations for hollow regions

A new material, i.e. *stagnant air*, was assigned to the hollow regions of the tunnel in Fluent. These hollow regions are indicated by red arrows in Figure 35. The empty regions in the girder were also stagnant air. For this material, all the properties of air were retained, except that air flow was not computed. This provided a compromise between model complexity and accuracy. It was later known that some of the hollow regions were to be filled with water instead of air. Their material could easily be individually changed to water, since each hollow region was specified as a separate part in the meshing step. Nevertheless, the current setting of *stagnant air* as the material was not expected to alter the results since the setting for wall heat flux was zero in this case.

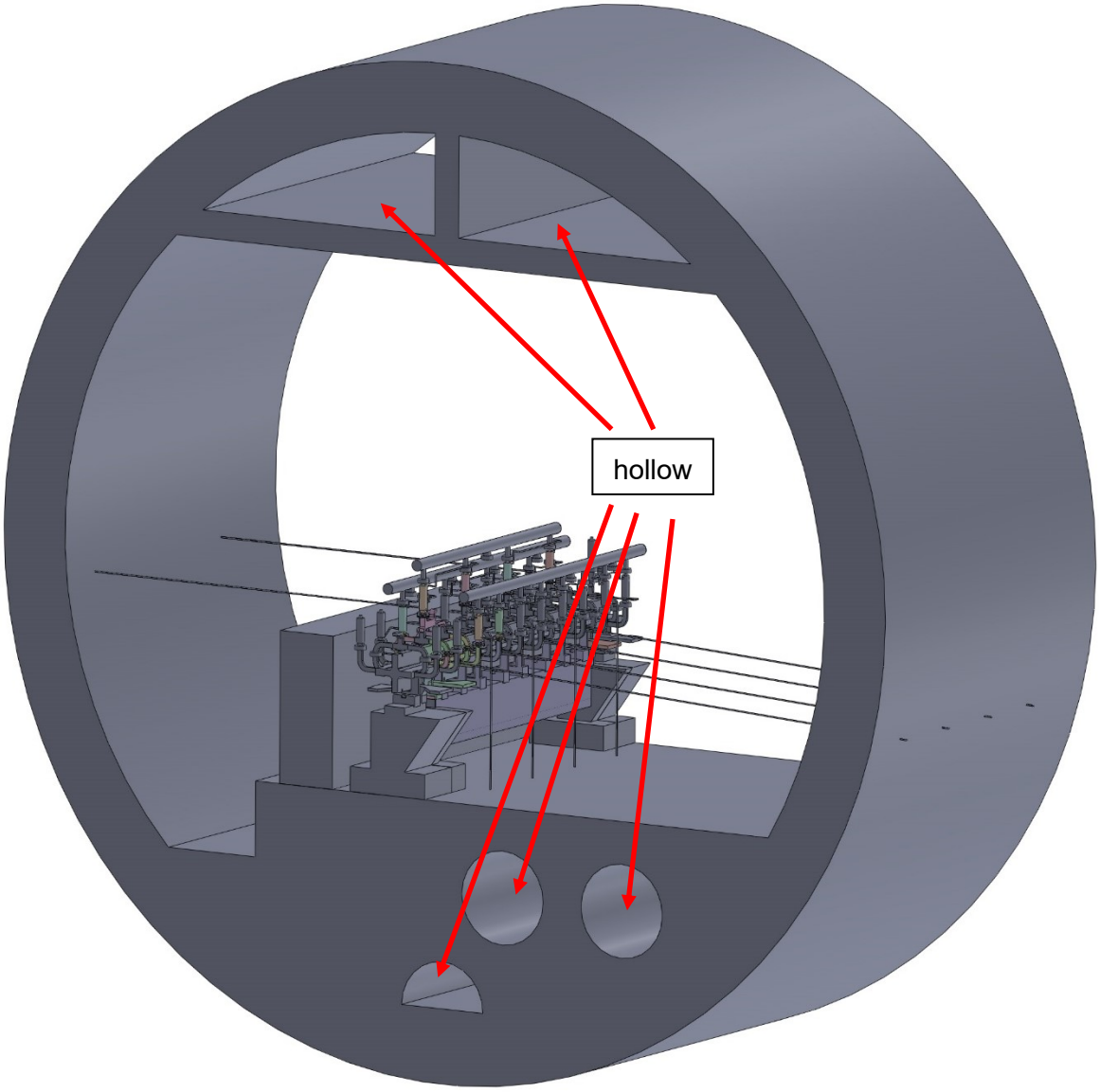

Figure 35: Hollow regions of the tunnel, main-beam-tunnel-wall

3.9.2.4. Dummy regions

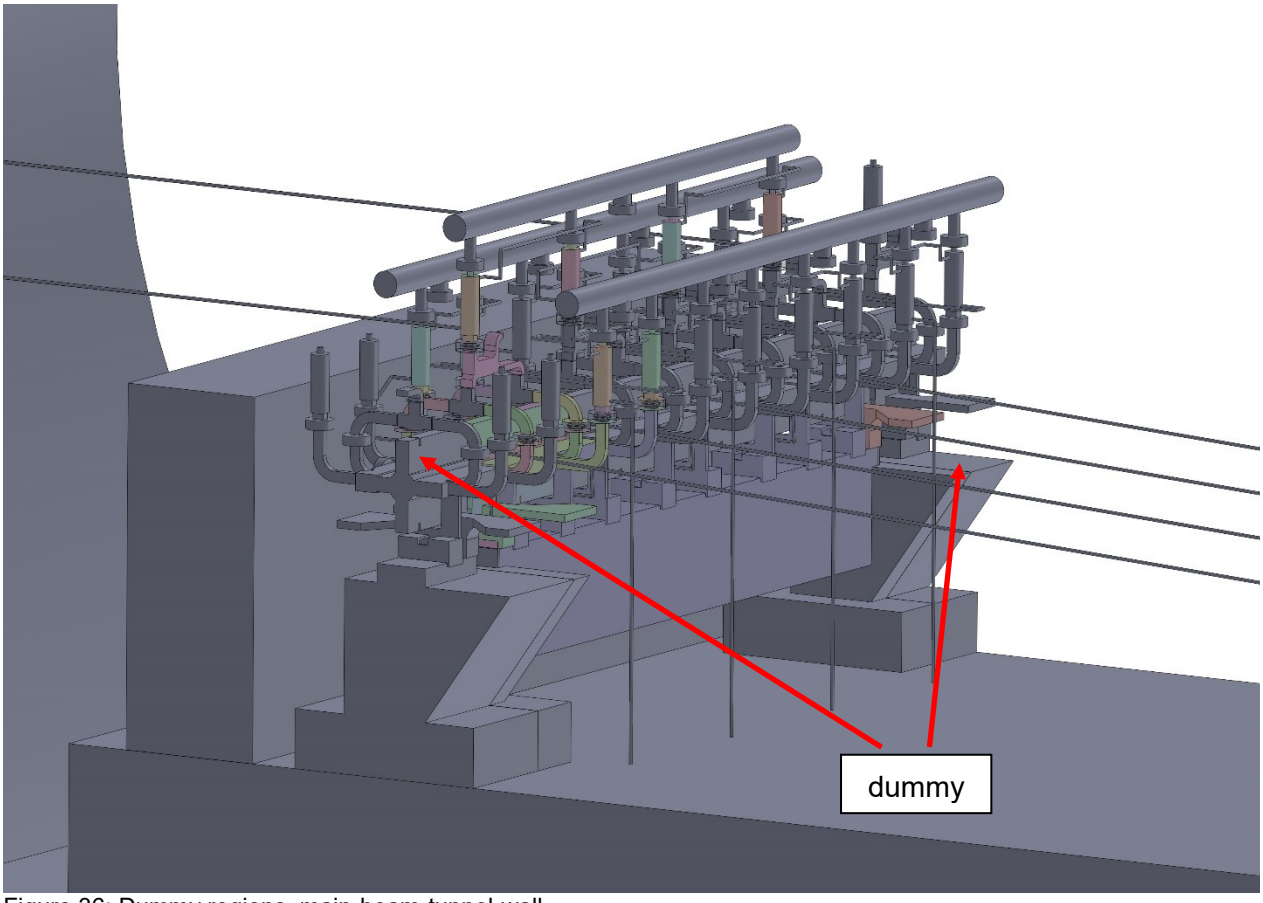

Figure 36: Dummy regions, main-beam-tunnel-wall

A dummy was added in front of and behind the module to introduce a slightly developed flow. Previous experience showed that, and not surprisingly, placing a strong obstruction near the main inlet requires an inlet boundary condition of higher certainty (see Section 3.7.7.3). Failure to do so may introduce convergence and accuracy problems. Removing such obstructions, and indeed placing a dummy solid in front of and behind the area of interest, introduces a smoother variation of flow speed. Nothing was solved within the dummy regions, and the boundary of these dummy regions coincided with the air inlet and outlet boundary. The choice of where to “cut” the module for these regions was made to ensure that the air inlet boundary was exactly the same as the air outlet boundary. This left space for introducing periodicity in the future, although it might require remeshing to achieve so.

3.9.2.5. Problem setup

Similarly, the heating elements in each SAS corresponded to those in the experiments. 780 W of heat was generated for each SAS, from the heating elements.

In the meshing process, surfaces which form the cylindrical cavity at the centre were specified as a separate group. This, in turn, enabled the possibility to assign heat flux values from these surfaces in Fluent, to mimic the effect of heat released from the beam, rather than what was set up in the experiments. To do this, simply assign a heat flux (W/m^2) for such surfaces and change the material of the heating elements to copper (so to “disable” the heating elements).

For the compact loads (CLs), 150 W was specified for each CL. There were 20 compact loads per module. The heating elements of the compact loads were made of aluminium and lied within the compact loads.

The SST k-ω model was used for turbulence, and the DO model was used for radiation. The entire simulation, again, was fully coupled in terms of heat transfer and fluid flow. The procedures for setting up the problem largely followed that described in Section 3.2.

3.9.2.6. Material properties

The number of materials in the domain increased dramatically compared to the SAS-only case. The following lists all of the materials:

1. Air
2. Aluminium
3. Concrete
4. Copper
5. Silicon carbide
6. Stagnant air
7. Steel
8. Water

The thermal properties of air were that from the Fluent default database. The incompressible gas law was used for density variations with temperature. Aluminium was found in the heating elements in the SAS and in the compact loads, and default values were retained. Concrete was specified for the tunnel wall. The properties were taken from [10]. For copper, which was found in the waveguides and the accelerating structure, and also the pipes, the default values were used. Silicon carbide was specified for the girder. The properties were obtained from BOOSTEC industries (A. Vamvakas, personal communication, October 27, 2017). Figure 85 provides a copy of the datasheet. Stagnant air, as described in Section 3.9.2.3, adopted the properties of air from the Fluent database for air properties except that the density was set to a constant of 1.1839 kg/m^3, corresponding to air density at 25 °C [7]. No fluid flow was solved in regions where stagnant air was specified. Steel was found in the cradle, the supports of the girder, the springs between SAS’s and the waveguide flanges. The default values in Fluent were used. Water was found in the different pipe circuits and solved with constant density. Default values were used.

3.9.3. Meshing

ICEM CFD v17.2 was used. A tetrahedral mesh with approximately 100 million elements was generated. This slightly exceeded the physical memory of the workstation of 24 GB. Further increase in the number of elements would drastically increase the mesh generation and loading times since the machine would switch to the hard disk for virtual memory space. The smallest elements were set to have a maximum size of 1.6 mm, and the time estimated to achieve convergence was approximately 1 week.

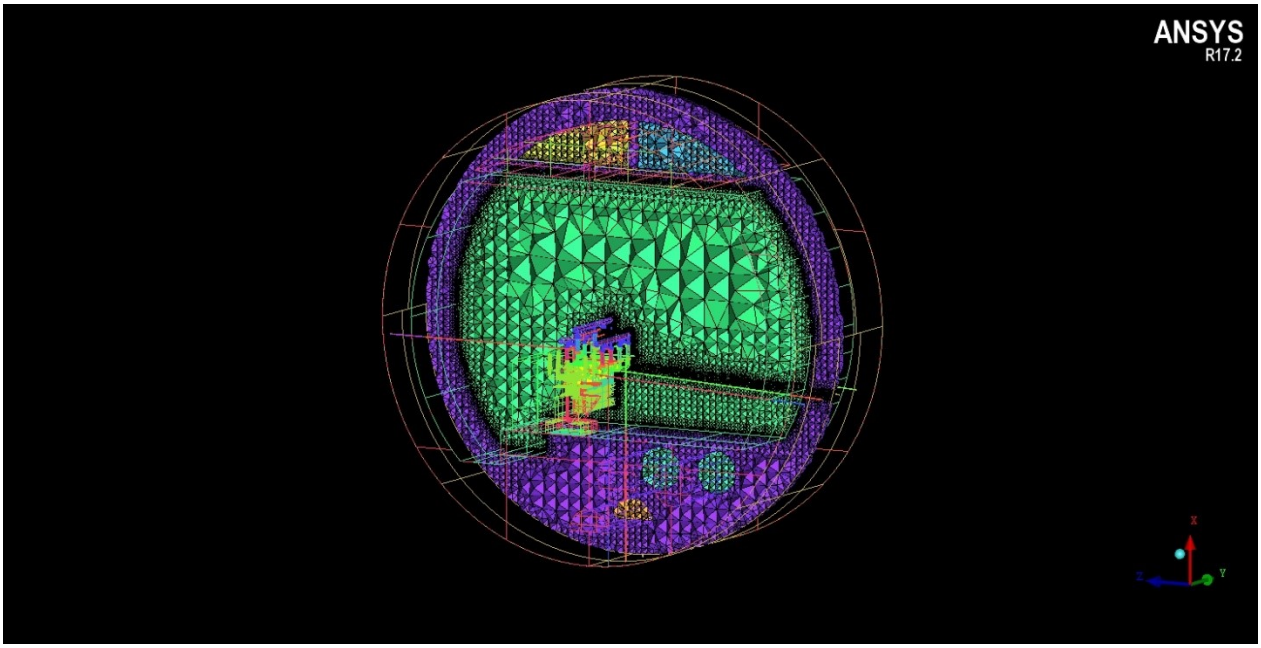

Figure 37: Cross section of the mesh, 3D, main-beam-tunnel-wall

Figure 37 shows a cross section of the mesh in 3D. The dummy regions, and the block for the drive beam were not meshed, since no physics would be solved in these regions. The interested reader should look at the original mesh files, since it takes heavy computer resources to visualise the mesh and produce screenshots for every detail. Nevertheless, Figure 38 to Figure 46 offer some of the cross sections for reference.

Figure 38 shows a cross section of the mesh. The tunnel geometry and structures can easily be seen. Figure 39 shows a zoomed-in cross section. The blank rectangle is the drive beam part of the module and is not meshed. Figure 40 shows another zoomed-in view, focusing on the main beam part. The blank regions are vacuum. Figure 41 zooms in further to the SAS. The deep blue regions within the SAS are the heating elements. Figure 42 zooms to the CL. It can be seen that the pipe walls are connected to the CL structure. The violet region is water. The thin layer in sky blue within the CL is the heating element. Figure 43 shows a cross section from the side. The dummy regions can be identified, where no mesh is present. The geometry on the very left is the same as the geometry on the very right – the mesh can be made periodic. Figure 44 offers a zoomed-in view of some of the dummy regions. Figure 45 displays another cross section from the side. At this cross section, the stagnant air within the girder can be seen (blue). Figure 46 zooms in to the dummy regions at this cross section.

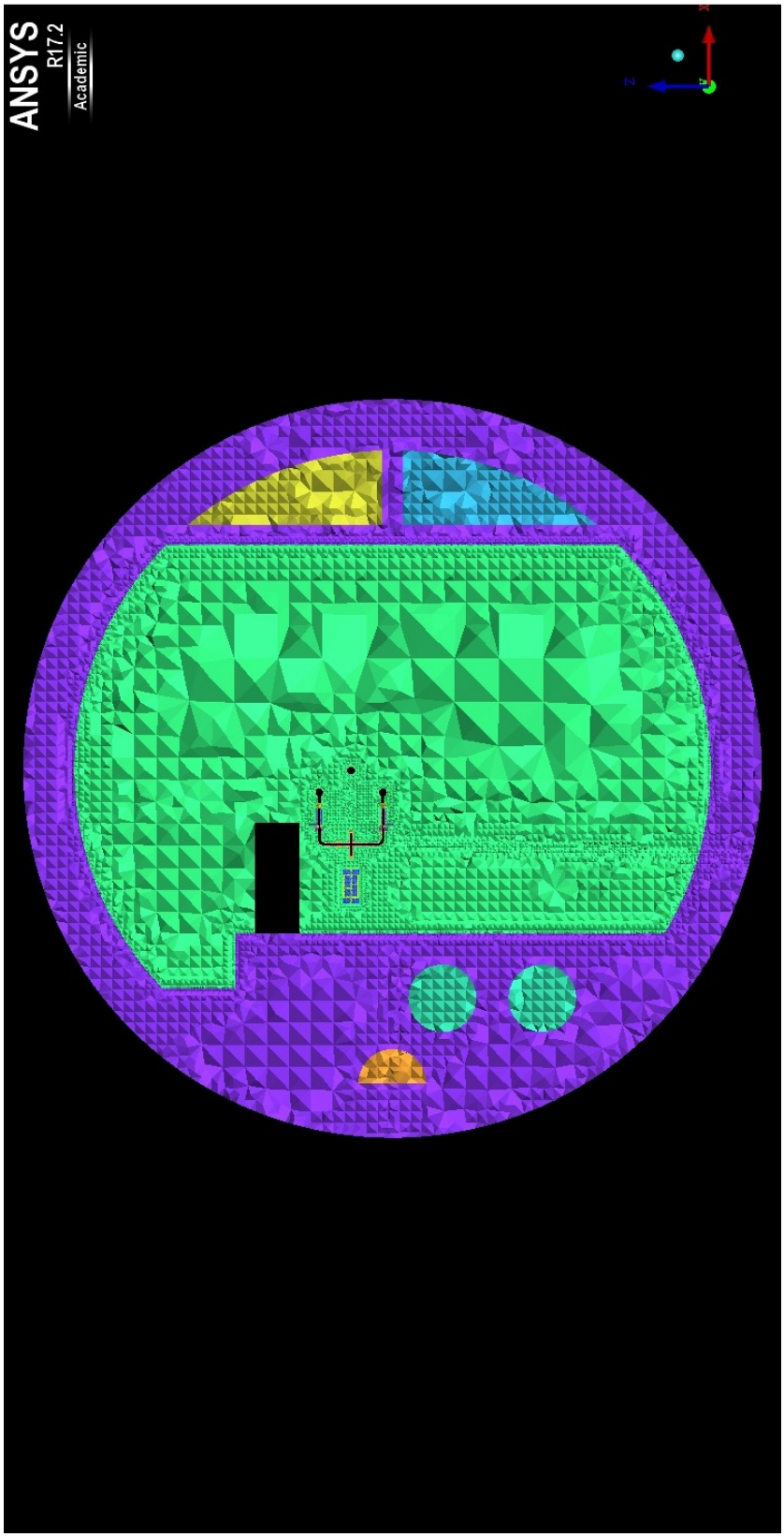

Figure 38: Cross section of the mesh, main-beam-tunnel-wall

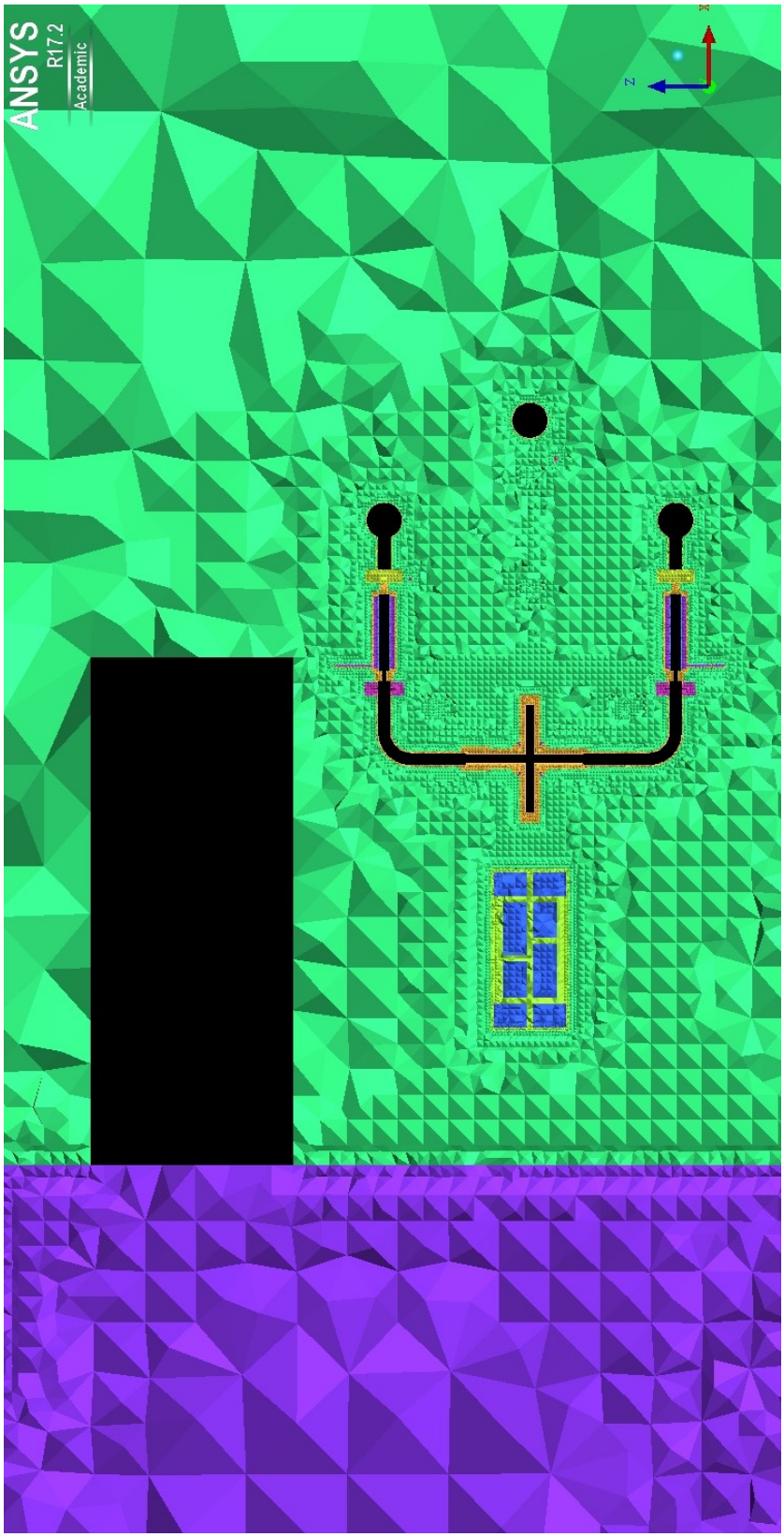

Figure 39: Cross section of the mesh, module, main-beam-tunnel-wall

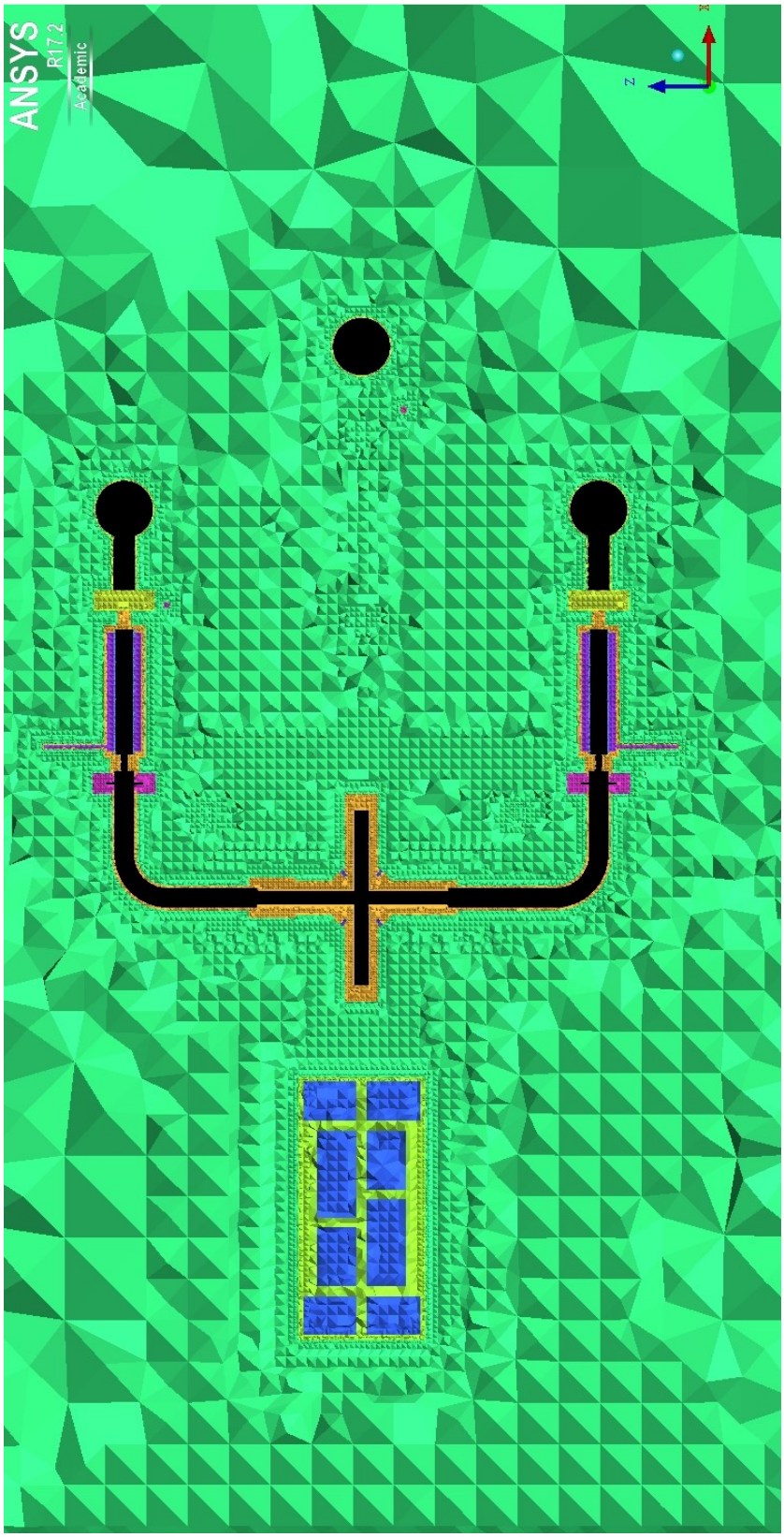

Figure 40: Cross section of the mesh, main beam, main-beam-tunnel-wall

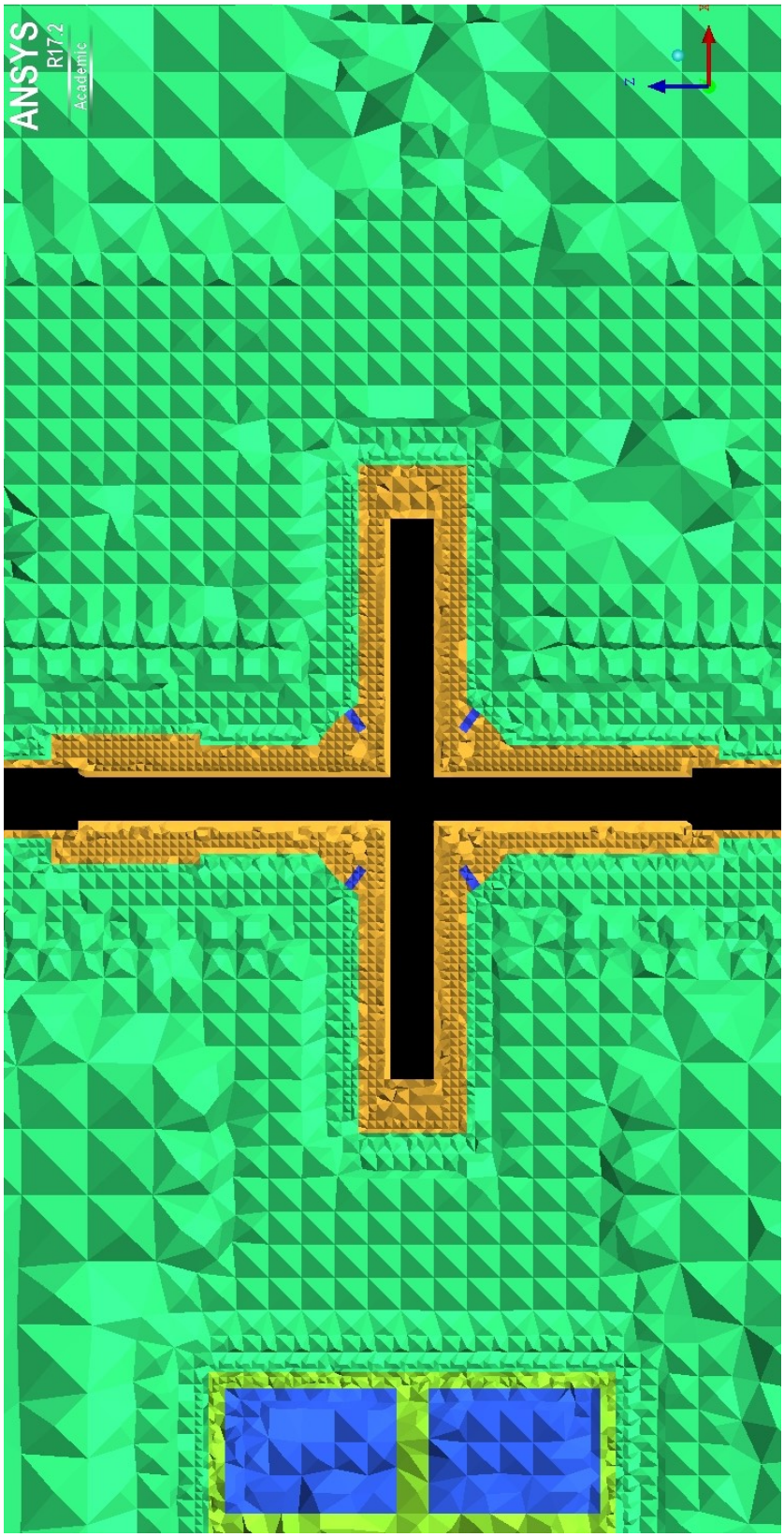

Figure 41: Cross section of the mesh, SAS, main-beam-tunnel-wall

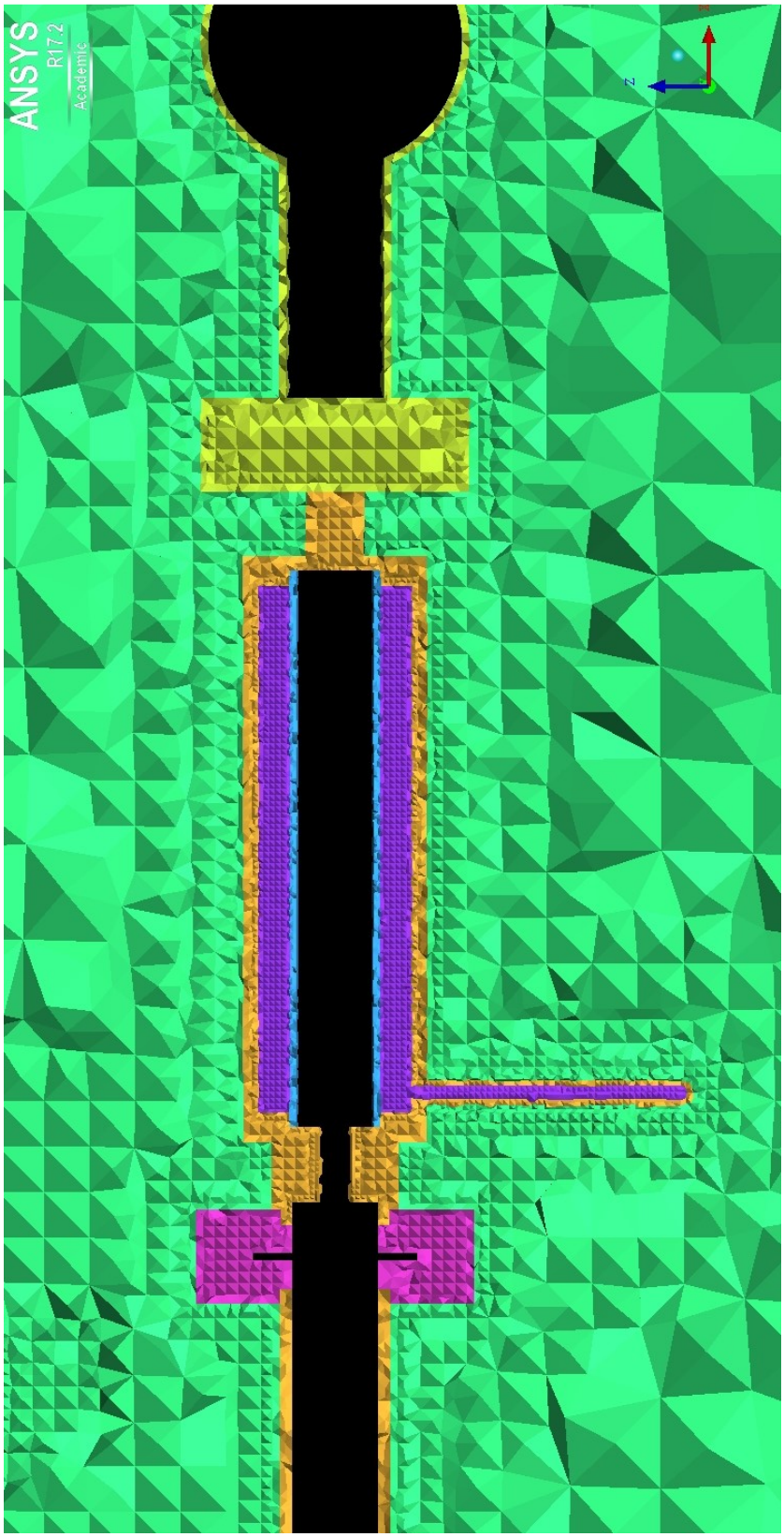

Figure 42: Cross section of the mesh, CL, main-beam-tunnel-wall

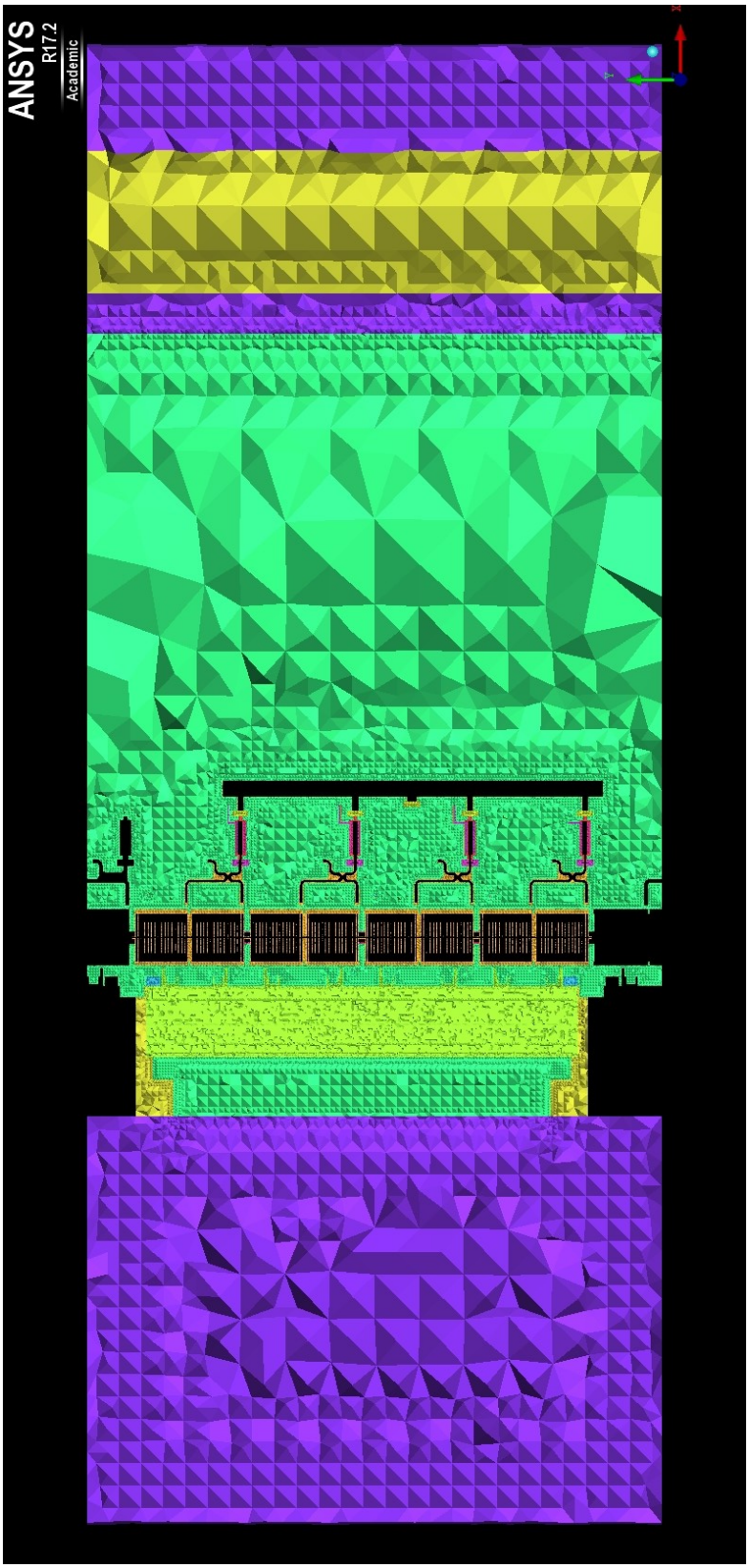

Figure 43: Cross section of the mesh, main-beam-tunnel-wall

Figure 44: Cross section of the mesh, dummy structures, main-beam-tunnel-wall

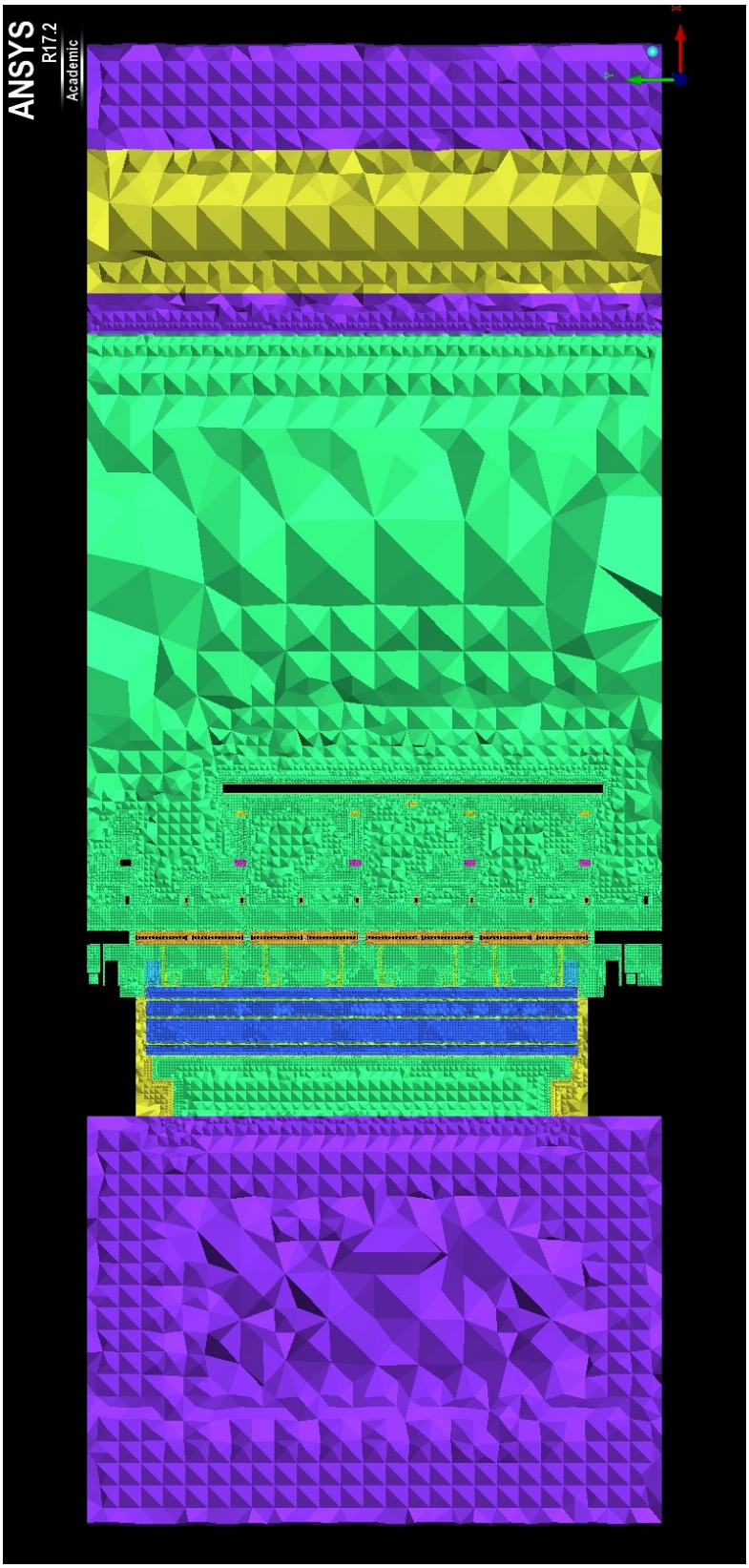

Figure 45: Cross section of the mesh, main-beam-tunnel-wall

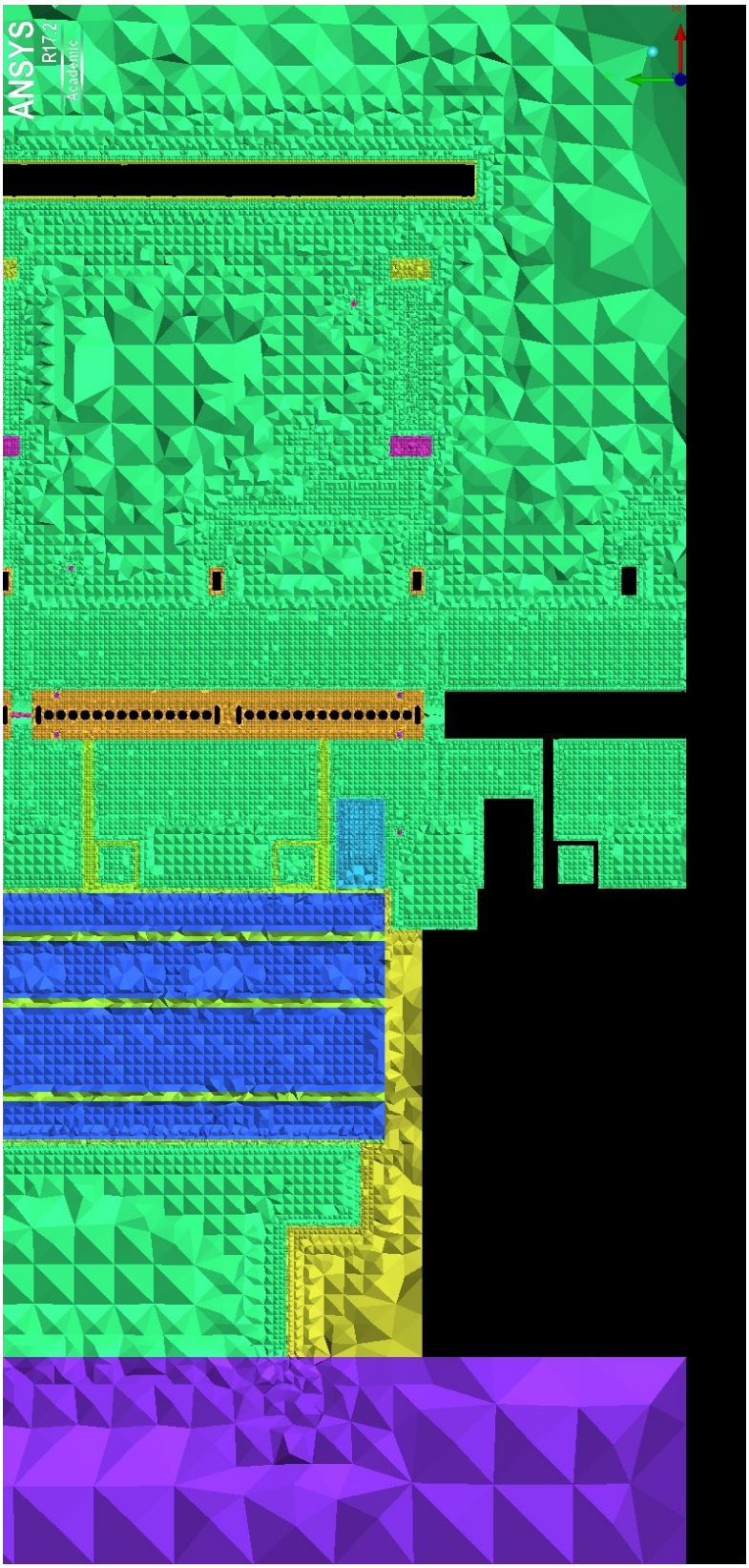

Figure 46: Cross section of the mesh, dummy structures, main-beam-tunnel-wall

3.9.4. Boundary conditions

The boundary conditions set were similar to those described in Section 3.7.4 and were simply extended to this case. There were some new settings, however. In this case, water did not participate in radiation. Also, the pipes participated in convective and radiation heat transfer to the tunnel air but not any heat transfer to the stagnant air and tunnel concrete.

3.9.4.1. Heat generation values

Heat generation values were prescribed in units of power per unit volume.

For the compact loads in the geometry file, each heating element had a volume of 18511.0493 mm^3. Each compact load generated 150 W of heat [21], therefore the prescribed heat generation was 8103268.3544 W/m^3.

For the SAS in the geometry file, the four heating elements near the main beam per SAS had a total volume of 60092.7963 mm^3 and generated a total heat of 780 W. Therefore, the prescribed heat generation was 12979925.1828 W/m^3.

3.9.5. Under-relaxation factors

The under-relaxation factors were problem-specific and required adjustments to the initial guesses. The following corrections were used after several attempts: pressure (0.6); momentum (0.6); energy (0.5). The others remain unchanged as in Section 3.2.3.3. The length scale under *Pseudo Transient Options* was changed to 2 m.

3.9.6. Results

Up to the completion of the traineeship on 28.02.2018, the model was still running on the CERN cluster and had not fully converged. Nevertheless, the intermediate results are reported as follows.

3.9.6.1. Case 1 – Only 4 SAS's heated

The first case concerns that only the heating elements lying in the 4 super-accelerating structures were switched on. The results are reported from Table 3 to Table 6. Note that the results were not sufficiently converged, as evident in the difference between the total heat dissipated and the theoretical total heat dissipation, which was calculated from the nominal values.

	Air inlet at 21 °C, 0.4 m/s Water inlet at 27 °C, 1.3 L/min 4 circuits to 4 SAS+CL sets 1 circuit to the CL set at the top
Heat to air (W)	600.95
Heat to 1st SAS + CL1 water (W)	646.14
Heat to 2nd SAS + CL2 water (W)	639.11
Heat to 3rd SAS + CL3 water (W)	637.43
Heat to 4th SAS + CL4 water (W)	620.98
Heat to TOPCL water (W)	-33.877
Total heat dissipated (W)	3110.73
Theoretical total heat dissipation (W)	780 * 4 = 3120

Table 3: Heat dissipation from the module, 4 SAS's heated, main-beam-tunnel-wall

	Air inlet at 35 °C, 0.4 m/s Water inlet at 27 °C, 1.3 L/min 4 circuits to 4 SAS+CL sets 1 circuit to the CL set at the top
Heat to air (W)	-29.401
Heat to 1st SAS + CL1 water (W)	808.00
Heat to 2nd SAS + CL2 water (W)	783.85
Heat to 3rd SAS + CL3 water (W)	782.52
Heat to 4th SAS + CL4 water (W)	805.01
Heat to TOPCL water (W)	68.116
Total heat dissipated (W)	3218.1
Theoretical total heat dissipation (W)	780 * 4 = 3120

Table 4: Heat dissipation from the module, 4 SAS's heated, main-beam-tunnel-wall

	Air inlet at 21 °C, 0.4 m/s Water inlet at 27 °C, 1.3 L/min 4 circuits to 4 SAS+CL sets 1 circuit to the CL set at the top
1st SAS + CL1 water ΔT (°C)	6.86
2nd SAS + CL1 water ΔT (°C)	7.03
3rd SAS + CL1 water ΔT (°C)	7.02
4th SAS + CL1 water ΔT (°C)	6.85
TOPCL water ΔT (°C)	-0.38

Table 5: Water ΔT, 4 SAS's heated, main-beam-tunnel-wall

	Air inlet at 35 °C, 0.4 m/s Water inlet at 27 °C, 1.3 L/min 4 circuits to 4 SAS+CL sets 1 circuit to the CL set at the top
1st SAS + CL1 water ΔT (°C)	8.62
2nd SAS + CL1 water ΔT (°C)	8.63
3rd SAS + CL1 water ΔT (°C)	8.61
4th SAS + CL1 water ΔT (°C)	8.88
TOPCL water ΔT (°C)	0.74

Table 6: Water ΔT, 4 SAS's heated, main-beam-tunnel-wall

3.9.6.2. Case 2 – 4 SAS's and 20 CLs heated

The second case concerns that apart from the heating elements in the 4 SAS's, the 20 CLs were as well heated. Again, note that the results were not sufficiently converged. The results are reported from Table 7 to Table 10.

	Air inlet at 21 °C, 0.4 m/s Water inlet at 27 °C, 1.3 L/min 4 circuits to 4 SAS+CL sets 1 circuit to the CL set at the top
Heat to air (W)	698.44
Heat to 1st SAS + CL1 water (W)	1231.0
Heat to 2nd SAS + CL2 water (W)	1222.1
Heat to 3rd SAS + CL3 water (W)	1221.8
Heat to 4th SAS + CL4 water (W)	1205.1
Heat to TOPCL water (W)	539.64
Total heat dissipated (W)	6118.08
Theoretical total heat dissipation (W)	780 * 4 + 150 * 20 = 6120

Table 7: Heat dissipation from the module, 4 SAS's & 20 CLs heated, main-beam-tunnel-wall

	Air inlet at 35 °C, 0.4 m/s Water inlet at 27 °C, 1.3 L/min 4 circuits to 4 SAS+CL sets 1 circuit to the CL set at the top
Heat to air (W)	-132.74
Heat to 1st SAS + CL1 water (W)	1452.9
Heat to 2nd SAS + CL2 water (W)	1368.1
Heat to 3rd SAS + CL3 water (W)	1366.1
Heat to 4th SAS + CL4 water (W)	1396.3
Heat to TOPCL water (W)	645.70
Total heat dissipated (W)	6086.36
Theoretical total heat dissipation (W)	780 * 4 + 150 * 20 = 6120

Table 8: Heat dissipation from the module, 4 SAS's & 20 CLs heated, main-beam-tunnel-wall

	Air inlet at 21 °C, 0.4 m/s Water inlet at 27 °C, 1.3 L/min 4 circuits to 4 SAS+CL sets 1 circuit to the CL set at the top
1st SAS + CL1 water ΔT (°C)	13.21
2nd SAS + CL1 water ΔT (°C)	13.43
3rd SAS + CL1 water ΔT (°C)	13.46
4th SAS + CL1 water ΔT (°C)	13.29
TOPCL water ΔT (°C)	5.94

Table 9: Water ΔT, 4 SAS's & 20 CLs heated, main-beam-tunnel-wall

	Air inlet at 35 °C, 0.4 m/s Water inlet at 27 °C, 1.3 L/min 4 circuits to 4 SAS+CL sets 1 circuit to the CL set at the top
1st SAS + CL1 water ΔT (°C)	14.82
2nd SAS + CL1 water ΔT (°C)	15.04
3rd SAS + CL1 water ΔT (°C)	15.19
4th SAS + CL1 water ΔT (°C)	15.65
TOPCL water ΔT (°C)	7.04

Table 10: Water ΔT, 4 SAS's & 20 CLs heated, main-beam-tunnel-wall

3.9.7. Comments

Although full convergence could not be achieved within the time limits, all of the elements essential to a successful simulation were put into place. Geometry was fixed, an error-free mesh was generated (previous attempts by others had failed due to errors reported from the meshing software), turbulence and radiation models tested with the simpler SAS case (Section 3.7), and the solution was converging, albeit slowly, after the adjustment of appropriate underrelaxation factors.

3.9.8. Future work

For future work, the first priority is to run the case to completion (convergence). After this is achieved, basic mesh independence tests should be performed. However, it is worth noting that the finest mesh reasonably possible on the current workstation had already been used. Therefore, such tests could only be performed backwards by decreasing the number of elements. The y^+ values should also be checked such that the first element should lie at least within the logarithmic layer.

Although the current solution converges, it is still desirable to adjust parameters in Fluent to speed up convergence and then perform a parametric study.

The current case made use of a uniform velocity for the inlet. Ideally, periodicity should be introduced so that the flow field can converge to a fully developed scenario.

4. Finite-Element Simulations for Structural Behaviour Determination

4.1. Introduction

As a side project of the first author's traineeship, finite-element simulations were performed for the adjustable supports of the SAS, including stress-strain simulations for the maximum adjustment window of the mechanism, as well as modal analysis for the supports attached to the SAS. The material of the adjustable supports was 30CrNiMo8, with a yield strength of 1.034 GPa [22]. All of the geometries were provided by J. I. Vainola.

4.2. Software and general workflow

This section describes the workflow generally followed in this work to perform a finite-element analysis of the structural responses of the module.

The source STEP files were imported into ANSYS Mechanical via the Workbench environment. Materials were assigned to different parts of the geometry. Then, it was necessary to specify the contacts. This had to be carefully performed since the contacts affect the final result significantly. There are 5 available contact types in ANSYS Mechanical, namely bonded, no separation, frictionless, rough and frictional. Figure 47, obtained from [23], summarises well the difference between contacts. Otherwise, refer to the section "Definition Settings" in [24].

Contact Names and Behavior

Name	Gap Open/Close ?	Sliding Allowed ?
Bonded	No	No
Rough	Yes	No, infinite μ
No Separation	No	Yes, $\mu = 0$
Frictionless	Yes	Yes, $\mu = 0$
Frictional	Yes	Yes, if $F_{sliding} > F_{friction}$

Figure 47: Different contacts in ANSYS Mechanical [23]

In general, *no separation* was chosen for the contacts, since it was assumed not likely to have a gap at the contact, and the friction condition was not known. The contact behaviour was chosen to be symmetric. The *Augmented Lagrange* formulation was chosen after careful consideration for contacts between the bars and the sleeve. The normal stiffness factor for the *Augmented Lagrange* formulation was chosen after a sensitivity study, and the stiffness was updated each iteration. Next, a relatively fine mesh was generated, with *Physics Preference* set to *Nonlinear Mechanical*. Gravity and displacement constraints were imposed. The solution was monitored with the deformation and stresses of the bars, with convergence requirements of 1% for the global safety factor, as well as the equivalent stresses of the bars. The problem was solved with an iterative solver.

A very brief workflow was presented above. This report does not go into the details of the theory of the Augmented Lagrange algorithm, and the contact stiffness sensitivity studies. However, a summary is given below.

The Augmented Lagrange method is a penalty-based method. Compared to the pure-penalty method, this is less sensitive to the normal stiffness factor [24]. The stiffness factor controls the penetration behaviour at the contact, so that the two solids penetrate each other as little as possible. Large stiffness factors may introduce numerical issues whereas small stiffness factors introduce large errors. The normal stiffness factor can impact the results significantly, see [25] for an example. The Normal Lagrange method was not favoured because it required a direct solver [24]. The interested reader should refer to [24] for the theoretical formulations.

For the results reported in the following sections, a normal stiffness factor of 1 was chosen. This was chosen based on criteria of the lack of erroneous stress values and maximum stress locations; low contact penetration; and CPU time. The trend of the important solution parameters (e.g. maximum stresses and safety factors) was monitored to ensure that the solution was stable around the chosen stiffness factor. These studies are not presented in this report. The interested reader should go to the Excel and Word files left behind in the various folders for a detailed analysis.

4.3. Stress-strain simulations

4.3.1. Bar-sleeve case

The first problem included two bars and one sleeve. The material in this section is directly taken from the presentation in October 2017 [26].

4.3.1.1. Simplification

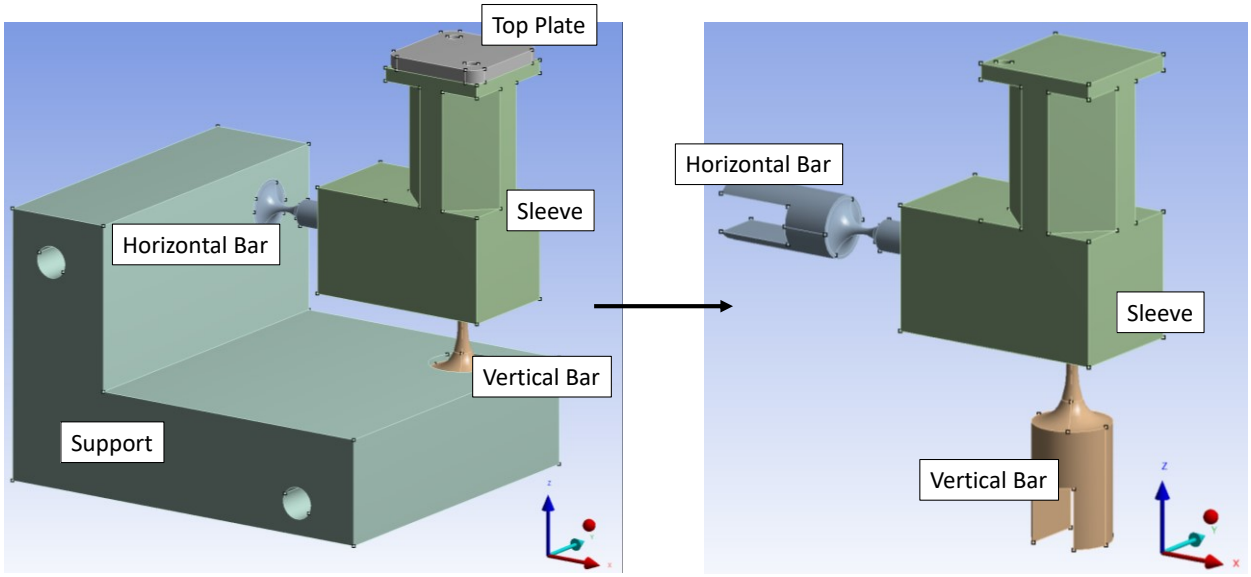

Figure 48: Simplification, bar-sleeve

The model was first simplified. Refer to the left of Figure 48. There is a plate between the top of the sleeve and the SAS. This plate was suppressed since it was assumed to be always bonded to the sleeve. The support was as well suppressed because it constituted additional mesh elements and additional contact conditions (at the interfaces between the bars and the support). Such additional conditions gave rise to more assumptions and convergence difficulties. Some test simulations were run, and they revealed negligible deformations of the support structure (~10 nm). The result of the simplification is seen on the right of Figure 48.

4.3.1.2. Contact definition and solution method

There were two contacts, i.e. between the horizontal bar and the sleeve; and between the vertical bar and the sleeve. The contact was specified to be *No Separation*, which allows frictionless sliding but not gaps between the surfaces. The algorithm chosen was Augmented Lagrange. The settings were according to Section 4.2.

4.3.1.3. Mesh and convergence

Initially, there were about 400’000 elements in total. Adaptive mesh refinement was enabled, such that ANSYS automatically refined the mesh where necessary after a run, until the pre-set convergence criteria were reached. The convergence requirements were set to be that there was < 1% change in monitored values between two successive runs. The monitored values were 1) maximum equivalent stress in the two bars; and 2) safety factor of the system and of the two bars.

4.3.1.4. Cases considered

There were three groups of cases considered. For all the cases, vertical bars of 4 different neck thicknesses were tested. The horizontal bars remained unchanged.

The first group considered only the static load on top of the sleeve, of 228.69 N. This assumed 3 supports for the weight of the SAS, 46.623 kg, multiplied by a safety factor of 1.5 for the variation of loads [27]. The second group considered the load, with the displacement of the horizontal bar *or* the vertical bar. The displacement range was from 0.5 mm to 1.5 mm, in steps of 0.25 mm. The third group considered the load, with *simultaneous* displacements of the horizontal and vertical bars. The displacement range was from 0.25 mm to 1 mm, in steps of 0.25 mm.

4.3.1.5. Stress

This section reports the simulated stress values when the bars were displaced.

Displacement of the horizontal bar only

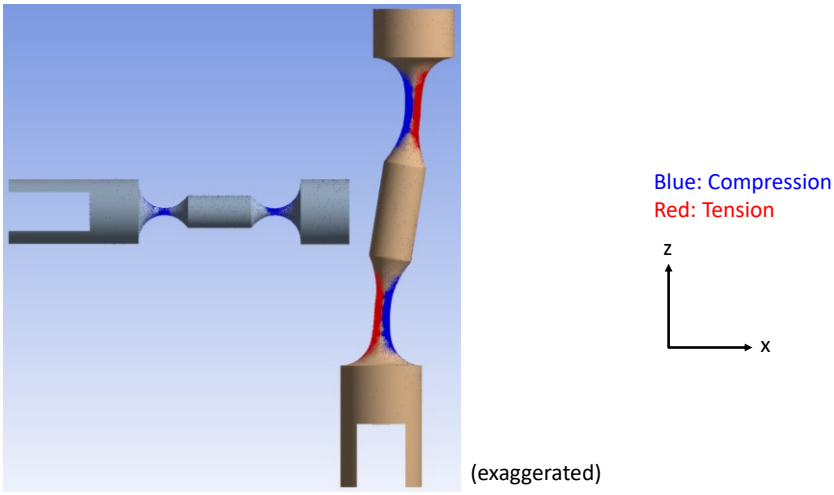

Figure 49: Stresses of the bars with horizontal bar displacement, bar-sleeve

Figure 49 shows the stresses of the bars when the horizontal bar was displaced. The colours indicate the state of compression or tension.

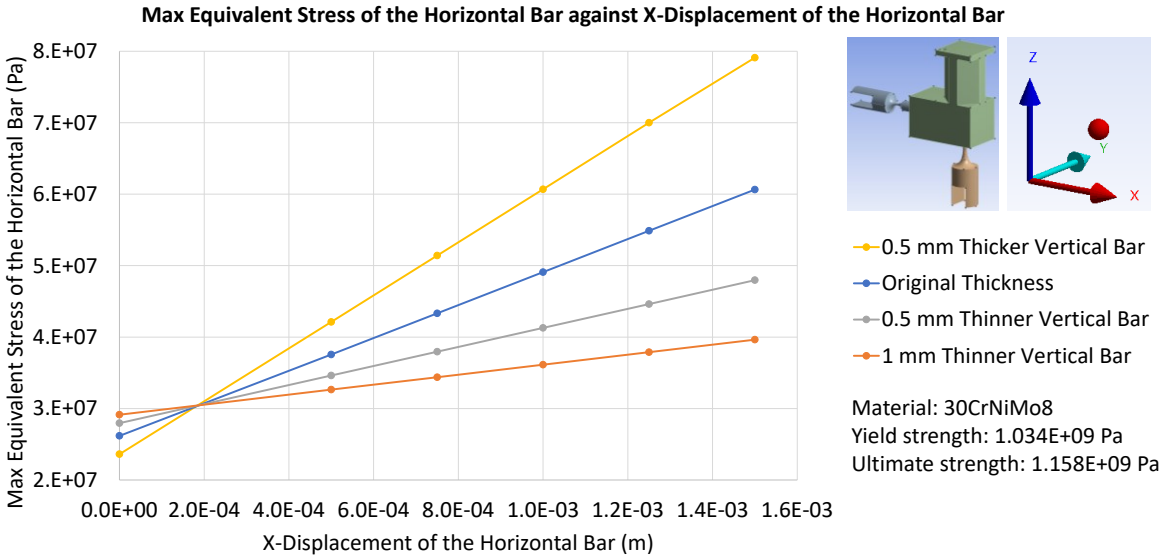

Figure 50: Maximum equivalent stress of the horizontal bar against horizontal bar displacement, bar-sleeve

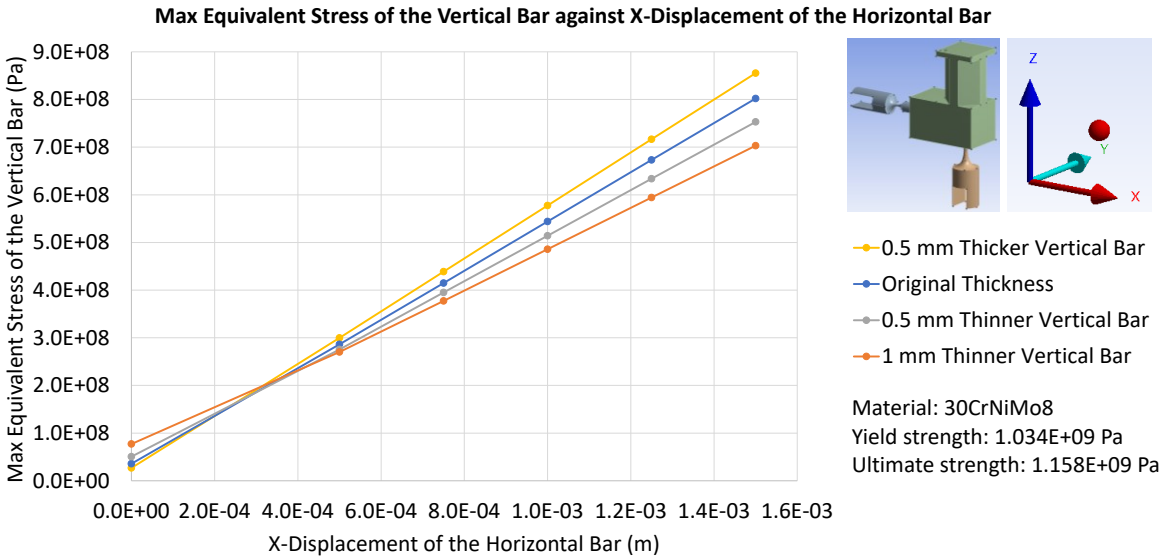

Figure 51: Maximum equivalent stress of the vertical bar against horizontal bar displacement, bar-sleeve

Figure 50 and Figure 51 show the maximum equivalent stress found in the horizontal bar and the vertical bar respectively, when the horizontal bar was displaced in the x-direction. It is clear that the stresses were linearly varying with the displacements, and that the vertical bar experienced a higher stress. Using a thinner vertical bar decreased the stresses in both the horizontal bar and the vertical bar.

Displacement of the vertical bar only

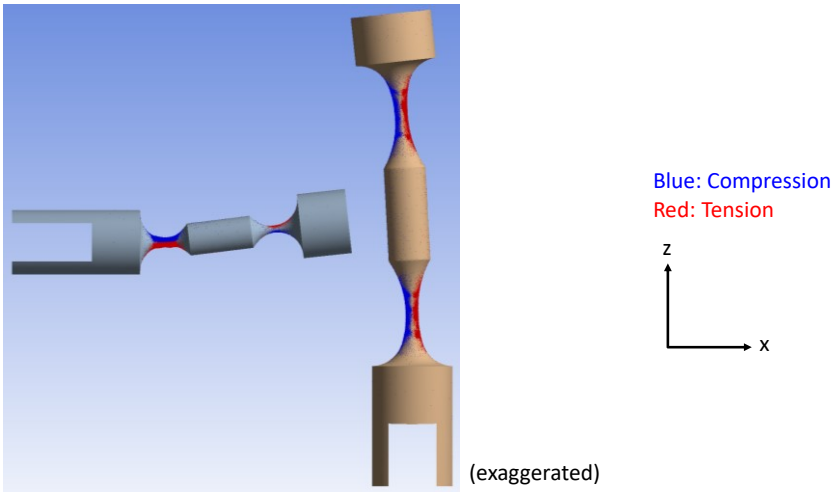

Figure 52: Stresses of the bars with vertical bar displacement, bar-sleeve

Figure 52 shows the stresses of the bars when the vertical bar is displaced. The colours indicate the state of compression or tension.

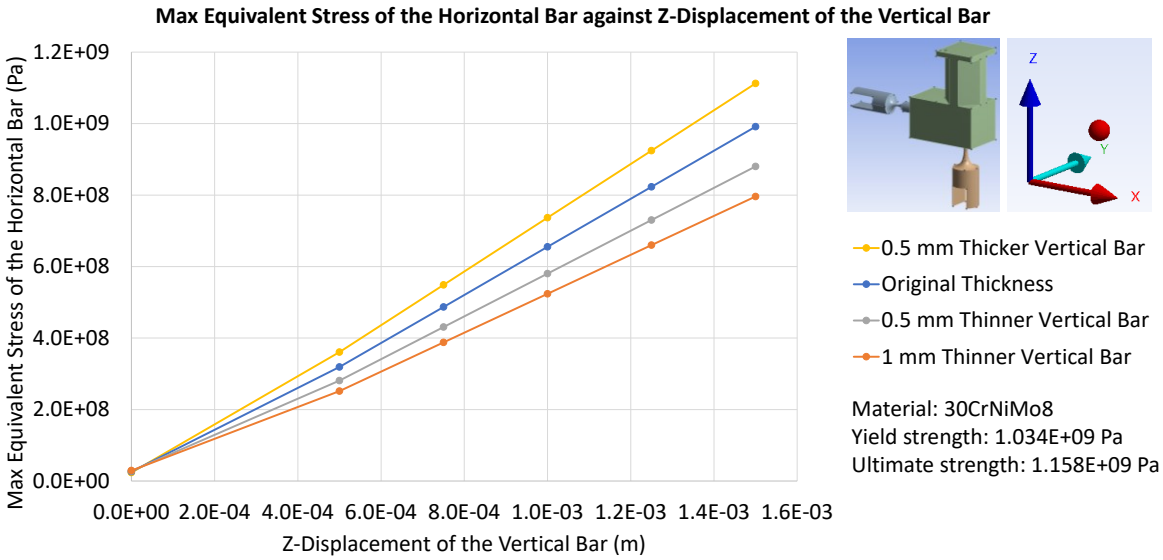

Figure 53: Maximum equivalent stress of the horizontal bar against vertical bar displacement, bar-sleeve

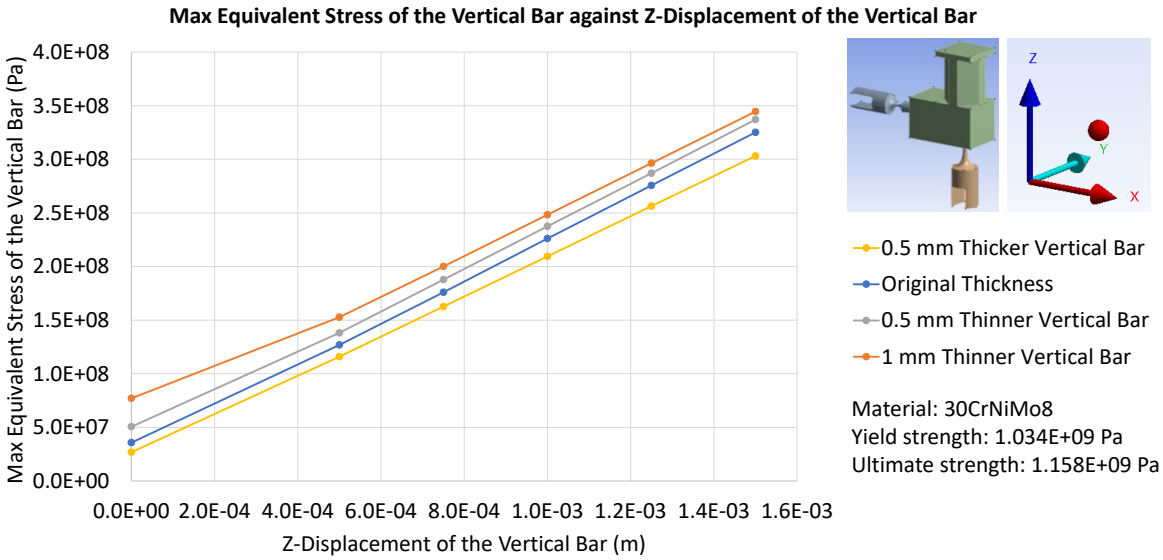

Figure 54: Maximum equivalent stress of the vertical bar against vertical bar displacement, bar-sleeve

Figure 53 and Figure 54 show the maximum equivalent stress found in the horizontal bar and the vertical bar respectively, when the vertical bar was displaced in the z-direction. Similarly, the stresses were more or less linearly varying with the displacements. In this case, the horizontal bar experienced a higher stress. Using a thinner vertical bar decreased the stress in the horizontal bar but increased the stress in the vertical bar. Nevertheless, the stress found in the horizontal bar was always higher than that in the vertical bar in the range tested and was thus the dominating factor.

Simultaneous displacement of both bars

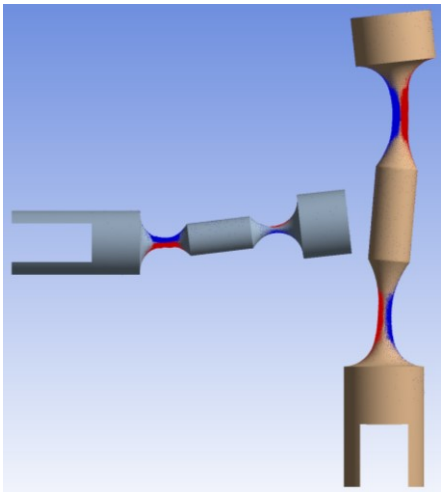

Figure 55: Stresses of the bars with simultaneous displacement of both bars, bar-sleeve

Figure 55 shows the stresses of the bars when both bars were displaced simultaneously. The colours indicate the state of compression or tension.

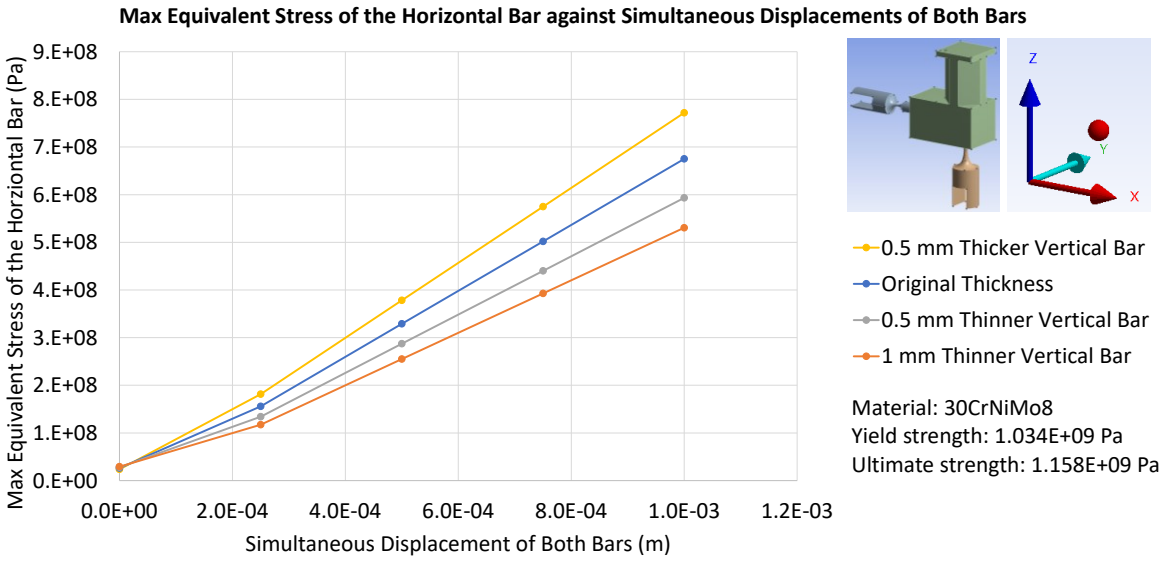

Figure 56: Maximum equivalent stress of the horizontal bar against simultaneous displacement of both bars, bar-sleeve

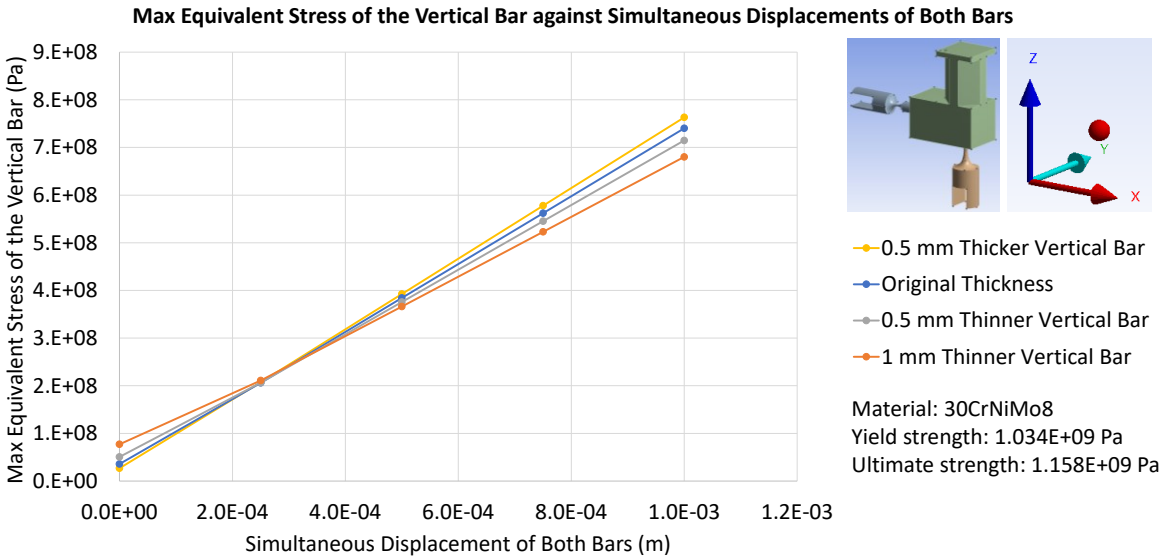

Figure 57: Maximum equivalent stress of the vertical bar against simultaneous displacement of both bars, bar-sleeve

Figure 56 and Figure 57 show the maximum equivalent stress found in the horizontal bar and the vertical bar respectively, when both bars were displaced simultaneously in their corresponding axial directions. The stresses were more or less linearly varying with the displacements. In this case, both bars experienced a similar magnitude of stresses. Using a thinner vertical bar decreased the stresses in both the horizontal bar and the vertical bar.

Extrapolation up to yield strength

Since the stress varied linearly with the displacements of the bars, and in some cases the range tested had not caused the maximum stress to reach the yield strength of the material, the stresses were extrapolated up to the yield strength, using Mathematica. The results are summarised in Table 11.

Neck of Vertical Bar	Displacement Range of the Horizontal Bar (Only Horizontal Adjustment)	Displacement Range of the Vertical Bar (Only Vertical Adjustment)	Displacement Range of Both Bars (Simultaneous Adjustment)
0.5 mm thicker	Up to 1.82521 mm	Up to 1.40390 mm	Up to 1.35708 mm
Original	Up to 1.95669 mm	Up to 1.58024 mm	Up to 1.41851 mm
0.5 mm thinner	Up to 2.10496 mm	Up to 1.78631 mm	Up to 1.48287 mm
1 mm thinner	Up to 2.30213 mm	Up to 1.98169 mm	Up to 1.59089 mm

Table 11: Displacement range from extrapolation, bar-sleeve

It can be seen that a thinner vertical bar allowed a wider displacement range while staying below the yield strength of the material. Note that these ranges were absolute limits and a safety margin should be allowed, also the displacement range reported includes one direction only. In theory the range in the opposite direction should be similar thus the actual full range should be double of the values reported above.

There were however a few limitations that were not considered in the simulation. The first limitation was that the tilting and movement of the top surface of the sleeve were not considered. In reality, there would be a reaction moment and reaction force from the load. The second limitation was that the force required to displace the bars could not be accurately estimated since the friction conditions between the bars and the support, and between the bars and the sleeve, were not known.

4.3.1.6. Tendency for the sleeve to tilt – Z-span

Since the reaction moments and reaction forces from the load were not known, no constraint was put on the surface except the weight of the load in the simulation. Nevertheless, a measure was used to give an idea of the tendency for the sleeve to tilt when the bars were displaced. It was termed as the z-span.

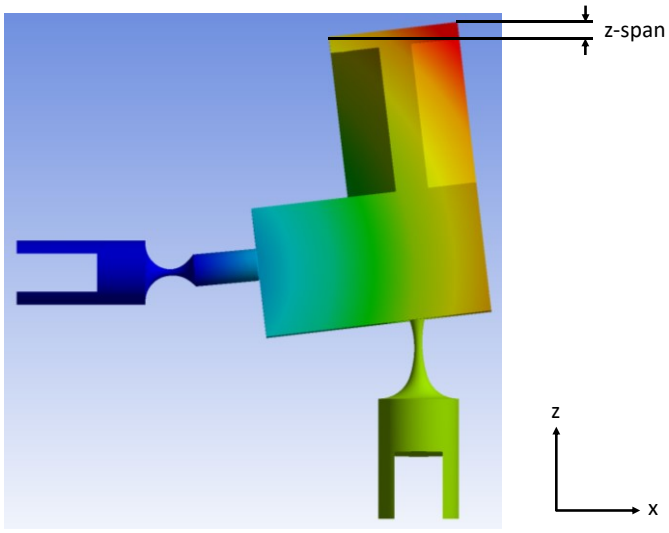

Figure 58: Definition of z-span, bar-sleeve

Figure 58 shows the z-span as defined (exaggerated for clarity). When the bars were displaced, there may be a tilt of the sleeve. The difference between the z-coordinate of the highest point and the lowest point of the top surface of the sleeve was the z-span. When without *any* loads and neglecting their own weight, it should be exactly 0.

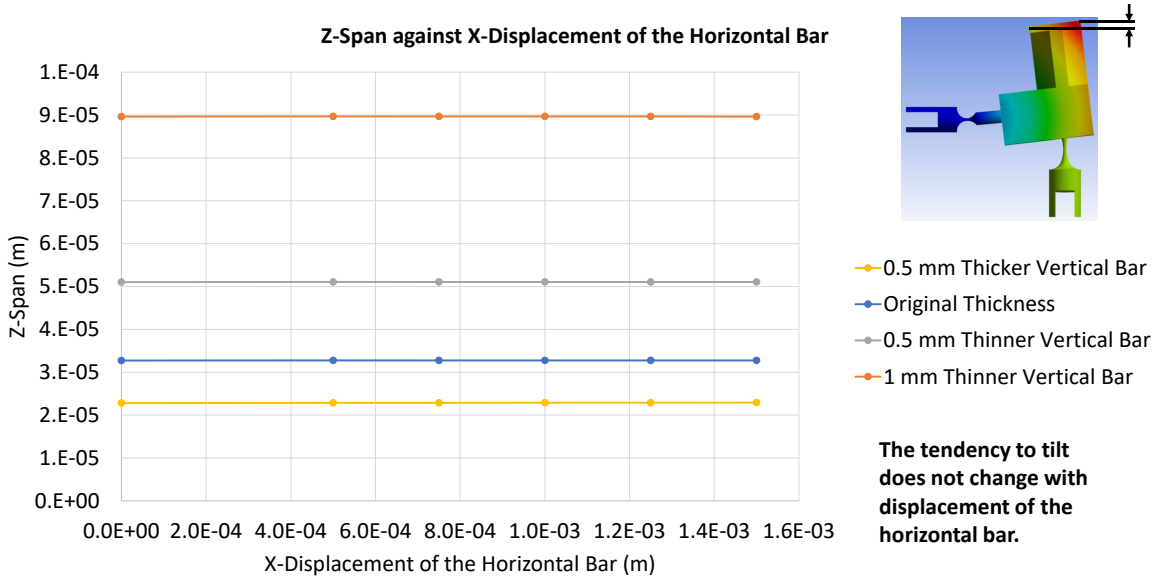

Figure 59: z-span against horizontal bar displacement, bar-sleeve

Figure 59 shows the z-span against the displacement of the horizontal bar in the x-direction. It can be seen that the z-span (tendency to tilt) did not change with horizontal bar displacement. Using a thinner vertical bar increased the tendency to tilt.

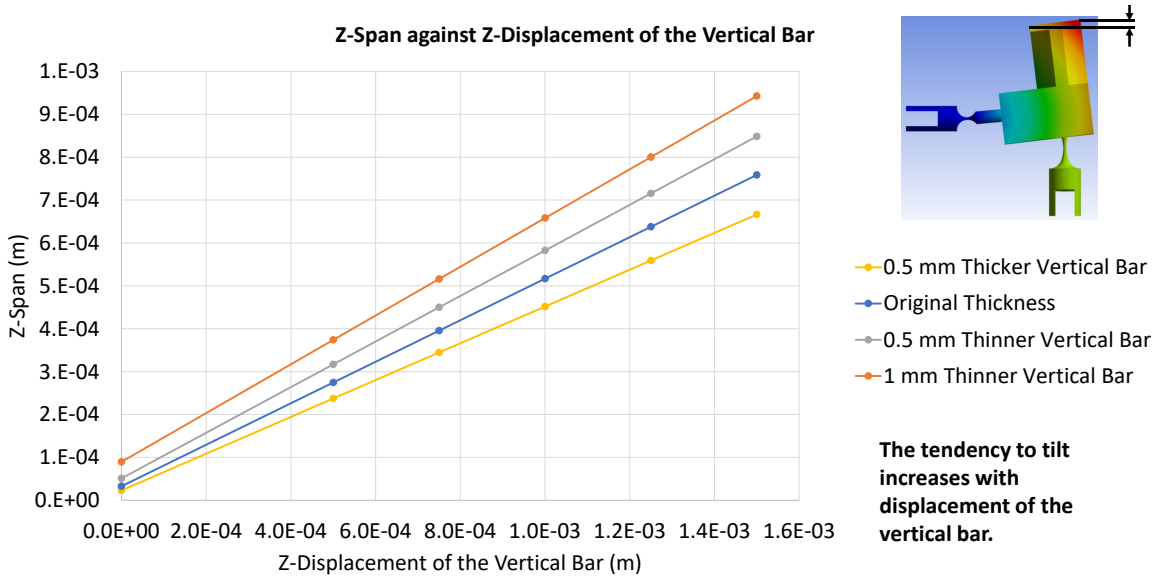

Figure 60: z-span against vertical bar displacement, bar-sleeve

Figure 60 shows the z-span against the displacement of the vertical bar in the z-direction. It can be seen that the tendency to tilt increased linearly with vertical bar displacement. Using a thinner vertical bar increased the tendency to tilt.

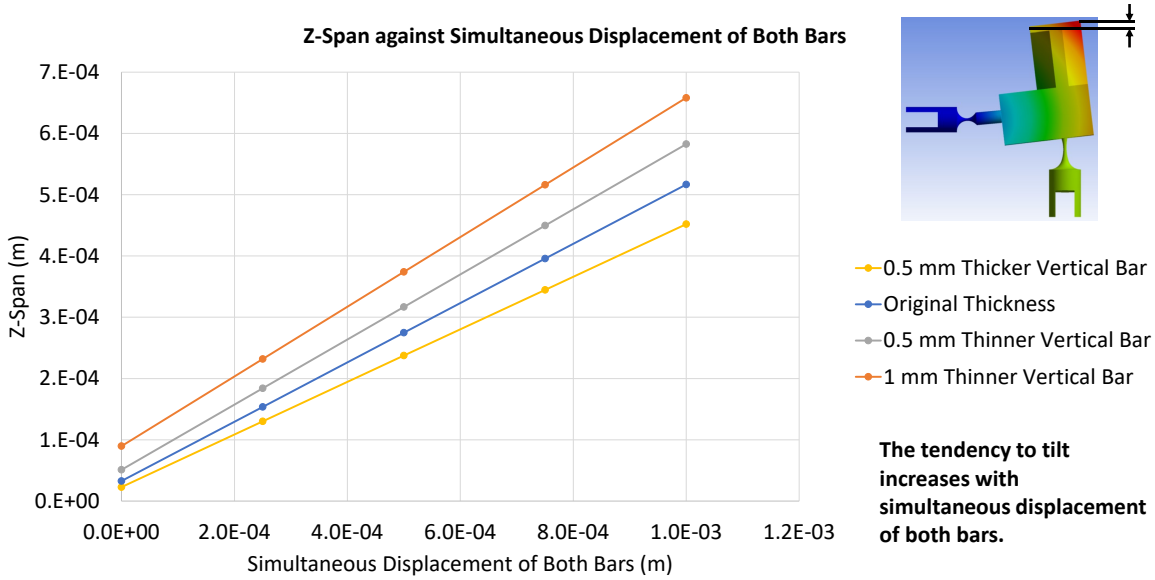

Figure 61: z-span against simultaneous displacement of both bars, bar-sleeve

Figure 61 shows the z-span against the simultaneous displacement of both bars. Similarly, the tendency to tilt increased linearly with simultaneous displacement of both bars. Using a thinner vertical bar increased the tendency to tilt.

4.3.1.7. Force for bar displacement

This section reports the force required for the bar displacements. Note that these are estimates since the friction conditions between the bars and the support, and between the bars and the sleeve were not known.

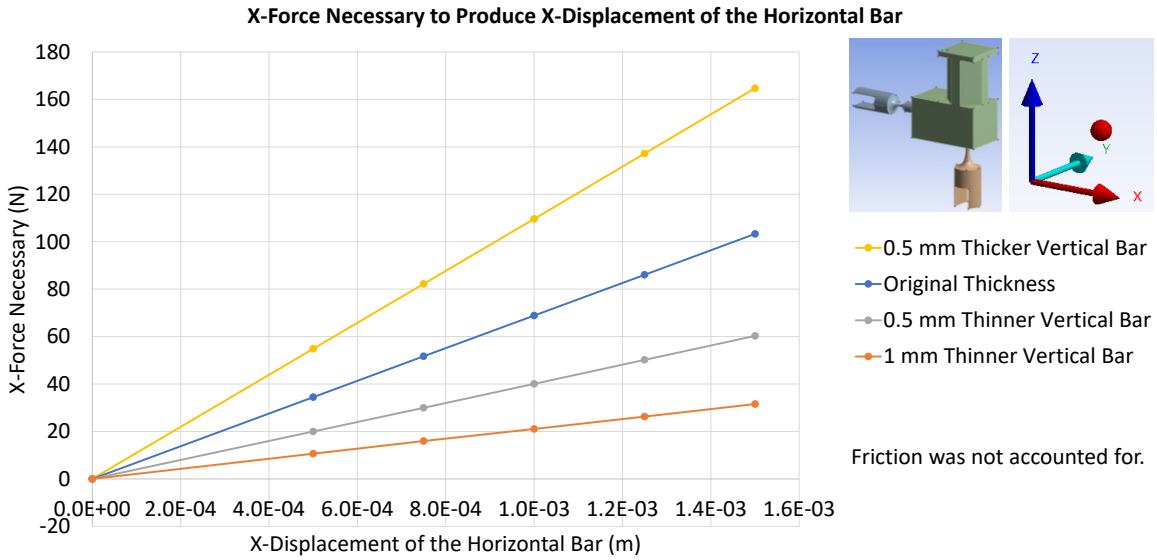

Figure 62: Horizontal force to produce horizontal bar displacement, bar-sleeve

Figure 62 shows the horizontal force required to produce displacement of the horizontal bar. The force required varied linearly with the displacement. A thinner vertical bar led to a smaller required force.

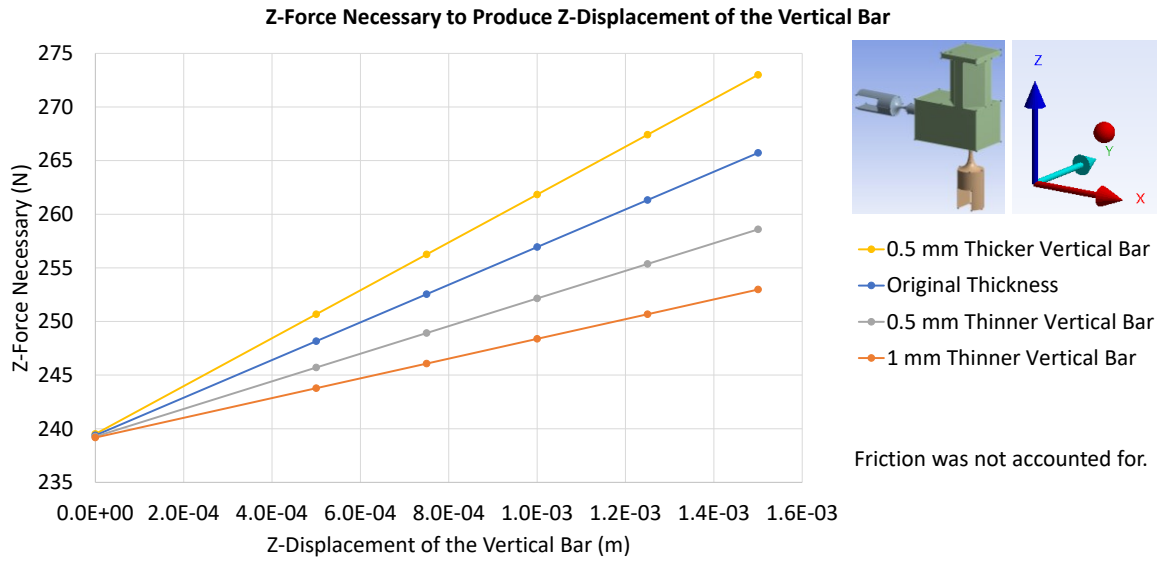

Figure 63: Vertical force to produce vertical bar displacement, bar-sleeve

Figure 63 shows the vertical force required to produce displacement of the vertical bar. The force required varied linearly with the displacement. A thinner vertical bar led to a smaller required force.

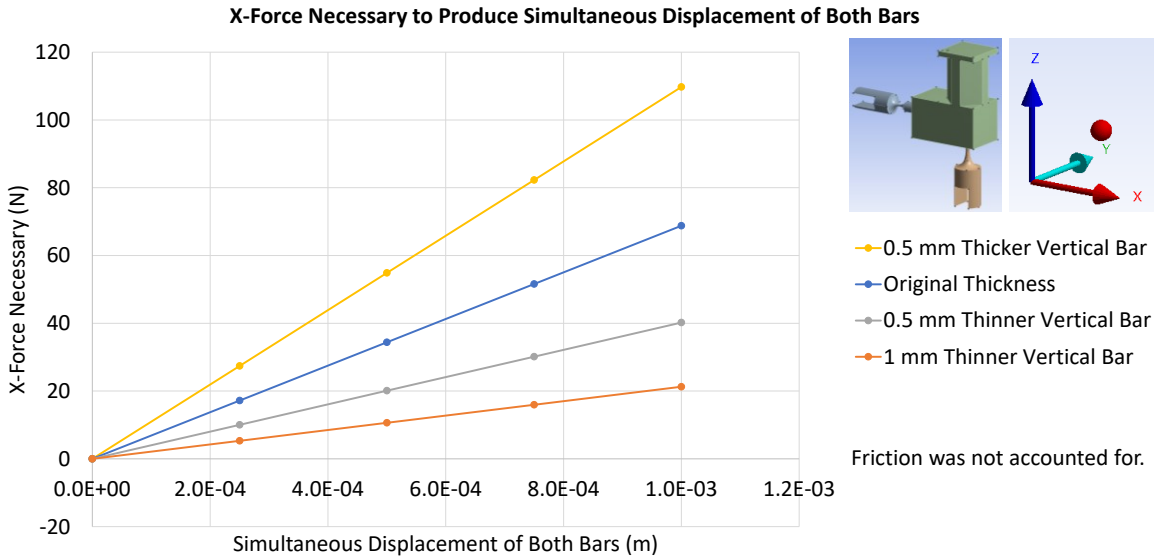

Figure 64: Horizontal force to produce simultaneous displacement of both bars, bar-sleeve

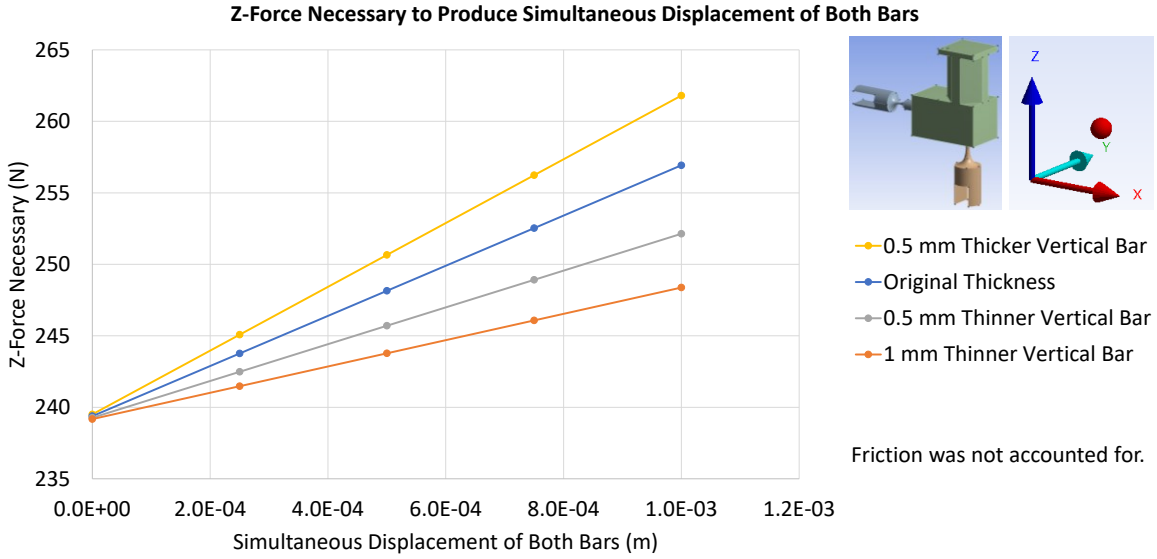

Figure 65: Vertical force to produce simultaneous displacement of both bars, bar-sleeve

Figure 64 and Figure 65 show the horizontal and vertical force required to produce simultaneous displacement of both bars. The forces required varied linearly with the displacements. A thinner vertical bar leads to a smaller required force.

4.3.1.8. Conclusions

The conclusions drawn from Section 4.3.1.5 to Section 4.3.1.7 are summarised. First, thinner vertical bars created lower stresses and increased the adjustment range. Thinner vertical bars as well required smaller forces to perform adjustments. However, using thinner vertical bars made the sleeve more likely to tilt. This may need to be taken into consideration during actual application.

4.3.2. Bar-sleeve-SAS case

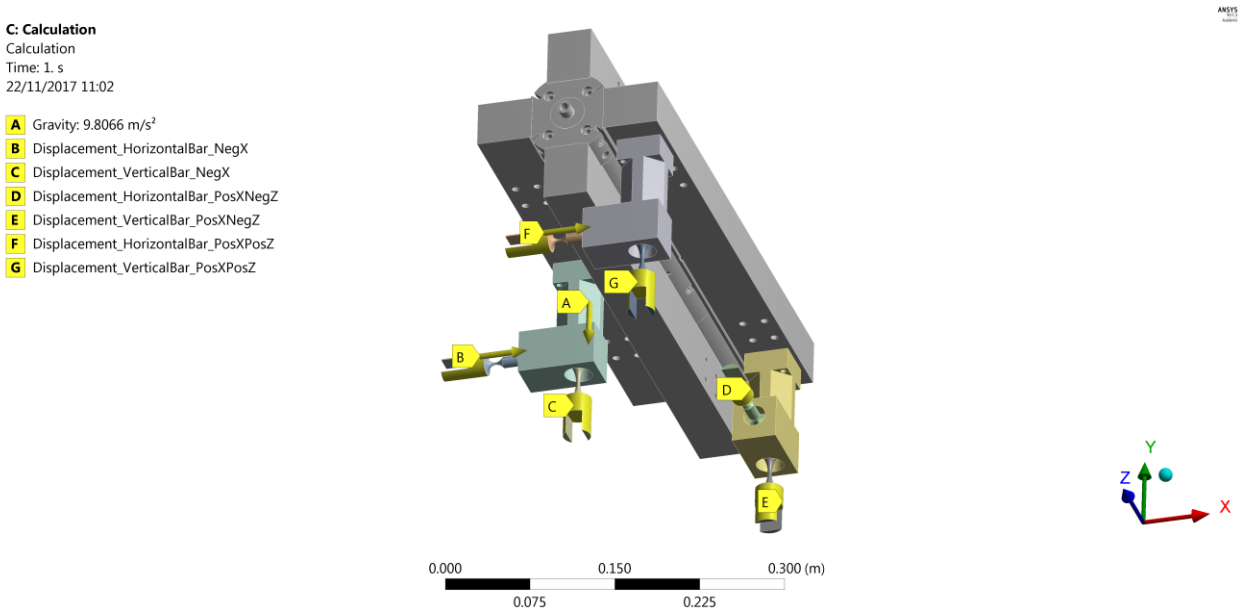

Figure 66: Geometry, bar-sleeve-SAS

The problem was extended to include the SAS itself so to address the tilting issue as characterised by the z-span measure (Section 4.3.1.6). The presence of the SAS would introduce reaction forces and reaction moments. Some minor adjustments were made to the sleeve so to fit with the SAS mock-up geometry.

Figure 66 shows a screenshot of the ANSYS Mechanical case for stress-strain simulations with the SAS. The letter A represents the gravitational force. Letters B – G refer to the displacements of the bars. For simplicity, the bars are named with their corresponding displacement letters, i.e. Bars B – G.

For simplicity, the material of the SAS was kept as steel, with only a modified density to correspond to the actual weight of the structure. Adaptive mesh refinement was not enabled in this case due to technical issues with the cluster. The solution methods were kept the same as described in 4.2. The contacts between the bars and the sleeves were *No Separation*, while the contacts between the sleeves and the SAS was *Bonded*. For *Bonded* contacts, the MPC formulation was chosen because of its simplicity. Again, the interested reader should refer to [24] for the theoretical background for such algorithms.

4.3.2.1. Moving Bars B and F

Here, Bars B and F were moved simultaneously by the same magnitude and direction (pushing into the sleeve). The highest stress was always observed in Bar D. Different geometries were as well tested for Bar D, namely:

1. Original
2. D1-5L50
3. D1-5L60
4. D1-25L50
5. D1-25L60

They differ by the neck thickness, and the length of the bar. The material was the kept the same as 30CrNiMo8.

Geometry	Displacement range of Bars B and F before Bar D Yields
Original	~ 0.75 mm
D1-5L50	~ 0.9 mm
D1-5L60	~ 1.2 mm
D1-25L50	~ 1 mm
D1-25L60	~ 1.25 mm

Table 12: Displacement range, bar-sleeve-SAS

Table 12 shows the results obtained from the stress-strain simulations in terms of maximum displacement range. They are concluded from Figure 67 to Figure 76. Note that, similarly, these displacement values are absolute, and that they show displacement range in only one direction.

Figure 67 to Figure 76 summarises the variation of safety factor with the displacements of Bars B and F when different geometries of Bar D were considered.

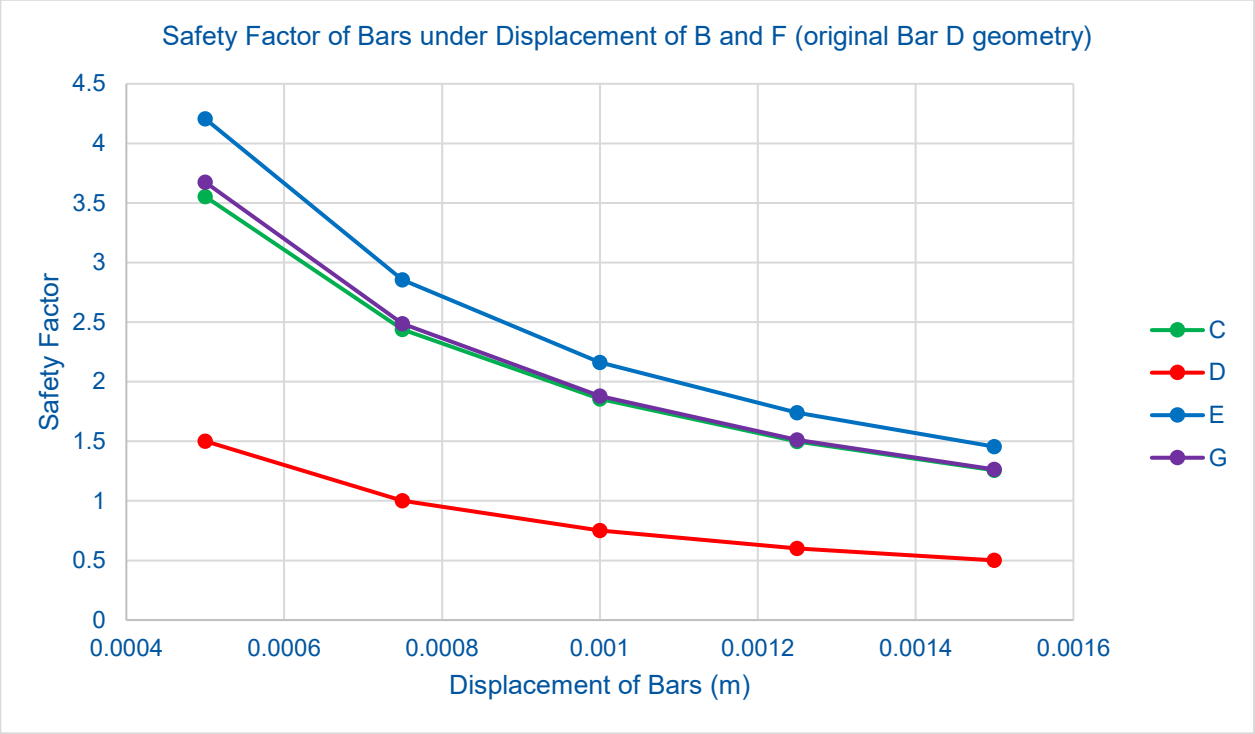

Figure 67: Safety factor of Bars C, D, E, and G under the displacement of Bars B and F, with original Bar D geometry, bar-sleeve-SAS

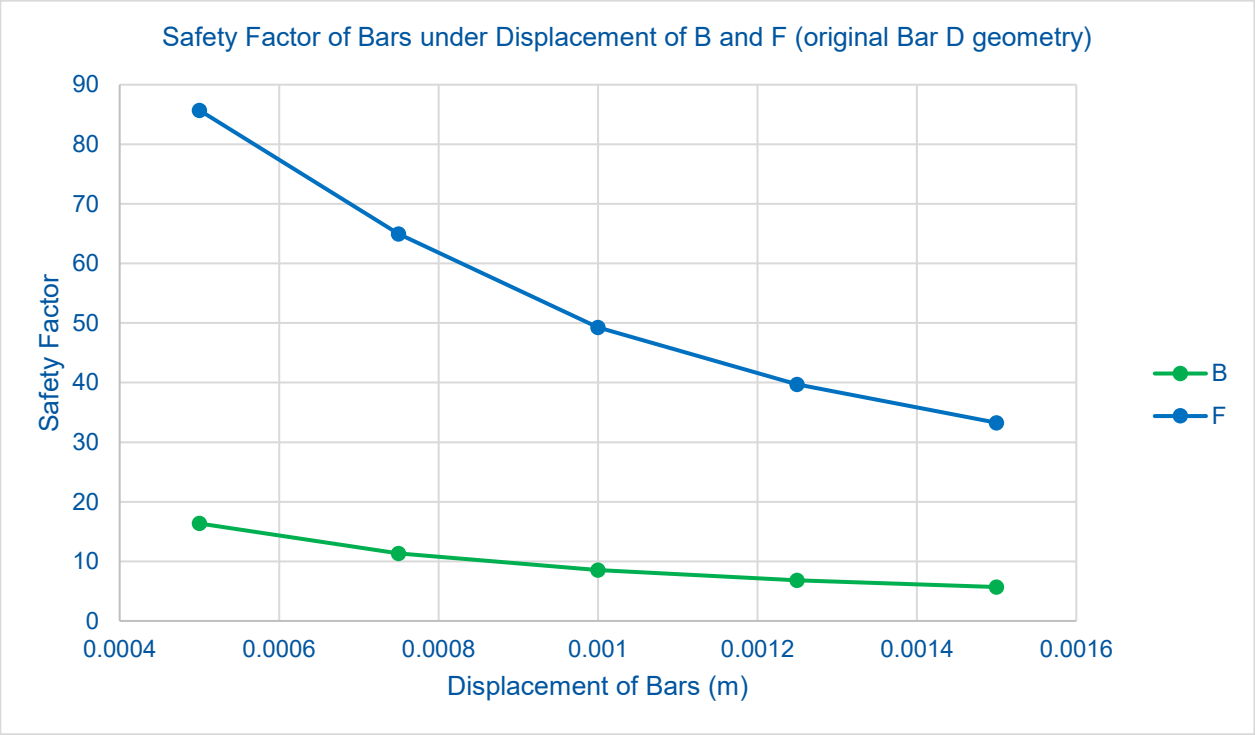

Figure 68: Safety factor of Bars B and F under the displacement of Bars B and F, with original Bar D geometry, bar-sleeve-SAS

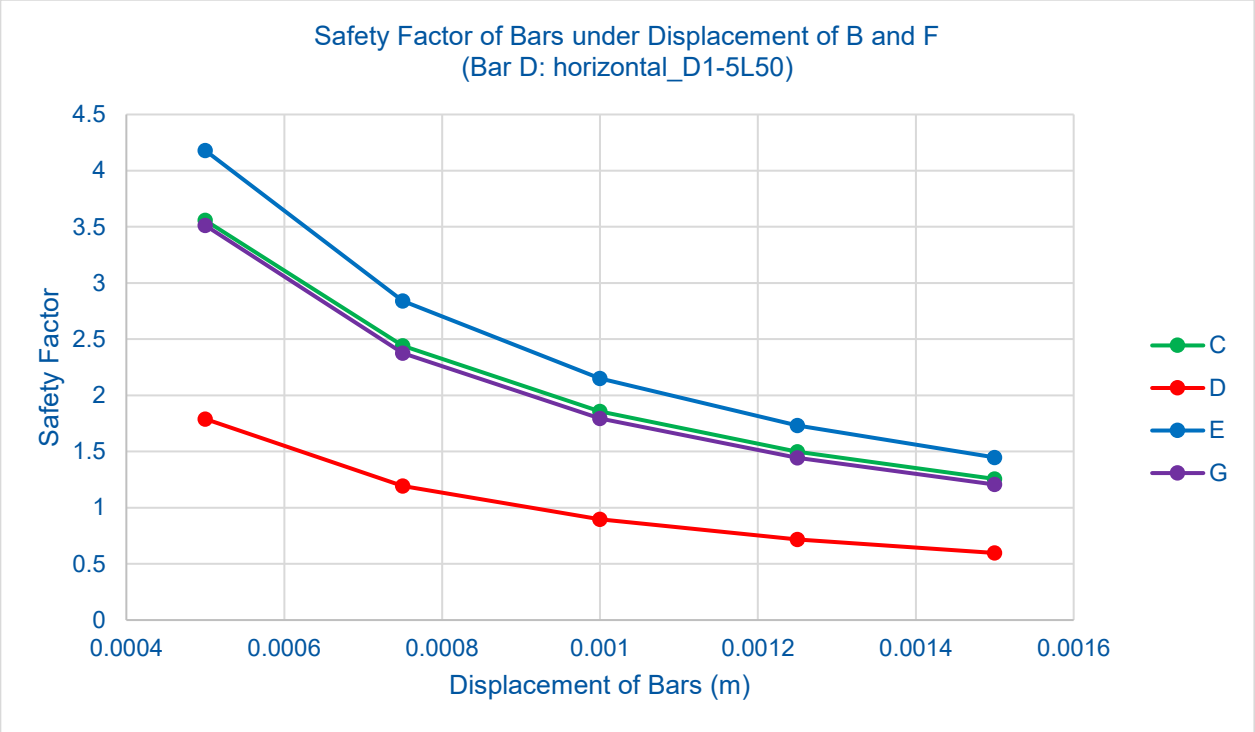

Figure 69: Safety factor of Bars C, D, E, and G under the displacement of Bars B and F, with D1-5L50 for Bar D, bar-sleeve-SAS

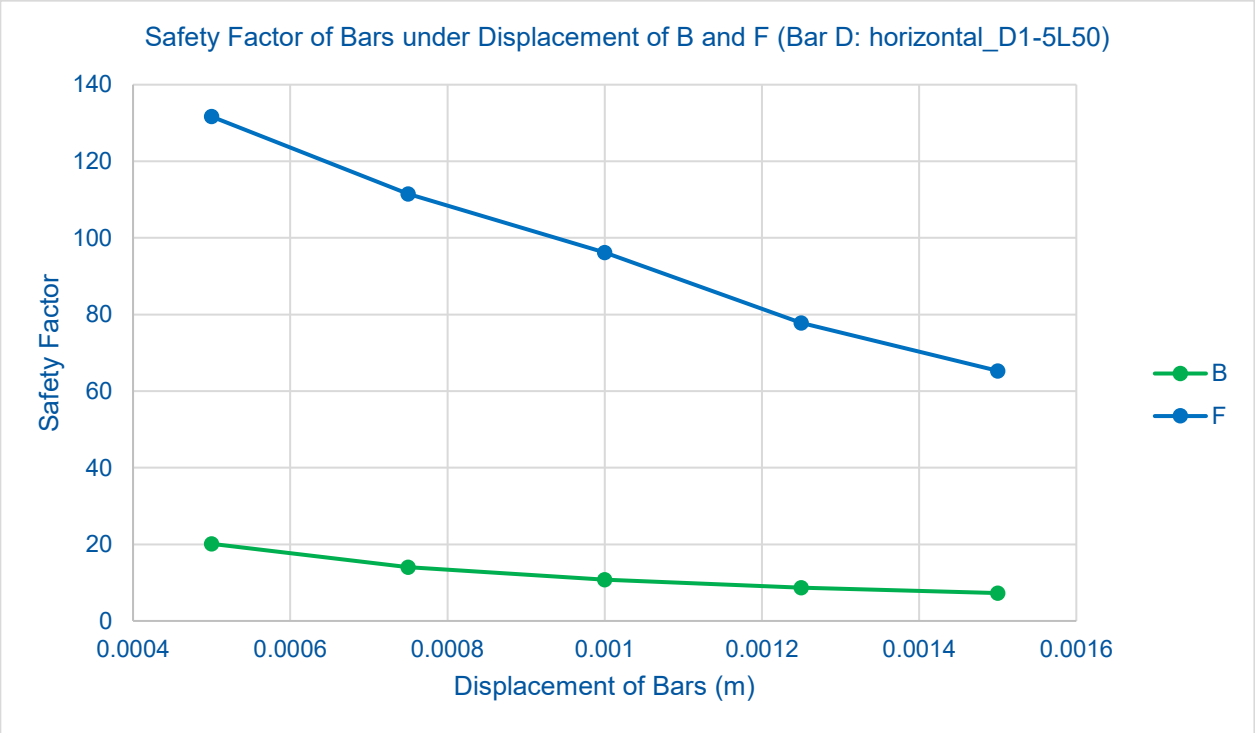

Figure 70: Safety factor of Bars B and F under the displacement of Bars B and F, with D1-5L50 for Bar D, bar-sleeve-SAS

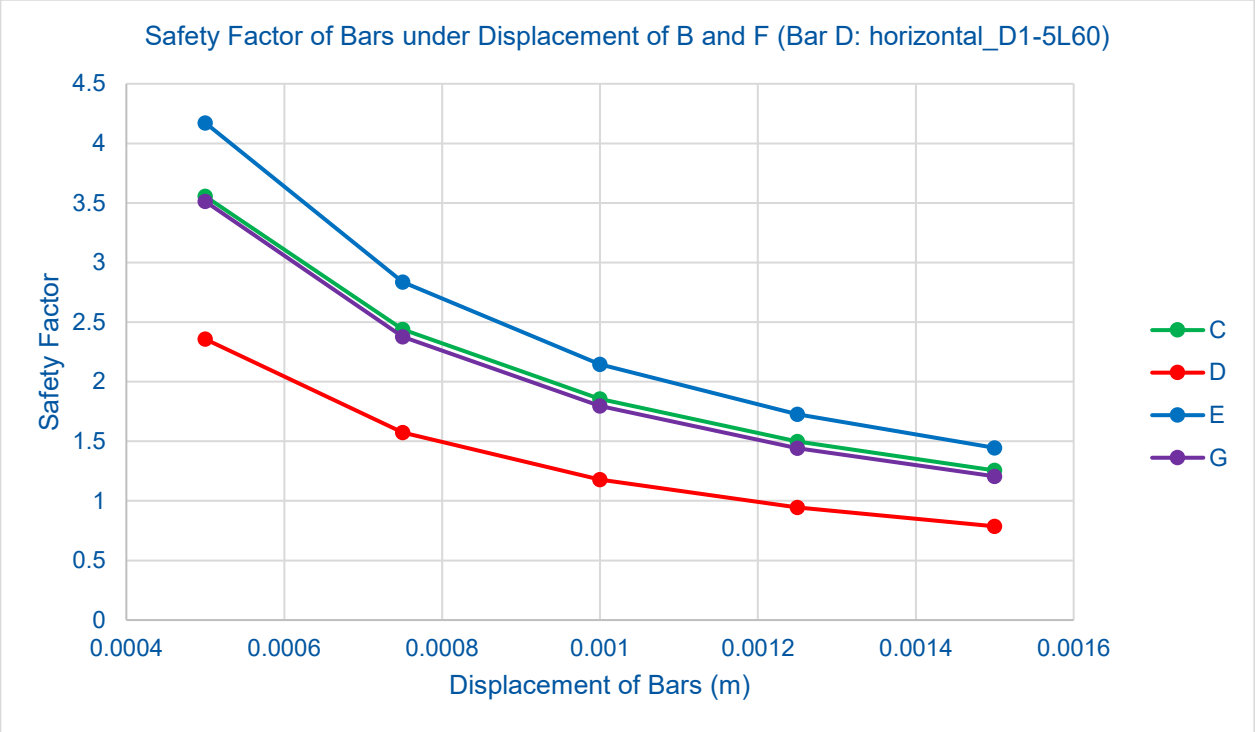

Figure 71: Safety factor of Bars C, D, E, and G under the displacement of Bars B and F, with D1-5L60 for Bar D, bar-sleeve-SAS

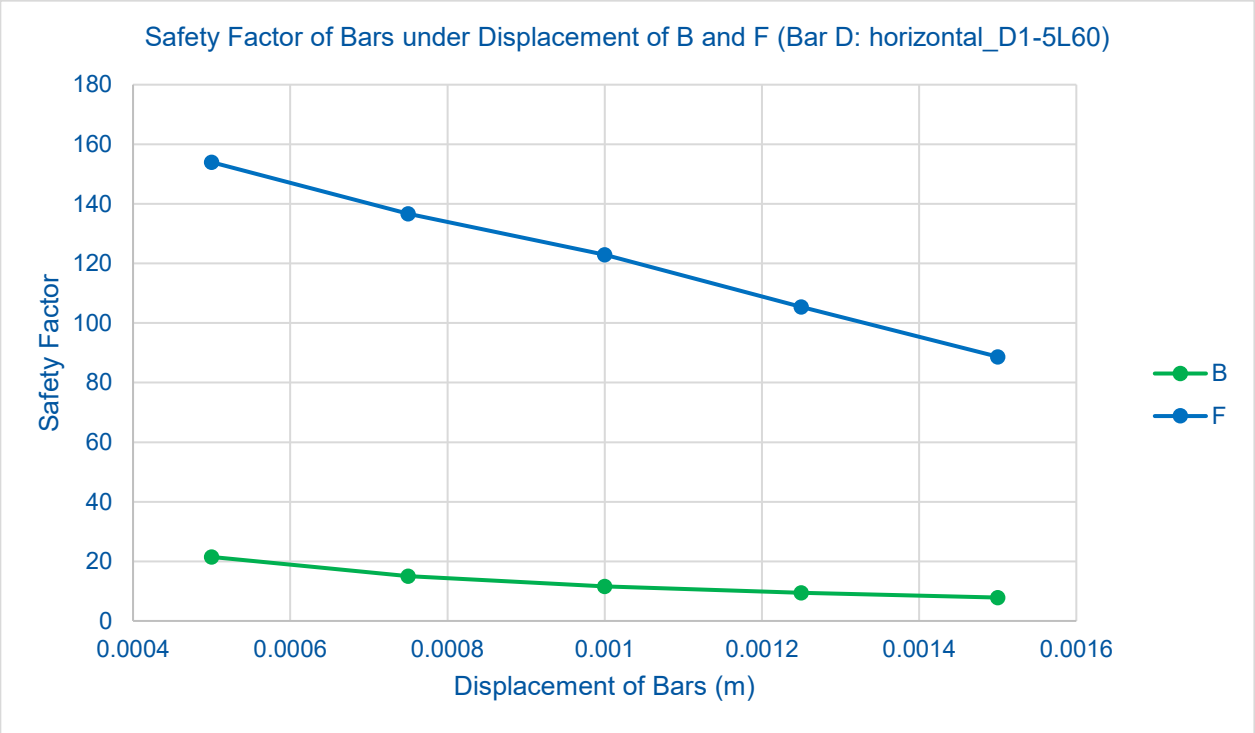

Figure 72: Safety factor of Bars B and F under the displacement of Bars B and F, with D1-5L60 for Bar D, bar-sleeve-SAS

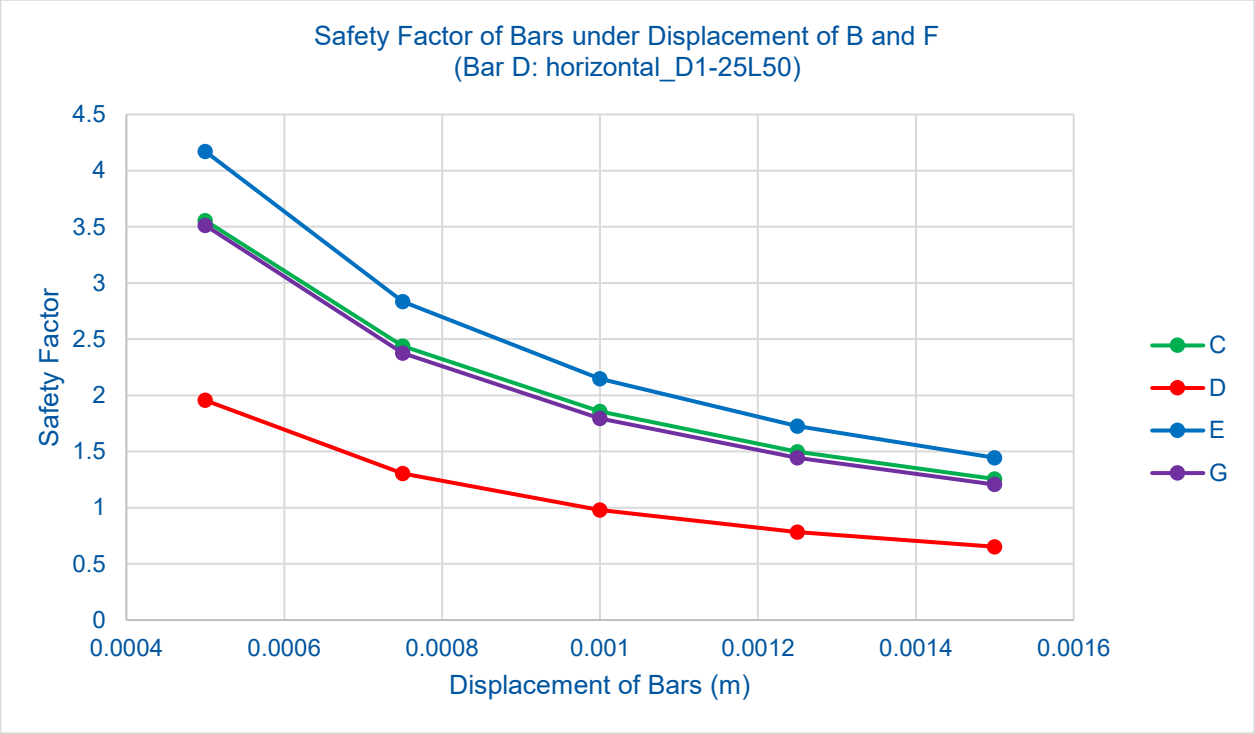

Figure 73: Safety factor of Bars C, D, E, and G under the displacement of Bars B and F, with D1-25L50 for Bar D, bar-sleeve-SAS

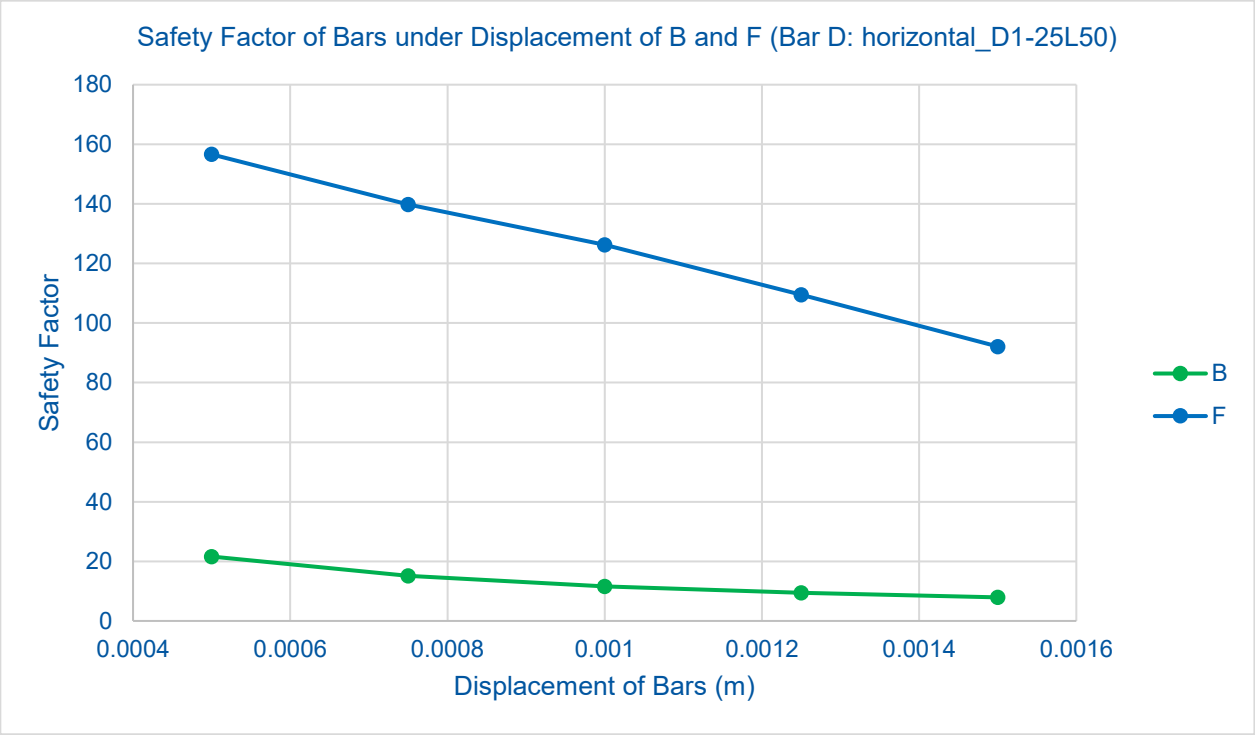

Figure 74: Safety factor of Bars B and F under the displacement of Bars B and F, with D1-25L50 for Bar D, bar-sleeve-SAS

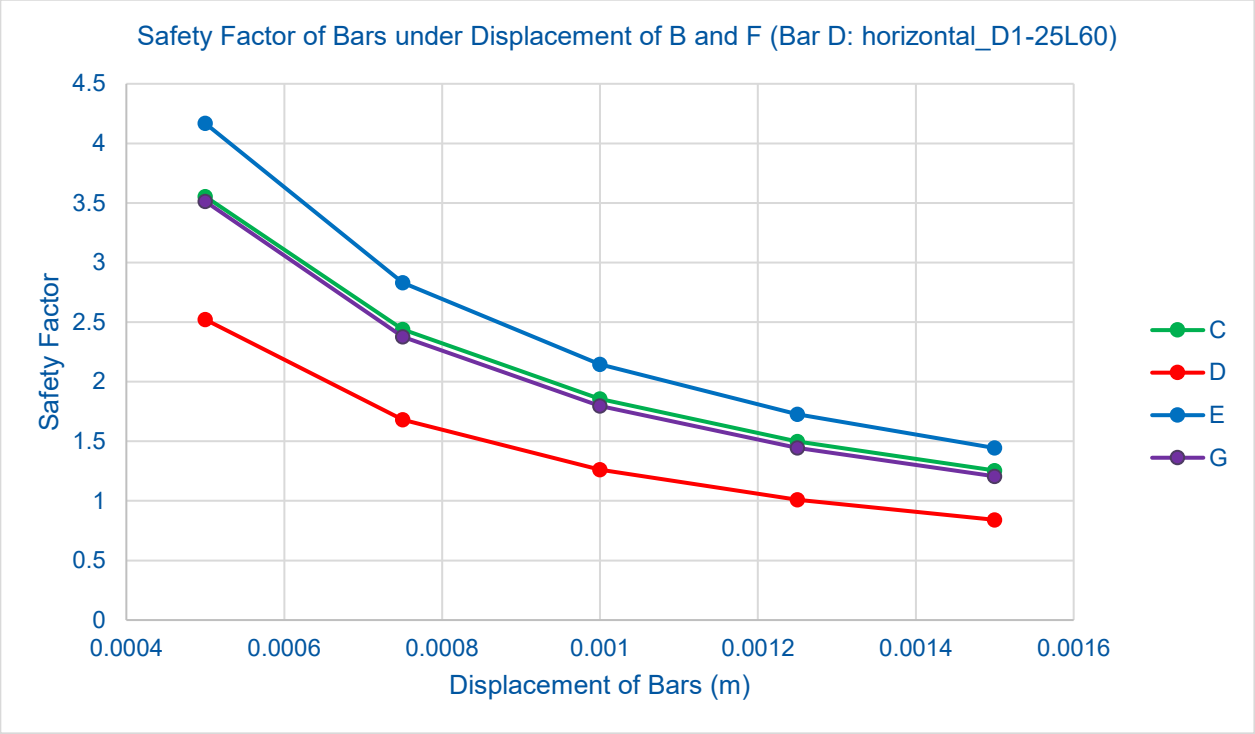

Figure 75: Safety factor of Bars C, D, E, and G under the displacement of Bars B and F, with D1-25L60 for Bar D, bar-sleeve-SAS

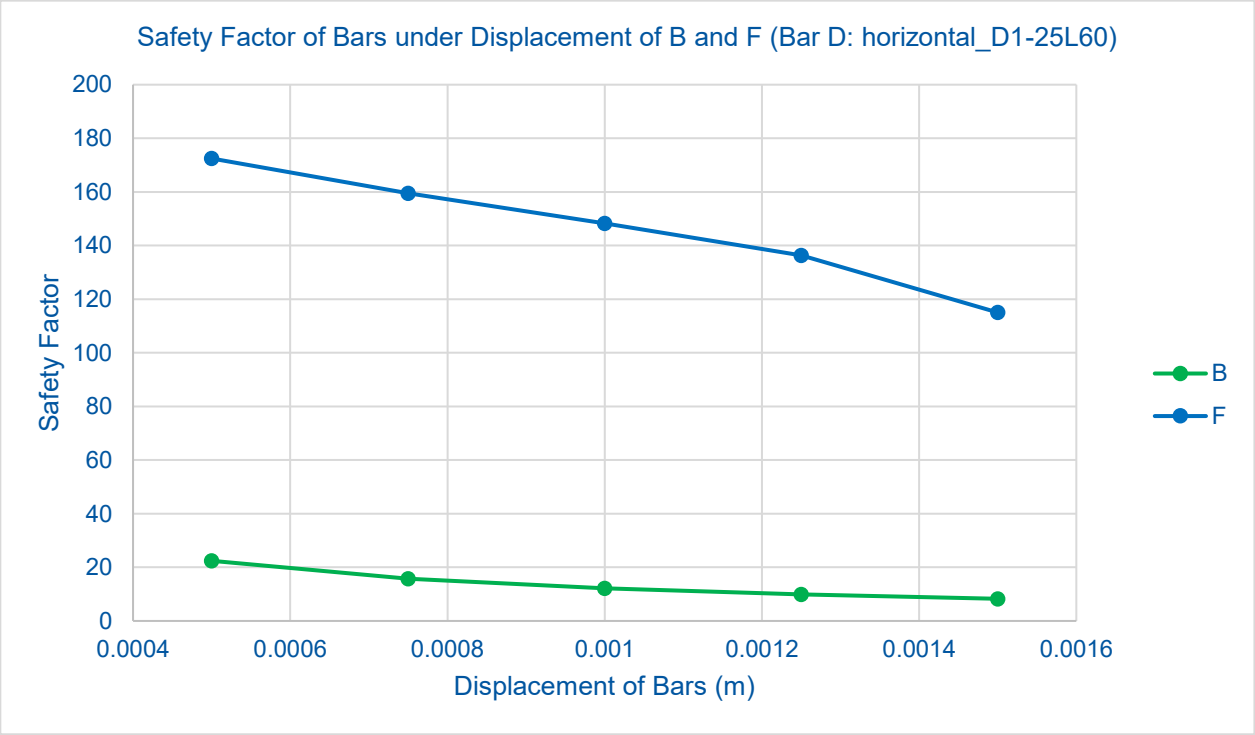

Figure 76: Safety factor of Bars B and F under the displacement of Bars B and F, with D1-25L60 for Bar D, bar-sleeve-SAS

4.3.2.2. Moving Bars C and G

Another case of moving Bars C and G simultaneously was tested, with the different Bar D geometries described in Section 4.3.2.1. The change of the results with the change of Bar D geometries was negligible. Hence the safety factors are only reported with the original Bar D geometry. The highest stress was always observed in Bars B and F.

Figure 77 and Figure 78 shows the safety factor of bars under the displacement of Bars C and G. The curve for Bars B and F are almost overlapping (Figure 78).

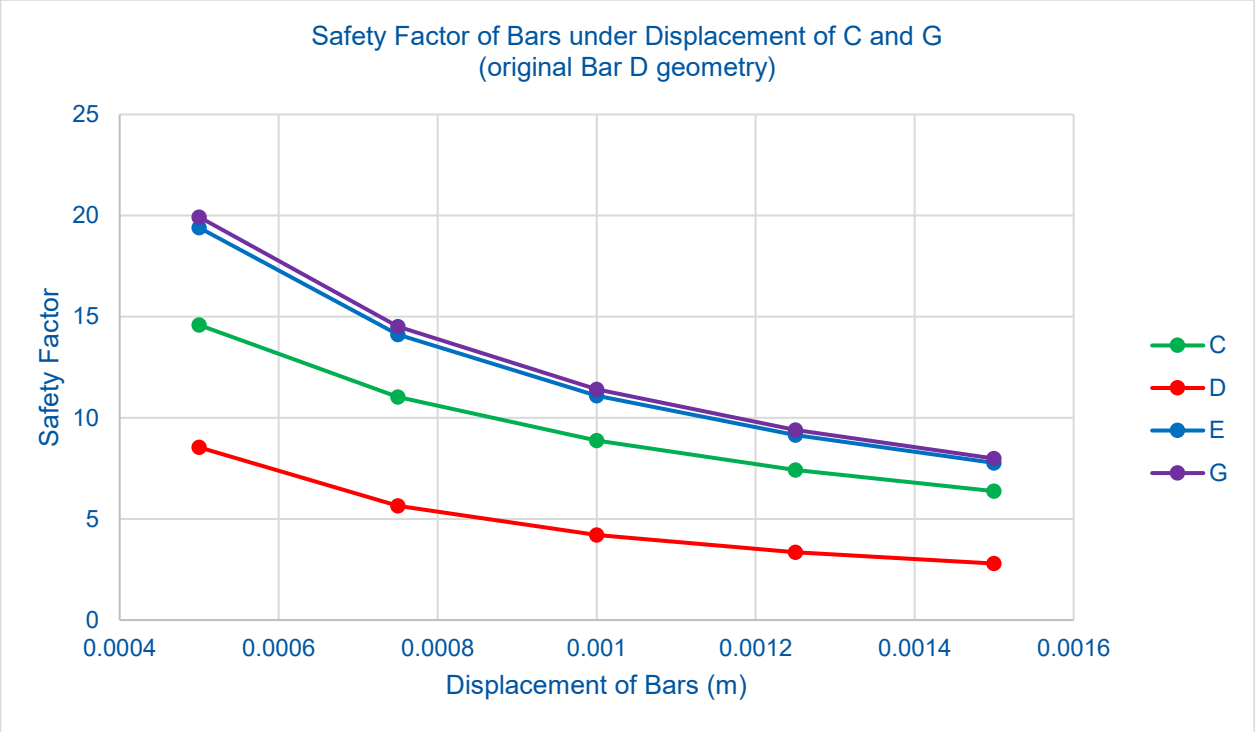

Figure 77: Safety factor of Bars C, D, E and G under the displacement of Bars C and G (original Bar D geometry), bar-sleeve-SAS

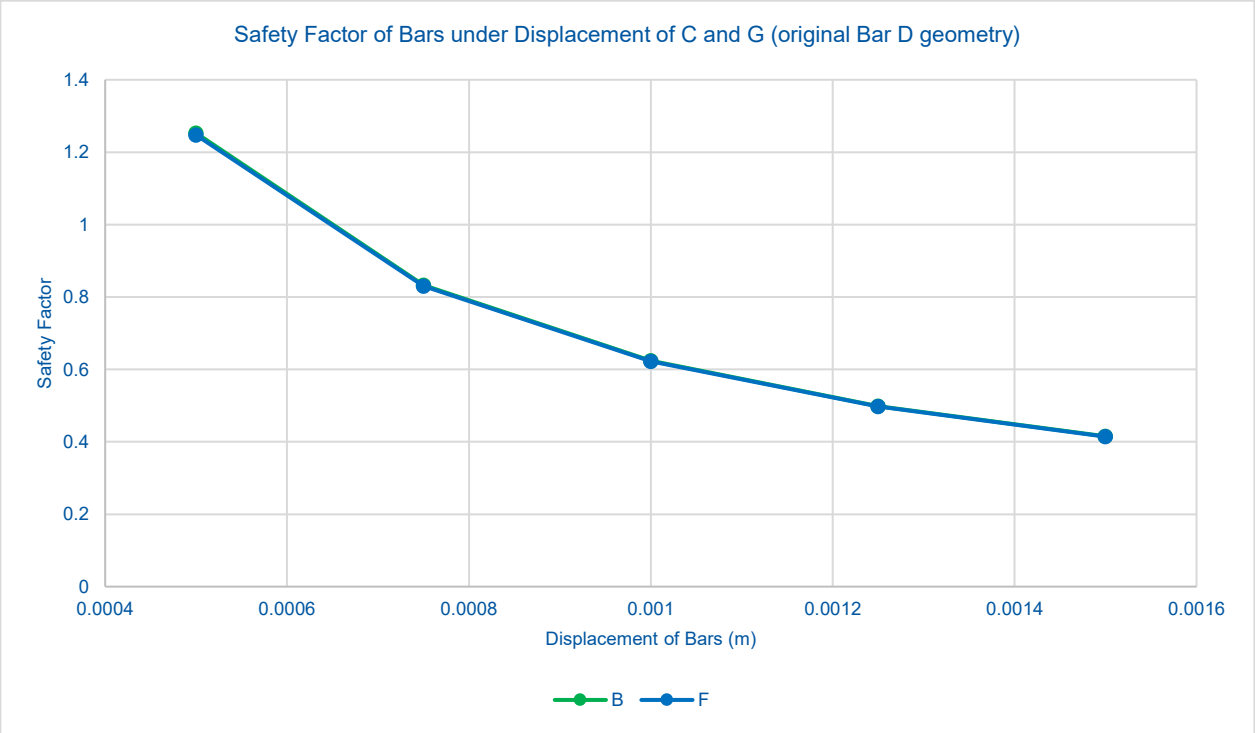

Figure 78: Safety factor of Bars B and F under the displacement of Bars C and G (original Bar D geometry), bar-sleeve-SAS

4.4. Modal analysis

4.4.1. Purpose

The main purpose of a modal analysis is to determine the resonance frequencies of the structure, such that they do not coincide the frequencies of the power supply (e.g. 50 Hz in Switzerland). As long as the resonance frequency stays sufficiently away, the structure is safe from resonating with the power supplies, and mechanical equipment such as motors.

4.4.2. Modifications to the structural simulations

In ANSYS Workbench, the stresses in the structure were first solved (as in Section 4.3.2). The stress and strain were then exported (linked) to the modal solver to solve for the frequencies of modes, i.e. pre-stress modal analysis.

Due to time limitations and issues with the CERN cluster, the mesh size was reduced, and the problem was solved locally. Adaptive mesh refinement was as well turned off, since ANSYS does not allow enabling convergence criteria in linked systems.

In stress-strain simulations of Section 4.3.2, for simplicity, the accelerating structure was set to be of structural steel, with a modified density so that the total mass in the model equalled the actual mass. Here, the material of the accelerating structure was changed to the actual material, copper, for higher accuracy.

4.4.3. Results

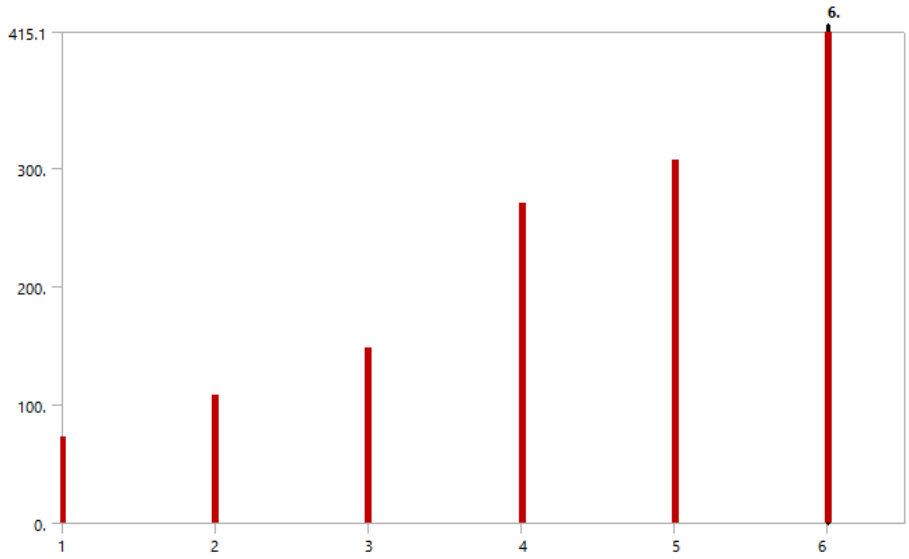

Figure 79: Frequencies reported by ANSYS Mechanical

The same bar naming convention as Section 4.3.2 is used. Similarly, Bars B and F, or Bars C and G, moved simultaneously by the same magnitude in the same direction (into the sleeve). Different geometries were tested for Bar D, as listed in Section 4.3.2.1.

Figure 79 shows an example of how ANSYS Mechanical reports the resonance frequencies. They correspond to the different modes using the original Bar D geometry, with no displacements.

In the range of displacements and geometries considered, all modes had frequencies higher than 70 Hz, safely away from 50 Hz. It was as well found that the displacements (and hence the corresponding stress and strain) of Bars B and F, or Bars C and G, did not significantly change the frequencies. Nevertheless, the following trends were observed:

1. A thinner Bar D lowered the frequency of the lower modes (~ 1st – 3rd mode)
2. A longer Bar D lowered the frequency of the higher modes (~ 4th mode or higher, > 200 Hz)

Section 6.4 in the appendix includes the full results of the modal analysis. Note that at some displacement values of the bars, some of the bars were yielding and were thus plastically deforming. The results might not be accurate since the yielding behaviour of the material was not known.

5. Conclusions

5.1. CFD simulations

This report has presented a complete approach to the steady-state CFD simulations of the two-beam module for its heat dissipation. For heat dissipation through the tunnel wall, a transient model has been determined as necessary and a working model has been presented. This, however, requires better understanding of the operation cycle. The CFD simulations can be further worked on by introducing periodicity and improving convergence behaviour.

5.2. Structural simulations

The results for the stress-strain simulations for the adjustable supports with different dimensions have been reported. For such simulations, it was crucial to fix a stiffness factor, if it was required by the algorithm. The results of these simulations have to be verified with a prototype.

Modal analyses were as well performed, and the resonance frequencies have been presented in this report.

5.3. Other possible cooling approaches and improvements

During the course of the project several other cooling approaches were considered. The approaches in this Section 5.3 are only for the record for the team during discussions rather than solely the first author's original ideas.

The first solution is to insulate the entire accelerating structure. This directly addresses the issue of heat dissipation from the module to air (and perhaps by radiation to the tunnel wall) and confine further the heat dissipation to the running cooling water. However, the main issue remains that however good the insulation is, there is always heat transferred to air. Although that may be significantly reduced, it may still account for something over the length of the entire accelerator, which can be as long as 50 km.

The second proposal is to introduce local cooling. This involves local cooling units between every SAS. The basic idea is to locally remove heat, which can be thought of as an insulation layer made of air. The major issue with this approach is to dimension such cooling units, but one can compare with the cooling requirements of a common consumer desktop PC, which under full load the CPU dissipates approximately 100 W of heat. The other issue with the approach is that none of the cooling units shall fail during the operation of the accelerator. In this regard, maintenance of all the units will also be an issue. In the end, since this is similar to putting an insulation layer of air instead of a solid thermally insulative material, there is always heat transferred to air and the problem described in the first solution still has to be solved.

The third suggestion is to introduce extrusions in the pipes. Currently, 4 straight hollow tubes are cut from each super-accelerating structure for water to flow within. To improve heat transfer performance, fins can be added to increase the area of heat transfer. Such features may not be too difficult to manufacture.

It is worth noting that the all of the above approaches can only aim to reduce the heat dissipation to air – but not eliminate it. In any case, a strategy to tackle heat dissipation to air from the module over tens of kilometres has to be devised.

6. Appendix

6.1. Tunnel cross section

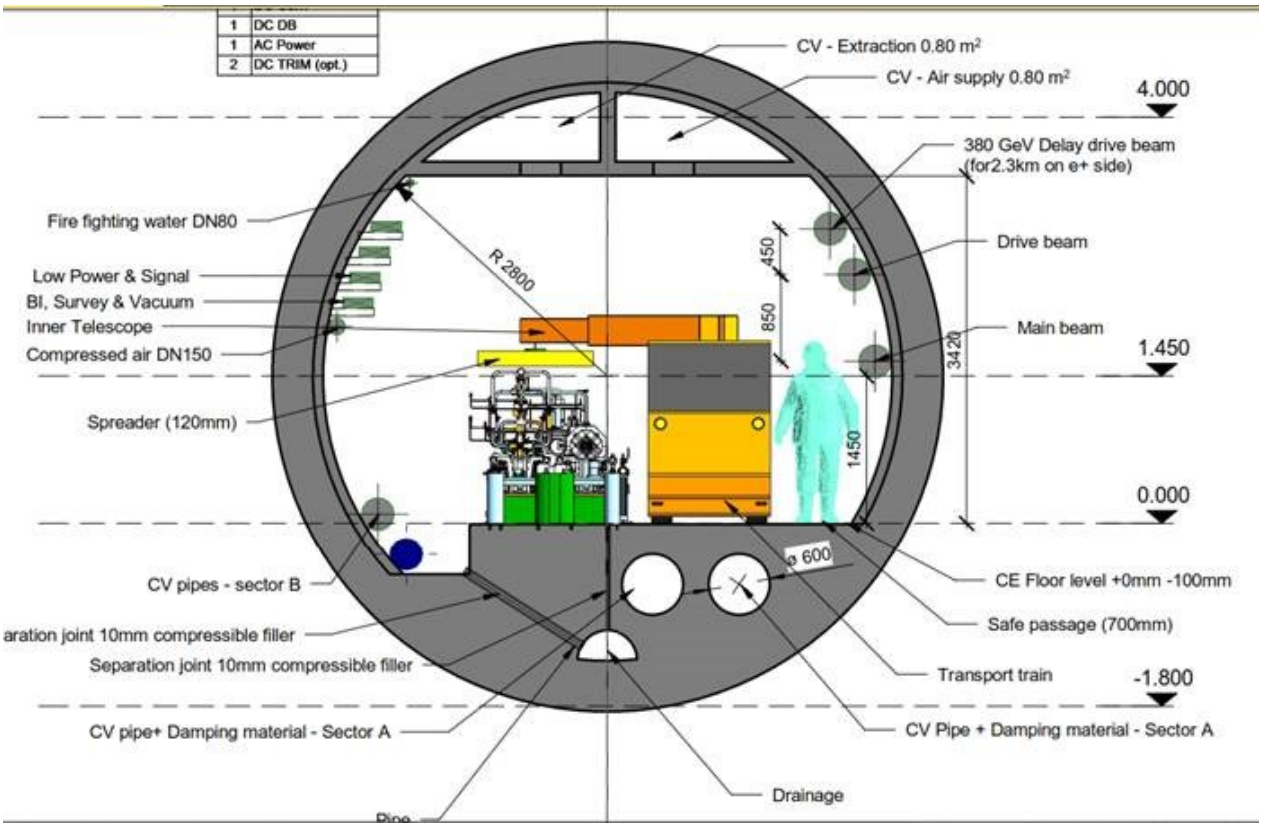

Figure 80: Tunnel cross section (M. J. Stuart, personal communication, January 8, 2018)

6.2. Steady-state approach to the modelling of heat transfer to soil

Refer to

Figure 81. In the following, $T_i = T(r = r_i)$, where $i \in \{1,2,3\}$

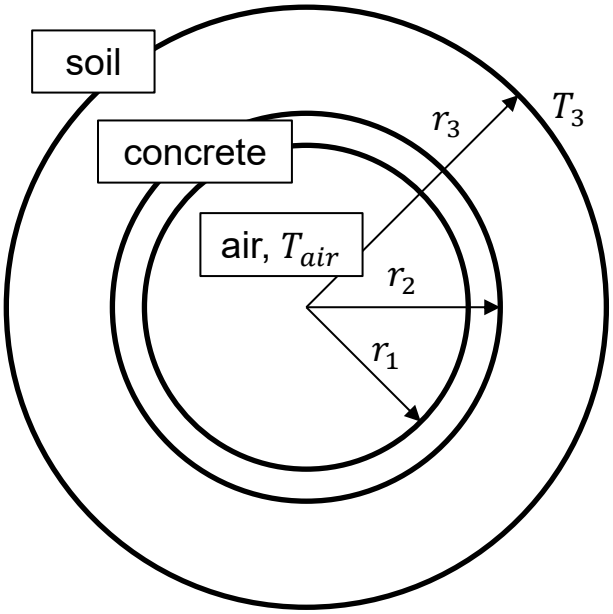

Figure 81: Cross section of the tunnel for the steady-state approach

The governing equation is given by:

$$\frac{1}{r}\frac{d}{dr}\left(r\frac{dT}{dr}\right) = 0$$

The equation is solved for $T(r)$ in $r_1 < r < r_3$.

At r_1, the convection boundary condition is prescribed:

$$q = -k_c\frac{dT}{dr} = h(T_{AIR} - T_1)$$

At r_3, the temperature boundary condition is prescribed:

$$T(r = r_3) = T_3$$

As described in Section 3.8.2.2, the problem of the steady-state approach lies with the artificial assumption of the outer soil boundary at r_3, and that r_3 and T_3 are arbitrary. The problem is not solved since the problem is only transformed to the problem of specifying r_3 and T_3.

An analytical solution to the above equation can easily be found. The temperature at the inner tunnel wall is found to be:

$$T_1 = T_{AIR} + \frac{k_c k_s (T_{AIR} - T_3)}{-k_c k_s + h k_s r_1 \ln(r_1/r_2) + h k_c r_1 \ln(r_2/r_3)}$$

The temperature in the concrete ($r_1 < r < r_2$) is found to be:

$$T = \frac{h(T_1 - T_{AIR}) r_1 \ln(r/r_2)}{k_c} + T_2$$

The temperature in the soil ($r_2 < r < r_3$) is found to be:

$$T = \frac{h(T_1 - T_{AIR}) r_1 \ln(r/r_3)}{k_s} + T_3$$

Note that at the interface between concrete and soil the temperature and the heat fluxes are coupled. The ratio of the thermal conductivity of the two materials determine the ratio of the slope of temperature of the two materials at the interface.

A numerical solution was also obtained with ANSYS Mechanical, using arbitrary tunnel parameters as follows:

Thermal conductivity of concrete, k_c = 0.8 W/(m·K)

Thermal conductivity of soil, k_s = 0.2 W/(m·K)

Convective heat transfer coefficient between air and concrete, h = 7.5 W/(m^2·K)

Inner radius of the tunnel wall, r_1 = 1 m

Outer radius of the tunnel wall, r_2 = 1.2 m

Air temperature, T_{AIR} = 35 °C

“Undisturbed” soil temperature, T_3 = 18 °C

Figure 82 to Figure 84 illustrate some of the results obtained numerically from ANSYS Mechanical and analytically. The numerical and analytical approach were in good match.

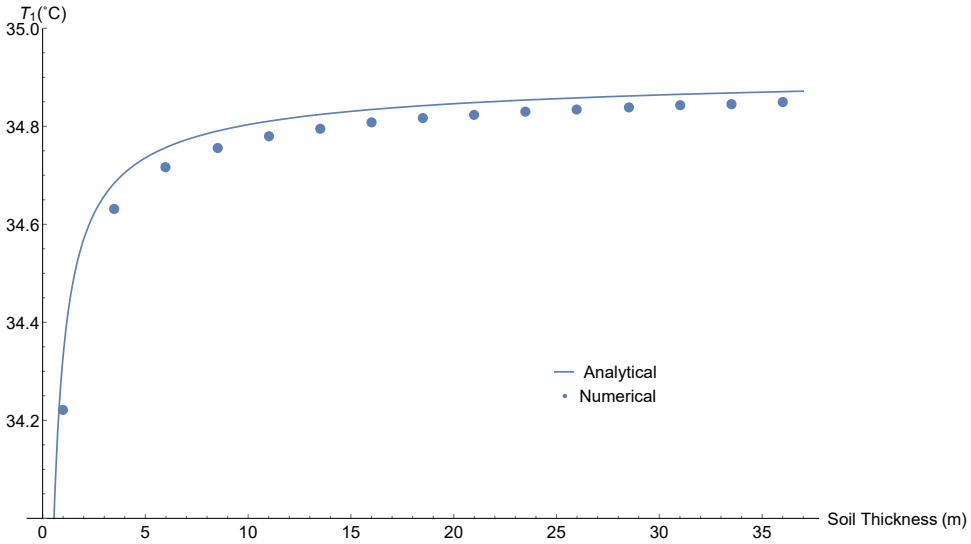

Figure 82: Variation of T_1 with soil thickness $(r_3 - r_2)$

From Figure 82, T_1 approaches T_{AIR} as soil thickness approaches infinity.

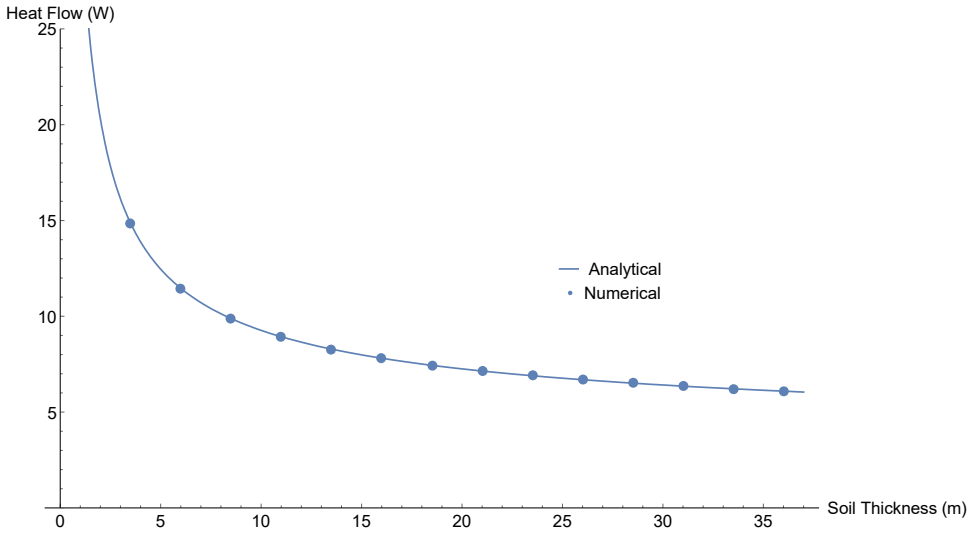

Figure 83: Variation of heat flow in the wall with soil thickness $(r_3 - r_2)$

Figure 83 shows that heat flow (per metre of tunnel) approaches 0 W, as soil thickness approaches infinity.

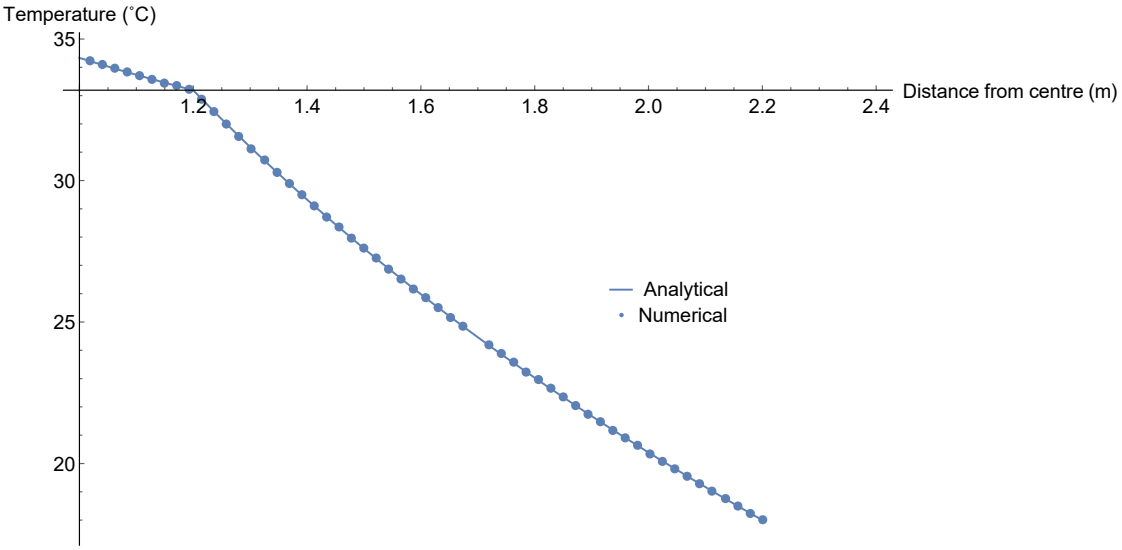

Figure 84: Temperature profile in the concrete and soil layers

Figure 84 shows the temperature profile in the concrete and soil layers. It was obtained using r_3 = 2.2 m, an arbitrary number.

The main point is that from Figure 82 and Figure 83, one can easily observe that the two most important results, the temperature of the wall and the heat flow through the wall depended on the choice of the soil thickness, i.e. how deep the “undisturbed” soil was, under the steady-state and “undisturbed” soil temperature assumptions. Consequently, the temperature profile in Figure 84 as well changed with the soil thickness.

6.3. Material properties of silicon carbide

Silicon carbide Main Beam Type I Sintec

XIII) ANNEX 1

CARBURE DE SILICIUM FRITTE BOOSTEC
BOOSTEC SINTERED SILICON CARBIDE

BOOSTEC INDUSTRIES

CARACTERISTIQUES TYPIQUES * / TYPICAL CHARACTERISTICS *			UNITES / UNITS	
	Silicium libre / Free silicon		% mass./ wt%	0 %
PHYSIQUES / PHYSICAL	Structure cristalline / Crystal structure		—	alpha SiC
	Taille moyenne des cristaux / Mean grain size		10^{-6} m	5
	Porosité totale / Total porosity		% vol. / vol. %	< 3.5 %
	Porosité ouverte / Open porosity		% vol. / vol. %	0 %
	Densité apparente / Apparent bulk density		10^3 kg/m^3	> 3.10
	Densité théorique / theoretical density		10^3 kg/m^3	3.21
THERMIQUES / THERMAL	Coefficient de dilatation linéaire	20-50°C	10^{-6}/°C	4.0
		20-100°C	10^{-6}/°C	4.6
	Coefficient of thermal expansion	20-1400°C	10^{-6}/°C	5.2
	Conductivité thermique à	20°C	W/m.K	180
		500°C	W/m.K	68
	Thermal conductivity at	1000°C	W/m.K	40
	Chaleur spécifique à	20°C	J/kg.K	680
		500°C	J/kg.K	1040
	Specific heat at	1000°C	J/kg.K	1180
	Résistance aux chocs thermiques / Maximum thermal shock		°C	325
MECANIQUES / MECHANICAL	Dureté Vickers (charge 500g) / Vickers hardness (500g load)		GPa	22
	Résistance mécanique (flexion 3pts) à	20°C	MPa	450
		1000°C	MPa	450
	Mechanical strength (3-point bending) at	1400°C	MPa	450
	Module de Weibull / Weibull modulus	à / at 20°C	—	10
	Résistance en compression / Compressive strength		MPa	3900
	Module d'Young / Young's modulus		GPa	420
	Module de cisaillement / Shear modulus		GPa	180
	Coefficient de Poisson / Poisson's ratio		—	0.16
	Ténacité Kic / Kic Toughness	à / at 20°C	MN.m$^{-3/2}$	3.5
ELECTRIQUES / ELECTRICAL	Résistivité électrique / Electrical resistivity		Ohm.m	10^5
	Température limite d'utilisation	sous air / in air	°C	1450
		atm. neutre / inert atm.	°C	1800
	Maximum working temperature			

* *Valeurs informatives données sans garantie de BOOSTEC INDUSTRIES*
* *These properties are typical and should not be considered as specifications*

Figure 85: Properties of SiC (A. Vamvakas, personal communication, October 27, 2017)

6.4. Results from modal analysis

	Original Geometry	horizontal_D1-5L50	horizontal_D1-5L60	horizontal_D1-25L50	horizontal_D1-25L60
Mode	Frequency (Hz)	Frequency (Hz)	Frequency (Hz)	Frequency (Hz)	Frequency (Hz)
1	73.247	71.638	71.545	70.061	69.965
2	108.29	95.534	95.203	89.560	89.335
3	147.95	143.96	143.89	142.78	142.74
4	270.83	270.80	270.82	270.79	226.70
5	306.57	303.02	302.97	301.67	270.82
6	415.10	414.96	303.23	414.86	301.65

Table 13: Modal analysis, no movement of bars

	Original Geometry	horizontal_D1-5L50	horizontal_D1-5L60	horizontal_D1-25L50	horizontal_D1-25L60
Mode	Frequency (Hz)	Frequency (Hz)	Frequency (Hz)	Frequency (Hz)	Frequency (Hz)
1	73.541	72.074	71.858	70.544	70.313
2	108.03	94.989	94.791	88.924	88.860
3	147.65	143.81	143.82	142.70	142.72
4	270.26	270.22	270.24	270.21	227.01
5	305.97	302.49	302.48	301.18	270.23
6	415.97	415.81	303.48	415.71	301.19

Table 14: Modal analysis, Bars B and F move by 0.5 mm

	Original Geometry	horizontal_D1-5L50	horizontal_D1-5L60	horizontal_D1-25L50	horizontal_D1-25L60
Mode	Frequency (Hz)	Frequency (Hz)	Frequency (Hz)	Frequency (Hz)	Frequency (Hz)
1	73.676	72.278	72.005	70.771	70.475
2	107.90	94.696	94.573	88.582	88.608
3	147.50	143.73	143.78	142.65	142.70
4	269.95	269.91	269.93	269.91	227.36
5	305.65	302.21	302.22	300.91	269.93
6	416.40	416.24	303.75	416.12	300.94

Table 15: Modal analysis, Bars B and F move by 0.75 mm

	Original Geometry	horizontal_D1-5L50	horizontal_D1-5L60	horizontal_D1-25L50	horizontal_D1-25L60
Mode	Frequency (Hz)	Frequency (Hz)	Frequency (Hz)	Frequency (Hz)	Frequency (Hz)
1	73.803	72.473	72.145	70.988	70.632
2	107.75	94.388	94.345	88.224	88.346
3	147.33	143.64	143.73	142.59	142.67
4	269.63	269.60	269.61	269.59	227.79
5	305.31	301.91	301.93	300.62	269.60
6	416.82	416.65	304.08	416.53	300.67

Table 16: Modal analysis, Bars B and F move by 1 mm

	Original Geometry	horizontal_D1-5L50	horizontal_D1-5L60	horizontal_D1-25L50	horizontal_D1-25L60
Mode	Frequency (Hz)	Frequency (Hz)	Frequency (Hz)	Frequency (Hz)	Frequency (Hz)
1	73.921	72.658	72.278	71.195	70.781
2	107.60	94.068	94.109	87.850	88.073
3	147.16	143.54	143.67	142.53	142.64
4	269.30	269.26	269.28	269.25	228.35
5	304.96	301.59	301.64	300.33	269.27
6	417.23	417.05	304.49	416.93	300.39

Table 17: Modal analysis, Bars B and F move by 1.25 mm

	Original Geometry	horizontal_D1-5L50	horizontal_D1-5L60	horizontal_D1-25L50	horizontal_D1-25L60
Mode	Frequency (Hz)	Frequency (Hz)	Frequency (Hz)	Frequency (Hz)	Frequency (Hz)
1	74.031	72.834	72.405	71.393	70.923
2	107.45	93.734	93.865	87.461	87.791
3	146.99	143.44	143.61	142.46	142.60
4	268.96	268.92	268.93	268.91	229.07
5	304.60	301.26	301.33	300.01	268.92
6	411.71	417.45	305.00	417.33	300.09

Table 18: Modal analysis, Bars B and F move by 1.5 mm

	Original Geometry	horizontal_D1-5L50	horizontal_D1-5L60	horizontal_D1-25L50	horizontal_D1-25L60
Mode	Frequency (Hz)	Frequency (Hz)	Frequency (Hz)	Frequency (Hz)	Frequency (Hz)
1	73.754	72.062	71.967	70.398	70.299
2	108.53	95.811	95.470	89.907	89.676
3	148.31	144.35	144.28	143.18	143.15
4	270.26	270.22	270.25	270.22	227.97
5	306.43	302.85	302.80	301.49	270.24
6	414.75	414.61	303.20	414.51	301.46

Table 19: Modal analysis, Bars C and G move by 0.5 mm

	Original Geometry	horizontal_D1-5L50	horizontal_D1-5L60	horizontal_D1-25L50	horizontal_D1-25L60
Mode	Frequency (Hz)	Frequency (Hz)	Frequency (Hz)	Frequency (Hz)	Frequency (Hz)
1	73.991	72.255	72.161	70.549	70.450
2	108.65	95.955	95.608	90.085	89.850
3	148.48	144.54	144.47	143.37	143.34
4	269.96	269.93	269.95	269.92	228.39
5	306.37	302.78	302.72	301.41	269.95
6	414.52	414.38	303.33	414.28	301.38

Table 20: Modal analysis, Bars C and G move by 0.75 mm

	Original Geometry	horizontal_D1-5L50	horizontal_D1-5L60	horizontal_D1-25L50	horizontal_D1-25L60
Mode	Frequency (Hz)	Frequency (Hz)	Frequency (Hz)	Frequency (Hz)	Frequency (Hz)
1	74.216	72.437	72.343	70.687	70.589
2	108.77	96.101	95.749	90.266	90.027
3	148.65	144.71	144.65	143.55	143.52
4	269.67	269.64	269.66	269.63	228.82
5	306.32	302.71	302.65	301.34	269.65
6	414.27	414.13	303.56	414.01	301.31

Table 21: Modal analysis, Bars C and G move by 1 mm

	Original Geometry	horizontal_D1-5L50	horizontal_D1-5L60	horizontal_D1-25L50	horizontal_D1-25L60
Mode	**Frequency (Hz)**	**Frequency (Hz)**	**Frequency (Hz)**	**Frequency (Hz)**	**Frequency (Hz)**
1	74.430	72.606	72.514	70.814	70.718
2	108.90	96.251	95.892	90.450	90.205
3	148.80	144.88	144.82	143.73	143.69
4	269.37	269.33	269.36	269.33	229.04
5	306.28	302.66	302.59	301.28	269.35
6	413.98	413.84	303.86	413.73	301.24

Table 22: Modal analysis, Bars C and G move by 1.25 mm

	Original Geometry	horizontal_D1-5L50	horizontal_D1-5L60	horizontal_D1-25L50	horizontal_D1-25L60
Mode	**Frequency (Hz)**	**Frequency (Hz)**	**Frequency (Hz)**	**Frequency (Hz)**	**Frequency (Hz)**
1	74.631	72.761	72.672	70.929	70.835
2	109.03	96.404	96.038	90.636	90.387
3	148.96	145.05	144.98	143.89	143.86
4	269.06	269.03	269.05	269.02	229.40
5	306.24	302.61	302.53	301.22	269.04
6	413.66	413.52	304.21	413.40	301.18

Table 23: Modal analysis, Bars C and G move by 1.5 mm

6.5. Borehole records

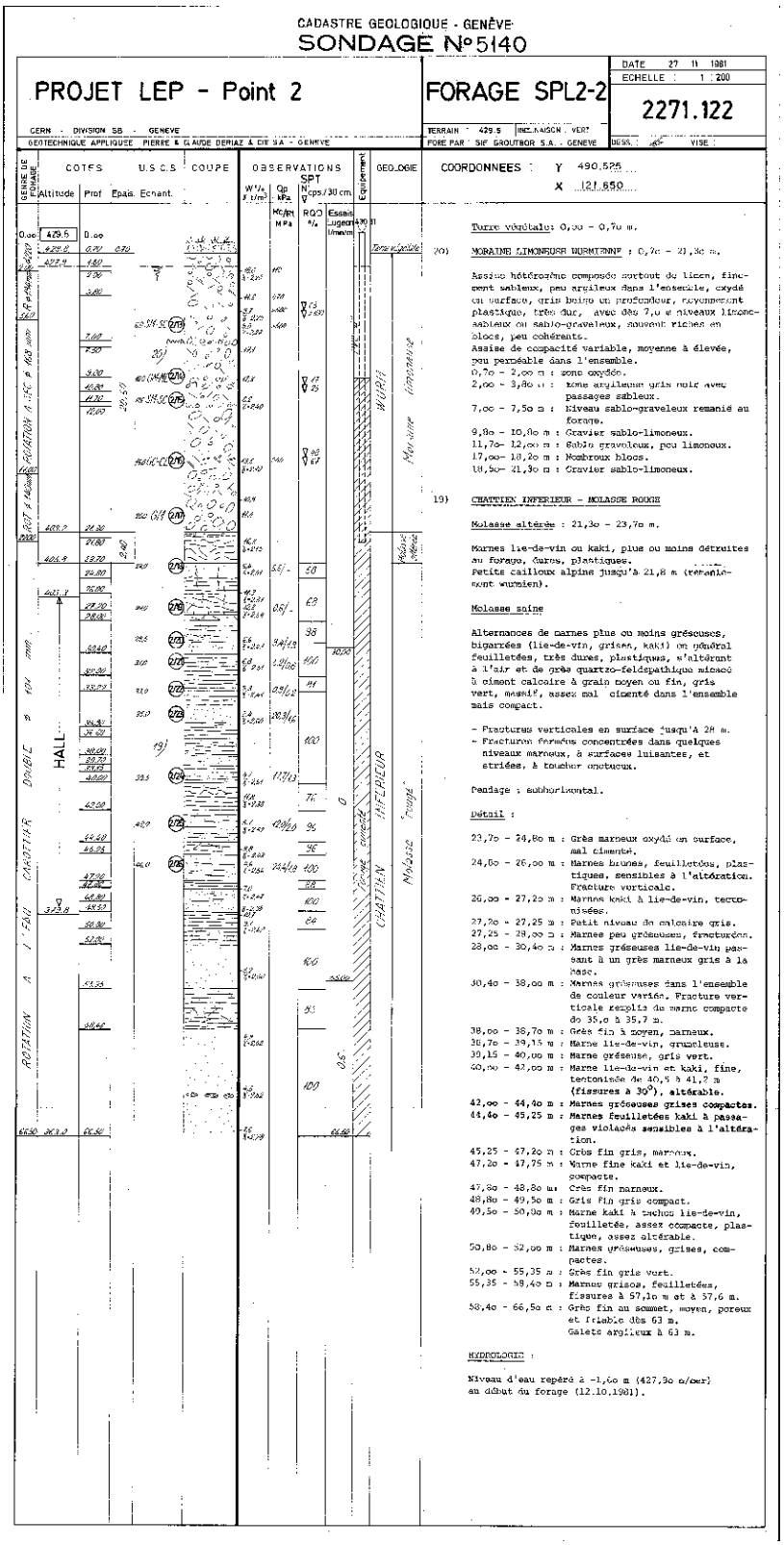

Figure 86: Borehole 5140 (M. J. Stuart, personal communication, November 28, 2017)

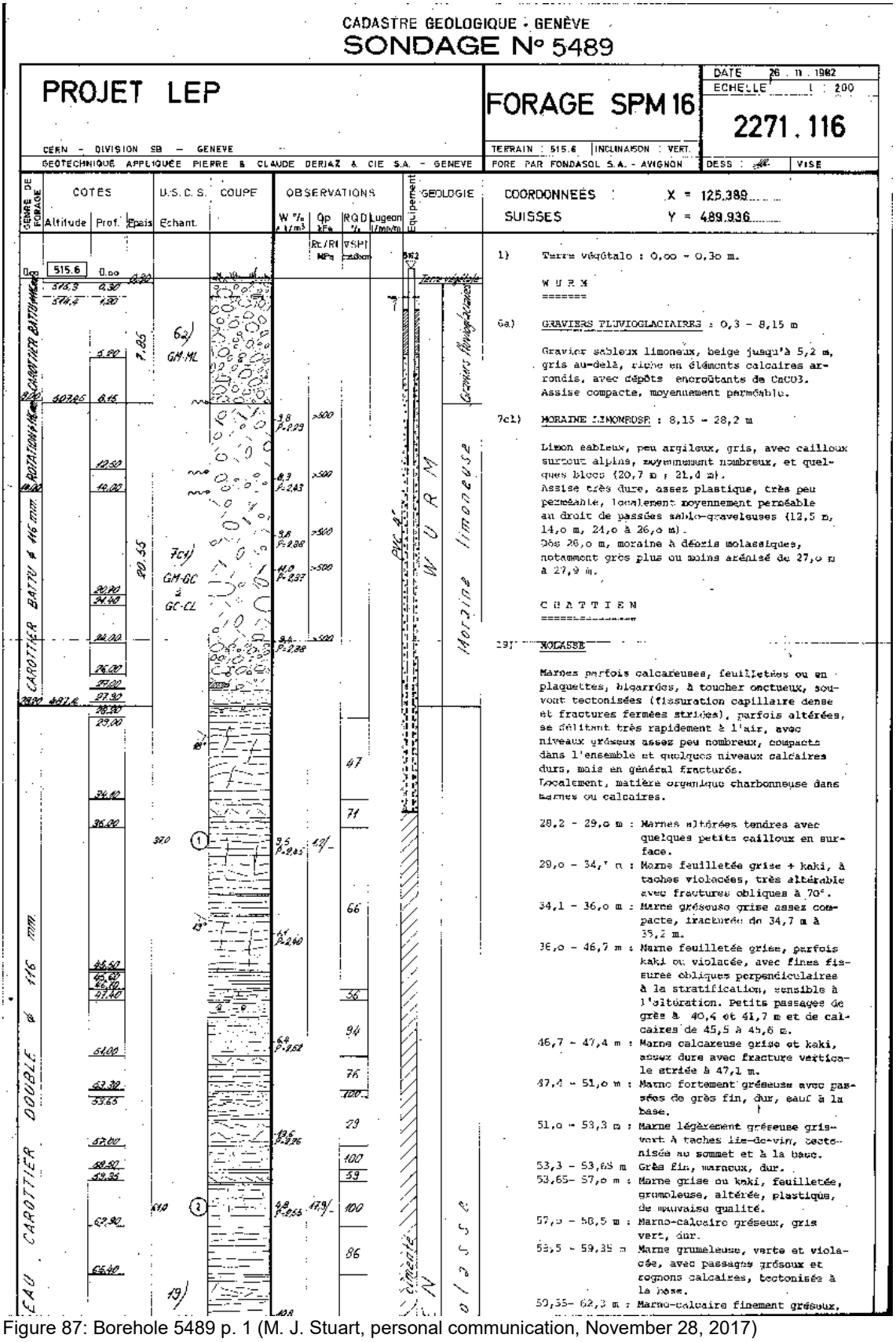

Figure 87: Borehole 5489 p. 1 (M. J. Stuart, personal communication, November 28, 2017)

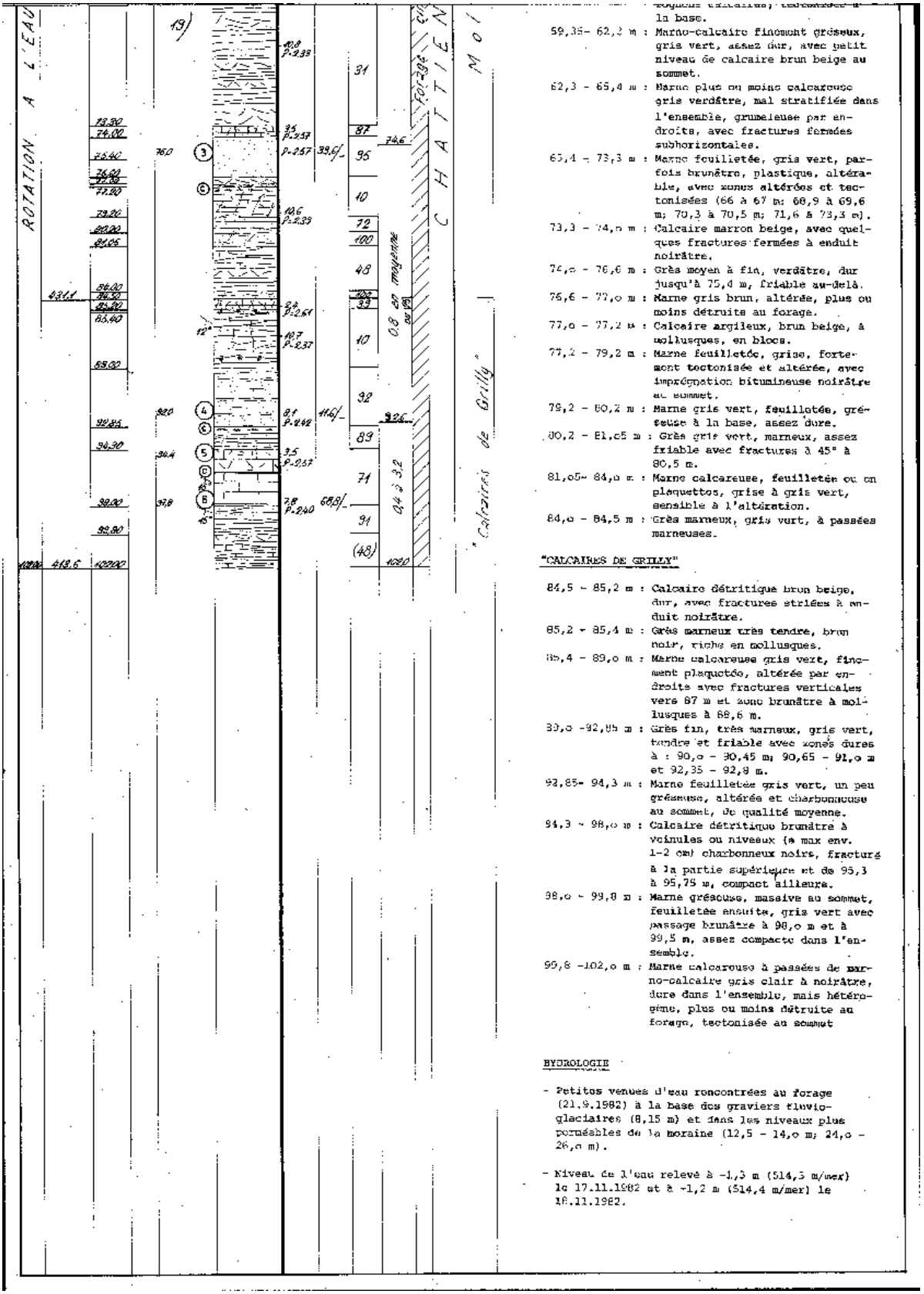

la base.

59,35 - 62,2 m : Marno-calcaire finement gréseux, gris vert, assez dur, avec petit niveau de calcaire brun beige au sommet.

62,2 - 65,4 m : Marne plus ou moins calcareuse gris verdâtre, mal stratifiée dans l'ensemble, grumeleuse par endroits, avec fractures fermées subhorizontales.

65,4 - 73,3 m : Marne feuilletée, gris vert, parfois brunâtre, plastique, altérable, avec zones altérées et tectonisées (66 à 67 m; 68,9 à 69,6 m; 70,3 à 70,5 m; 71,6 à 73,3 m).

73,3 - 74,0 m : Calcaire marron beige, avec quelques fractures fermées à enduit noirâtre.

74,0 - 76,6 m : Grès moyen à fin, verdâtre, dur jusqu'à 75,4 m, friable au-delà.

76,6 - 77,0 m : Marne gris brun, altérée, plus ou moins détruite au forage.

77,0 - 77,2 m : Calcaire argileux, brun beige, à mollusques, en blocs.

77,2 - 79,2 m : Marne feuilletée, grise, fortement tectonisée et altérée, avec imprégnation bitumineuse noirâtre au sommet.

79,2 - 80,2 m : Marne gris vert, feuilletée, gréseuse à la base, assez dure.

80,2 - 81,05 m : Grès gris vert, marneux, assez friable avec fractures à 45° à 80,5 m.

81,05 - 84,0 m : Marne calcareuse, feuilletée ou en plaquettes, grise à gris vert, sensible à l'altération.

84,0 - 84,5 m : Grès marneux, gris vert, à passées marneuses.

"CALCAIRES DE GRILLY"

84,5 - 85,2 m : Calcaire détritique brun beige, dur, avec fractures striées à enduit noirâtre.

85,2 - 85,4 m : Grès marneux très tendre, brun noir, riche en mollusques.

85,4 - 89,0 m : Marne calcareuse gris vert, finement plaquetée, altérée par endroits avec fractures verticales vers 87 m et zone brunâtre à mollusques à 88,6 m.

89,0 - 92,85 m : Grès fin, très marneux, gris vert, tendre et friable avec zones dures à : 90,0 - 90,45 m; 90,65 - 91,0 m et 92,35 - 92,8 m.

92,85 - 94,3 m : Marne feuilletée gris vert, un peu gréseuse, altérée et charbonneuse au sommet, de qualité moyenne.

94,3 - 98,0 m : Calcaire détritique brunâtre à veinules ou niveaux (à max env. 1-2 cm) charbonneux noirs, fracturé à la partie supérieure et de 95,3 à 95,75 m, compact ailleurs.

98,0 - 99,8 m : Marne gréseuse, massive au sommet, feuilletée ensuite, gris vert avec passage brunâtre à 98,0 m et à 99,5 m, assez compacte dans l'ensemble.

99,8 - 102,0 m : Marne calcareuse à passées de marno-calcaire gris clair à noirâtre, dure dans l'ensemble, mais hétérogène, plus ou moins détruite au forage, tectonisée au sommet

HYDROLOGIE

- Petites venues d'eau rencontrées au forage (21.9.1982) à la base des graviers fluvio-glaciaires (8,15 m) et dans les niveaux plus perméables de la moraine (12,5 - 14,0 m; 24,0 - 26,0 m).

- Niveau de l'eau relevé à -1,3 m (514,3 m/mer) le 17.11.1982 et à -1,2 m (514,4 m/mer) le 18.11.1982.

Figure 88: Borehole 5489 p. 2 (M. J. Stuart, personal communication, November 28, 2017)

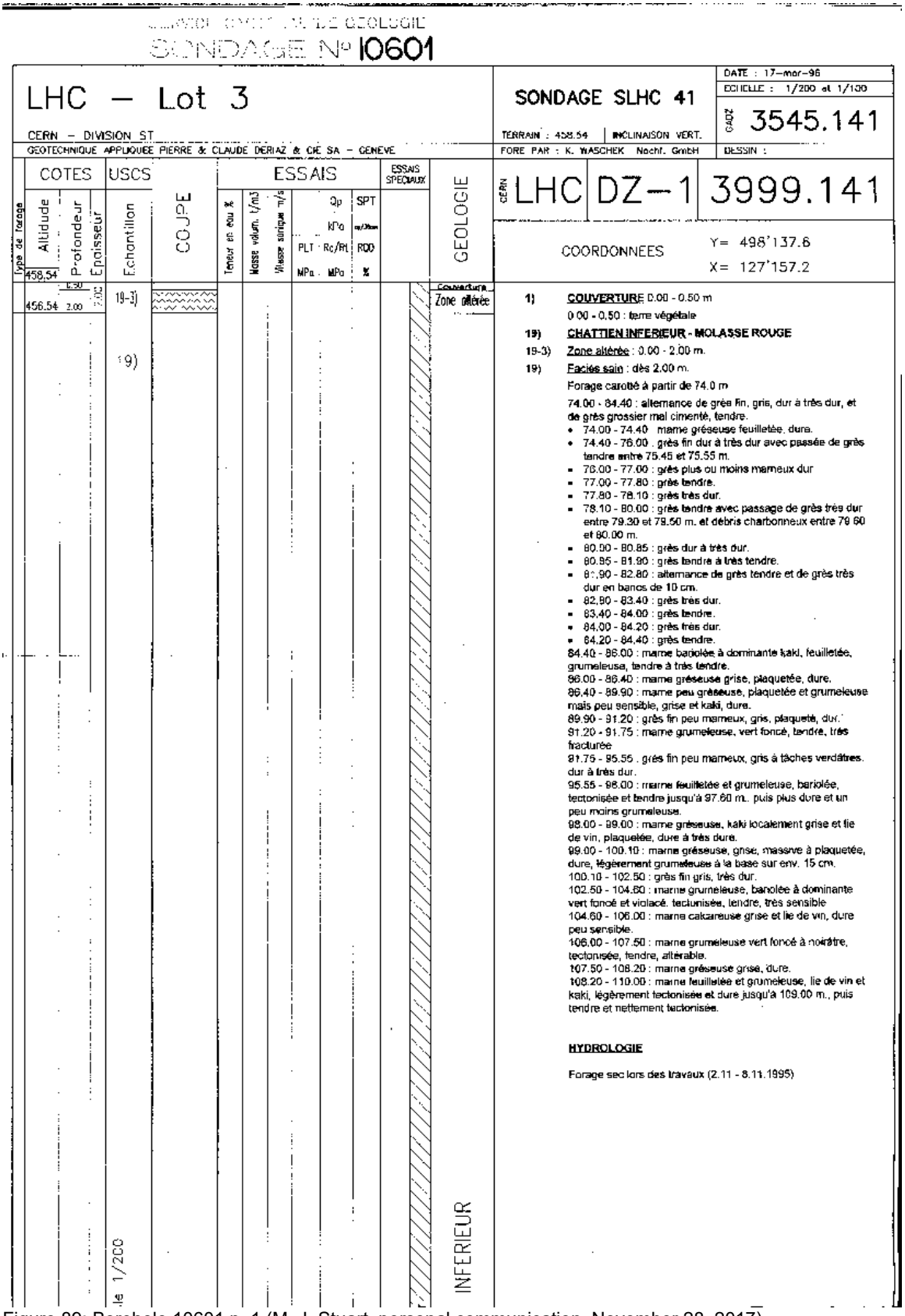

SONDAGE N° 10601

LHC — Lot 3

CERN — DIVISION ST

GEOTECHNIQUE APPLIQUEE PIERRE & CLAUDE DERIAZ & CIE SA — GENEVE

SONDAGE SLHC 41

TERRAIN : 458.54 | INCLINAISON VERT.

FORE PAR : K. WASCHEK Nachf. GmbH

DATE : 17-mar-96

ECHELLE : 1/200 et 1/100

CADZ 3545.141

DESSIN :

CERN LHC DZ-1 3999.141

COORDONNEES Y= 498'137.6 X= 127'157.2

COTES (Altitude, Profondeur, Epaisseur) | USCS (Echantillon) | COUPE | ESSAIS (Teneur en eau %, Masse volum. t/m3, Vitesse suisque m/s, Qp kPa, PLT : Rc/Rt MPa, SPT, RQD %) | ESSAIS SPECIAUX | GEOLOGIE

458.54

456.54 2.00

19-3)

19)

Couverture

Zone altérée

INFERIEUR

1) **COUVERTURE** 0.00 - 0.50 m

0.00 - 0.50 : terre végétale

19) **CHATTIEN INFERIEUR - MOLASSE ROUGE**

19-3) Zone altérée : 0.00 - 2.00 m.

19) Faciès sain : dès 2.00 m.

Forage carotté à partir de 74.0 m

74.00 - 84.40 : alternance de grès fin, gris, dur à très dur, et de grès grossier mal cimenté, tendre.

- 74.00 - 74.40 marne gréseuse feuilletée, dure.
- 74.40 - 76.00 . grès fin dur à très dur avec passée de grès tendre entre 75.45 et 75.55 m.
- 76.00 - 77.00 : grès plus ou moins marneux dur
- 77.00 - 77.80 : grès tendre.
- 77.80 - 78.10 : grès très dur.
- 78.10 - 80.00 : grès tendre avec passage de grès très dur entre 79.30 et 79.50 m. et débris charbonneux entre 79.60 et 80.00 m.
- 80.00 - 80.85 : grès dur à très dur.
- 80.85 - 81.90 : grès tendre à très tendre.
- 81.90 - 82.80 : alternance de grès tendre et de grès très dur en bancs de 10 cm.
- 82.80 - 83.40 : grès très dur.
- 83.40 - 84.00 : grès tendre.
- 84.00 - 84.20 : grès très dur.
- 84.20 - 84.40 : grès tendre.

84.40 - 86.00 : marne bariolée à dominante kaki, feuilletée, grumeleuse, tendre à très tendre.
86.00 - 86.40 : marne gréseuse grise, plaquetée, dure.
86.40 - 89.90 : marne peu gréseuse, plaquetée et grumeleuse mais peu sensible, grise et kaki, dure.
89.90 - 91.20 : grès fin peu marneux, gris, plaqueté, dur.
91.20 - 91.75 : marne grumeleuse, vert foncé, tendre, très fracturée
91.75 - 95.55 . grès fin peu marneux, gris à tâches verdâtres. dur à très dur.
95.55 - 98.00 : marne feuilletée et grumeleuse, bariolée, tectonisée et tendre jusqu'à 97.60 m. puis plus dure et un peu moins grumeleuse.
98.00 - 99.00 : marne gréseuse, kaki localement grise et lie de vin, plaquetée, dure à très dure.
99.00 - 100.10 : marne gréseuse, grise, massive à plaquetée, dure, légèrement grumeleuse à la base sur env. 15 cm.
100.10 - 102.50 : grès fin gris, très dur.
102.50 - 104.60 : marne grumeleuse, bariolée à dominante vert foncé et violacé. tectonisée, tendre, très sensible
104.60 - 106.00 : marne calcareuse grise et lie de vin, dure peu sensible.
106.00 - 107.50 : marne grumeleuse vert foncé à noirâtre, tectonisée, tendre, altérable.
107.50 - 108.20 : marne gréseuse grise, dure.
108.20 - 110.00 : marne feuilletée et grumeleuse, lie de vin et kaki, légèrement tectonisée et dure jusqu'à 109.00 m., puis tendre et nettement tectonisée.

HYDROLOGIE

Forage sec lors des travaux (2.11 - 8.11.1995)

Figure 89: Borehole 10601 p. 1 (M. J. Stuart, personal communication, November 28, 2017)

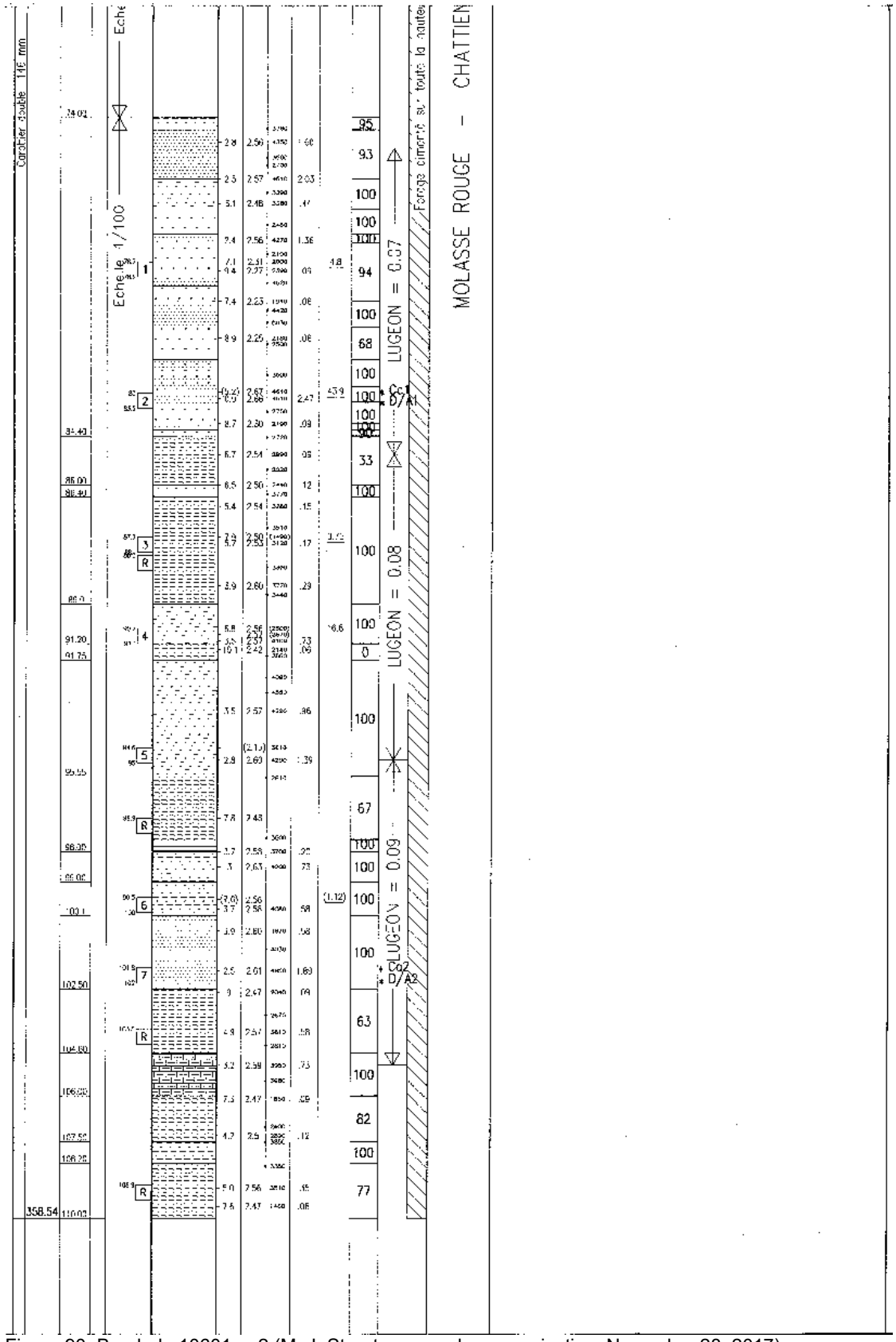

Figure 90: Borehole 10601 p. 2 (M. J. Stuart, personal communication, November 28, 2017)

7. References

[1] M. Aicheler *et al.*, “A Multi-TeV linear collider based on CLIC Technology: CLIC Conceptual Design Report,” Geneva, 2012.

[2] A. Zemanek, “Active repositioning and sensor characterization for the CLIC module,” 2018. [Online]. Available: https://indico.cern.ch/event/656356/contributions/2838066/attachments/1587605/2510747/CLIC_workshop_Active_repositioning.pdf. [Accessed: 15-Feb-2018].

[3] E. Lam, “Conjugate Heat Transfer Simulations with CFD,” 2017. [Online]. Available: https://indico.cern.ch/event/684351/contributions/2805543/attachments/1572166/2480868/Conjugate_Heat_Transfer_Simulations_with_CFD.pdf. [Accessed: 20-Feb-2018].

[4] M. Aicheler, “CLIC Module Heat load calculations, modelling and experimental program,” 2018. [Online]. Available: https://indico.cern.ch/event/656356/contributions/2838063/attachments/1587802/2511178/CLICWS2018-Aicheler-TBMThermal.pdf. [Accessed: 20-Feb-2018].

[5] ANSYS, *ANSYS ICEM CFD Help Manual Release 17.2*. Canonsburg, PA, 2016.

[6] ANSYS, *ANSYS ICEM CFD User’s Manual Release 17.2*. Canonsburg, PA, 2016.

[7] Wikipedia, “Density of air,” 2018. [Online]. Available: https://en.wikipedia.org/wiki/Density_of_air. [Accessed: 07-May-2018].

[8] ANSYS, *ANSYS Fluent User’s Guide Release 17.2*. Canonsburg, PA, 2016.

[9] ANSYS, *ANSYS Fluent Theory Guide Release 17.2*. Canonsburg, PA, 2016.

[10] M. G. Marzoa, “Estimate of the steady-state heat load dissipation to the ground in the HL-LHC UR15 and UR55 tunnel sections,” Geneva, 2015.

[11] A. K. Khatry, M. S. Sodha, and M. A. S. Malik, “Periodic variation of ground temperature with depth,” *Sol. Energy*, vol. 20, no. 5, pp. 425–427, 1978.

[12] M. Badache, P. Eslami-Nejad, M. Ouzzane, Z. Aidoun, and L. Lamarche, “A new modeling approach for improved ground temperature profile determination,” *Renew. Energy*, vol. 85, pp. 436–444, 2016.

[13] B. Givoni and L. Katz, “Earth temperatures and underground buildings,” *Energy Build.*, vol. 8, no. 1, pp. 15–25, 1985.

[14] G. Al Nakshabandi and H. Kohnke, “Thermal conductivity and diffusivity of soils as related to moisture tension and other physical properties,” *Agric. Meteorol.*, vol. 2, no. 4, pp. 271–279, 1965.

[15] Y. Hiraiwa and T. Kasubuchi, “Temperature dependence of thermal conductivity of soil over a wide range of temperature (5-75°C),” *Eur. J. Soil Sci.*, vol. 51, no. 2, pp. 211–218, 2000.

[16] C. Clauser *et al.*, “Erkennen und Quantifizieren von Stroemung: Eine geothermische Rasteranalyse zur Klassifizierung des tiefen Untergrundes in Deutschland hinsichtlich seiner Eignung zur Endlagerung radioaktiver Stoffe,” Aachen, 2002.

[17] C. Cook and J. Osborne, “FCC 100km Intersecting Option Rock Temperatures: Estimates & Potential Applications,” Geneva, 2016.

[18] V. Gnielinski, “Neue Gleichungen für den Wärme- und den Stoffübergang in turbulent durchströmten Rohren und Kanälen,” *Forsch. im Ingenieurwes.*, vol. 41, no. 1, pp. 8–16, 1975.

[19] Engineering ToolBox, “Dry Air Properties,” 2005. [Online]. Available: https://www.engineeringtoolbox.com/dry-air-properties-d_973.html. [Accessed: 27-Feb-2018].

[20] D. W. Hahn and M. N. Özişik, *Heat Conduction*, 3rd ed. Hoboken, N.J.: John Wiley & Sons, 2012.

[21] A. Moilanen, M. Aicheler, A. Vamvakas, and S. Doebert, “FINITE ELEMENT MODEL FOR THERMAL-STRUCTURAL ANALYSIS OF CLIC LAB MODULE TYPE 0#2,” Geneva, 2017.

[22] China jiangyou longhai Special Steel Co, “30CrNiMo8,” 2011. [Online]. Available: http://www.steelss.com/Carbon-steel/30crnimo8-.html. [Accessed: 21-Mar-2018].

[23] deust, “Behavior of Contact (In ANSYS),” 2012. [Online]. Available: https://deust.wordpress.com/2012/01/02/behavior-of-contact-in-ansys/. [Accessed: 11-May-2018].

[24] ANSYS, “ANSYS Mechanical User’s Guide Release 17.2,” Canonsburg, PA, 2016.

[25] T. Harris, “Default Contact Stiffness Behavior for Bonded Contact,” 2014. [Online]. Available: http://www.padtinc.com/blog/the-focus/default-contact-stiffness-behavior-for-bonded-contact. [Accessed: 14-Apr-2018].

[26] E. Lam, “Adjustable Support Simulations,” 2017. [Online]. Available: https://indico.cern.ch/event/670987/contributions/2744575/attachments/1534734/2403769/Adjustable_Support_Simulations.pdf. [Accessed: 22-Apr-2018].

[27] S. Uimonen, “TRANSPORTATION TEST SUPPORT,” Geneva, 2017.